

Analysis of 1.55 μ m Semiconductor Lasers for Modelocked Operation

by

Erwin Kin-Ping Lau

S.B., Massachusetts Institute of Technology (2000)

Submitted to the Department of Electrical Engineering and Computer Science
in partial fulfillment of the requirements for the degree of

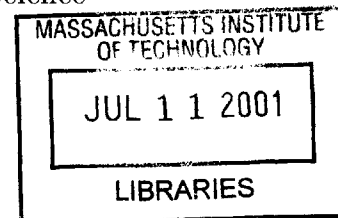
Master of Engineering in Electrical Engineering and Computer Science

at the

MASSACHUSETTS INSTITUTE OF TECHNOLOGY

February 2001

BARKER




© Erwin Kin-Ping Lau, MMI. All rights reserved.

The author hereby grants to MIT permission to reproduce and distribute publicly
paper and electronic copies of this thesis document in whole or in part.

Author
Department of Electrical Engineering and Computer Science
February 6, 2001

Certified by

 Rajeev J. Ram
Associate Professor
Thesis Supervisor

Accepted by
Arthur C. Smith
Chairman, Department Committee on Graduate Students

Analysis of $1.55\mu\text{m}$ Semiconductor Lasers for Modelocked Operation

by

Erwin Kin-Ping Lau

Submitted to the Department of Electrical Engineering and Computer Science
on February 6, 2001, in partial fulfillment of the
requirements for the degree of
Master of Engineering in Electrical Engineering and Computer Science

Abstract

This thesis derives its motivation from developing $1.55\mu\text{m}$ semiconductor modelocked lasers for use in high-speed, high-resolution optical analog-to-digital systems. Understanding how to experimentally determine laser parameters is vital to knowing how well the modelocked laser will perform. This thesis begins by explaining the different experimental techniques used in determining these parameters. Extensive use of the spectrum analysis method developed by Hakki and Paoli is used. The laser parameters can then be used in a theoretical simulation to determine the dynamics and performance of the modelocked laser. The simulation can be used to determine which parameters are most important when different design issues are imposed. This thesis first explores a split-step Fourier method developed by Derickson et al. A critical analysis of the method is presented and its limitations are discussed. A new split-step finite difference method is developed and analyzed. The method is used to determine trends useful for design of superior performance modelocked lasers.

Thesis Supervisor: Rajeev J. Ram
Title: Associate Professor

Acknowledgments

There are a few people I'd like to thank. These people have either been great friends that have filled my life with color, variety, and enjoyment or they have been selfless sources of knowledge and information. First and foremost is my advisor, Rajeev. Thank you for teaching me so much about lasers and life. You have been my rolemodel, mentor, and friend for so many years. Your unconditionally positive attitude has kept me going in the face of so many obstacles. Your vast and comprehensive knowledge of science and your willingness to share it is, in my mind, the most noble of characteristics. You may never know how much you have impacted my life in so many positive ways. I hope it is enough to say that I would not be anywhere near the kind of person that I am if I hadn't met you. Thanks to Fatih for many great hours of talks about philosophy and academics; you're one of the few people I've met that shares my shameless and unabashed curiosity and thirst for knowledge. Your talent will take you as far as you wish to go in life. Thanks to Farhan for providing the lasers and physical knowledge. Your thirst for knowledge and thoroughness is truly inspirational. Thanks to Harry for so many tidbits of knowledge, both conceptually and experimentally. You have a mirthful wit and commanding intellect. Thanks to Steve for the bipolar cascade lasers, for sharing your knowledge, and for steadfast friendship and a willingness to teach. I have always appreciated your frankness and have learned much from you about so many things. Thanks to Mathew for your unwavering positiveness and erudition. You have always been a man of strong and just principle, whom I respect very highly. Thanks Margaret, for everything. There's just too much to list. Your loving attitude towards life and friendship brings a smile to my face; knowing that there exists people as special as you. Thanks, Peter, for your friendship and for being the guy who miraculously balances living life and learning. Your friendly, unassuming attitude is always welcome and refreshing. I wish I had the chance to play Ultimate with you. Maybe someday, when you come out to California. Thanks, Kevin, for many enjoyable and frank talks. I respect your attitude and confidence on life and know you will achieve your goals. Thanks, Holger, for your teaching and for always being friendly and courteous. I know you will make a great

professor someday. Thanks also, to Professor Ming Wu and the guys at UCLA for allowing me the freedom to finish my thesis under unusual circumstances and putting up with my quirky work habits. I am also largely indebted to my friends: Mainn, Robby, Emily and Risat, who have always made me feel like I belong somewhere in this large and sometimes lonely world. And lastly, to my family: David, Julia, and Herman. Nothing I have done or will do could have taken place without you. You will always remain most special in my life. I feel truly blessed to have been surrounded by such wonderful, caring people.

Contents

1	Introduction	17
1.1	A/D Converters	18
1.2	Optical A/D Converters	20
1.3	Modelocking	24
1.3.1	Active Modelocking	27
1.3.2	Passive Modelocking	28
1.3.3	Hybrid Modelocking	30
1.4	Thesis Overview	31
2	Characterization	33
2.1	Laser Design	33
2.2	Laser Rate Equations	37
2.3	Theoretically-Derived Parameters	40
2.3.1	Group Velocity (v_g)	40
2.3.2	Confinement Factor (Γ)	41
2.3.3	Mirror Reflectivity (R)	41
2.4	Experimental Parameters	42
2.4.1	Loss (α_i) and Internal Quantum Efficiency (η_i) Measurements	42
2.4.2	Derivation of Fabry-Perot Modes	46
2.4.3	Measuring the Fabry-Perot Modes	50
2.4.4	Group Index Measurements	53

2.4.5	Loss/Gain Curve Measurements	53
2.4.6	Recombination Coefficients	61
2.5	Summary	64
3	Theory and Split-Step Simulations	67
3.1	Laser Parameters	67
3.2	Traveling Wave Rate Equations	68
3.3	Pulse-Shaping Mechanisms	71
3.3.1	Non-linear Effects	71
3.3.2	Linear Effects	80
3.4	Simulations	84
3.4.1	Split-step method	86
3.4.2	Simulation Validity	94
3.4.3	Limitations and Improvements	101
3.5	Summary	104
4	Finite Difference Simulations	105
4.1	Introduction	105
4.2	Summary of Simulation Methods	106
4.3	Laser Rate Equations	108
4.4	Finite Difference Laser Rate Equations	109
4.4.1	First-Order Finite Difference Approximations	109
4.4.2	Implementation	110
4.4.3	Calculating Error	113
4.5	Classic Finite Difference Simulation Results	114
4.5.1	First-Order Derivative Finite Difference Equations	114
4.5.2	Second-Order Derivative Finite Difference Equations	116
4.6	Difference Equation Filtering	118
4.7	Split-step/Finite Difference Simulation	121

4.7.1	Symmetric Difference Equation Filtering	122
4.7.2	Reverse-Bias Model	128
4.7.3	Computational Recipe	129
4.7.4	Simulation Validity	131
4.8	Design Trends	133
4.8.1	Biasing	140
4.8.2	Geometry	148
4.8.3	Intrinsic	148
4.9	Summary	152
5	Conclusion	155
5.1	Summary	155
5.2	Future Work	156
5.2.1	Active Modulation	156
5.2.2	Phase Effects	156
5.2.3	Direct Derivative Filter	158
5.2.4	Filtering Limit	160
5.2.5	Energy Conservation	160
5.2.6	Lax Averaging	160
5.2.7	Spontaneous Emission Modeling	161
A	Matlab Code	163
A.1	Hakki-Paoli Code	163
A.1.1	hakki.m	163
A.1.2	findpeak.m	164
A.2	Split-step Fourier Code	166
A.2.1	modelock.m	166
A.2.2	LaserParam.m	168
A.2.3	makeRTmatrix.m	169

A.2.4	splitstep.m	170
A.2.5	findwidth.m	172
A.2.6	PlotModelock.m	172
A.3	Split-step Finite Difference Code	173
A.3.1	findGBWFunc.m	173
A.3.2	fdiffMain.m	175
A.3.3	LaserParam.m	177
A.3.4	fdiffLoop.m	179
A.3.5	plotRT.m	181
A.3.6	plotEP.m	183
B	Second-Order Derivative Approximations	185

List of Figures

1-1	(a) Analog sine wave. (b) Sine wave discretized in time. (c) Sine wave discretized in time and magnitude. (d) Sine wave discretized into binary channels.	19
1-2	Resolution and sampling rate for currently-existing A/D converters [63]	20
1-3	Schematic of Proposed Optical A/D system [59]	22
1-4	(a) Ideal pulse train. (b) Pulse train with amplitude jitter. (c) Pulse train with timing jitter.	23
1-5	(a) Frequency-domain and (b) Time-domain representations of modelocked pulses .	25
1-6	General active modelocking scheme: (a) active section (b) waveguide section. Energy is coupled from each mode to its neighbors.	29
1-7	Time domain explanation of active modelocking. The photon gain is highest when the pulse inhabits the RF Gain region.	29
1-8	General passive modelocking scheme: (a) saturable absorber section (b) gain section	30
1-9	Semiconductor modelocked laser comparison [17]	31
2-1	(a) Side view of laser, including biasing scheme. (b) Band structure of active region.	35
2-2	Schematic of hybrid laser design: (a) without (shown for detail) and (b) with polyimide planarization.	36
2-3	E.P.I. laser design	37
2-4	Field and index profile in laser core, E.P.I. growth	42
2-5	Typical Power vs. Current laser curve and representation of dP/dI , E.P.I. growth .	43
2-6	Linear fit of $1/\eta_d$ versus $1/\alpha_m$ to determine α_i and η_i , E.P.I. growth	44

2-7	Representation of Fabry-Perot modes	47
2-8	Simulation of Fabry-Perot field spectrum in $n_g = 1$ medium.	49
2-9	Schematic of test setup	51
2-10	Typical OSA trace for a laser below threshold, showing the Fabry-Perot resonances, E.P.I. growth, $L=300\mu m$, width= $5\mu m$, 10mA bias, $20.2^\circ C$	52
2-11	Index spectrum for different biases, E.P.I. growth, $L = 300\mu m$, $W = 5\mu m$, $T = 293.2K$	54
2-12	Overall material gain ($\Gamma g - \alpha_i$) for different biases, E.P.I. growth $L = 320\mu m$, $W = 3\mu m$, $T = 293.2K$	57
2-13	Gain (g) spectrum from (a) theoretical simulation (b) Hakki-Paoli experimental extraction. E.P.I. growth $L = 320\mu m$, $W = 3\mu m$. Theory: $T = 300K$. Experiment: $T = 293.2K$	59
2-14	Theoretical loss curves and experimental loss, E.P.I. growth, $L = 320\mu m$, $W = 3\mu m$, $T = 293.2K$, $I = 17mA$	60
2-15	Peak gain (g) versus carrier density (N) for different quantum well temperatures, E.P.I. growth	62
2-16	Current Density (J) versus carrier density (N) theory and data, E.P.I. growth. $A = 1.1 \times 10^8$, $B = 1 \times 10^{-10}$, $T = 293.2K$	63
2-17	L-I curve for biases well below threshold along with fitted parameters	65
2-18	A , B , and C parameters as a function of η_c , as fitted to L-I curve	65
3-1	Examples of (a) gain and (b) absorption saturation effects. $L_{gain} = L_{sa} = 50\mu m$, $I_{gain} = 4mA$, $g_{sa} = -9539cm^{-1}$	73
3-2	Example of pulse drifting due to gain saturation; pulse evolves with lighter pulse color. Each pulse represents one round-trip propagation from the previous. $t = 0$ follows the propagation at the pulse's group velocity. $\alpha = 0$, $L_{gain} = 50\mu m$, $I_{gain} =$ $3mA$	74

3-3 (a) Pulse evolution with shaping potentials. Each evolved pulse is shown with the shaping potential used to create it from the previous pulse (directly above). Top picture is the original pulse. The following pictures show evolution due to gain saturation, absorption saturation, and mirror reflection, respectively. (b) Pulses on an absolute scale (pulse evolves with lighter pulse color). (c) Total shaping potential, including unity line. $L_{gain} = L_{sa} = 50\mu m, I_{gain} = 6mA, g_{sa} = -1.244 \times 10^4 cm^{-1}, \alpha = 0$ 77

3-4 Self-phase modulation effects due to linewidth enhancement factor. $\alpha = 2$. Graphs shown are Power (P), Carrier density (N), index (n), instantaneous frequency (f). $L_{gain} = L_{sa} = 50\mu m, I_{gain} = 4mA, g_{sa} = -9539cm^{-1}$ 78

3-5 Examples of (a) pulse drifting due to dominant gain saturation in a 2-section passively modelocked laser and (b) pulse drift cancelling in a 2-section active modelocked laser. $L_{sa} = L_{act} = 80\mu m, L_{gain} = 3500\mu m, \omega_M = \frac{v_g}{2(L_{act} + L_{gain})}, I_{gain} = 63mA, g_{sa} = -1864cm^{-1}, I_{RF} = 5mA, g_{act} = -9159cm^{-1}$ 80

3-6 Gain vs. wavelength at 300K and several carrier densities 82

3-7 Determination of g_p, ω_0 and t_2 . The fit is second-order. 82

3-8 Example of pulse broadening due to finite gain bandwidth. (a) shows the input pulse and the broadened pulse. (b) shows the input and broadened spectrum. (c) shows the magnitude of the filter. $t_2 = 1 \times 10^{-13}s, g_p = 2 \times 10^4 cm^{-1}, L = 50\mu m$ The gain was increased for illustrative purposes. 83

3-9 Example of pulse broadening due to dispersion. (a) shows the unchirped input pulse and the broadened pulse. (b) shows the instantaneous frequency. (c) shows the phase of the filter. $\beta_2 = 4 \times 10^{-22} cm^2/s, L = 50\mu m$ 85

3-10 Explanation of split-step method 92

3-11 Pulse evolution from split-step simulation. Pulse evolves dark to light pulse lines. $I_{gain} = 63mA, g_{sa} = -7776cm^{-1}$. The saturable absorber was split into 4 sections of $20\mu m$ each; the gain section was split into 35 sections of $100\mu m$ each. 93

3-12	Pulse width [(a)&(c)] and pulse energy [(b)&(d)] evolution. (a)&(b) vary the initial pulse energy. (c)&(d) vary the initial pulse width. In all cases, the steady-state pulse width is $4.1ps$, pulse energy is $1.1pJ$. Laser parameters are the same as in Figure 3-11.	95
3-13	Comparison between analytic solution and simulation with (a) gain bandwidth only (b) dispersion only unchirped Gaussian Pulse input, $t_2 = 0.1ps$, $\beta_2 = 10^3ps^2m^{-1}$, $L = 10\mu m$, $g_p = 5 \times 10^4cm^{-1}$ (illustrative purposes)	98
3-14	Diagram of ring cavity [61].	99
3-15	Pulse width evolution with various initial pulse widths. Each reach the same steady state. $L = l = 50\mu m$, $g_0 = 4cm^{-1}$, $\alpha_0 = 2cm^{-1}$, $M = 506.6059$, $\omega_M = 2\pi \times 1GHz$, $t_2 = 5ps$	101
4-1	Illustration of the state variables in a three-section laser structure with P sections. The total laser length is $P\Delta z$	111
4-2	Pulse evolution with insufficient broadening forces (infinite gain bandwidth). Selected round trip snapshots are shown.	115
4-3	Pulse evolution using unstable finite gain bandwidth implementation. (a) the initial pulse ($t = 0fs$). (b) the pulse at the threshold of instability ($t = 58fs$). (c) the pulse exhibiting significant instability ($t = 63fs$). (d) the pulse well beyond the threshold of instability ($t = 70fs$).	117
4-4	Parabolic gain spectrum model and the frequency response of filters with varying η (From [31])	119
4-5	Fitting of the digital filter parameter, η , for various Δt . The fit is to Equation 4.33 for a given $t_2 = 5 \times 10^{-13}s$. Shown above are for $\Delta z =$ (a) $1\mu m$ (b) $5\mu m$ (c) $10\mu m$	124
4-6	Error corresponding to the digital filter approximations defined by the parameters in Figure 4-5. Shown above are for $\Delta z =$ (a) $1\mu m$ (b) $5\mu m$ (c) $10\mu m$	126
4-7	$\eta(g_p)$ for various $\Delta z = 1\mu m, 5\mu m, 10\mu m$	127
4-8	Steady-state pulse width and energy for different space increments.	132
4-9	Steady-state (a) pulse width and (b) pulse energy for different initial pulse widths.	133

4-10	Steady-state (a) pulse width and (b) pulse energy for different initial pulse energies.	134
4-11	Pulse evolution to steady-state for two different initial relative pulse locations. . .	135
4-12	Laser output with $I_{act}^{RF} = 0$. The pulse continues to advance in time faster than the group velocity.	136
4-13	DC L-I curves for three-section laser.	136
4-14	Optical spectrum of three-section laser.	138
4-15	Schematic of laser used for design [29].	139
4-16	(a) Pulse width and (b) pulse energy versus gain region bias current, for different saturable absorber lengths (no active modulation).	142
4-17	(a) Pulse width and (b) pulse energy versus gain region bias current, for different modulation depths.	143
4-18	(a) Pulse width and (b) pulse energy versus detuning frequency, for different modulation depths.	144
4-19	(a) Pulse width and (b) pulse energy versus detuning frequency, for different modulation depths. A more detailed view than Figure 4-18.	145
4-20	(a) Pulse width and (b) pulse energy versus gain region bias current, for different saturable absorber strengths (measured by carrier lifetime).	147
4-21	(a) Pulse width and (b) pulse energy versus gain region bias current, for different saturable absorber lengths in a 37.8 GHz cavity.	149
4-22	(a) Pulse width and (b) pulse energy versus gain region bias current, for different saturable absorber lengths in a 30 GHz cavity.	149
4-23	(a) Pulse width and (b) pulse energy versus gain region bias current, for different saturable absorber lengths in a 20 GHz cavity.	150
4-24	(a) Pulse width and (b) pulse energy versus gain region bias current, for different optical loss values.	151
4-25	(a) Pulse width and (b) pulse energy versus gain region bias current, for different left-hand-side mirror reflectivities.	152

- 4-26 (a) Pulse width and (b) pulse energy versus gain region bias current, for different internal reflections. 153
- 5-1 Actual filter with fitted filter for $\Delta z = 5\mu m$. (a) $t_2 = 5 \times 10^{-13} s$ (b) $t_2 = 1 \times 10^{-13} s$ 159

List of Tables

3.1	Laser Parameters	68
4.1	Table of simulation methods. ✓ = suitable application. □ = untested but suitable application. † = limitations deter usage. suitable otherwise.	107
4.2	Laser Parameters	137

Chapter 1

Introduction

Analog-to-digital converters are an integral technology that allows us to interpret real world information into electrical data. They are the necessary interface of computers to the physical world, allowing us to create massive databases, communicate with others across the globe, store and analyze scientific data, and control electrical devices such as robots, to name just a few applications. They also allow us to perform tasks that were never before possible, such as weather forecast modeling or secure data encryption. The success of computers relies on the ability to transmit, store, and manipulate digital data. Without this, they would not have been able to achieve the speed, power, and reliability that we take for granted today. The real world, however, is not digital. For example, our limbs do not have a limited number of specified positions that they can bend. Rather, they can swing freely through a virtually infinite number of positions that span the range of flexed to extended. If a computer was used to model the movement of a human arm, it would not have the ability to represent the position of the arm to infinite precision since this would require an infinitely large storage device. It is, however, allowed to take the infinite number of possible positions and pick (for argument's sake) a large number of them that would suitably represent the entire set. This process is called discretization, and is similar to rounding a number off to an integral value. The number of discrete values that have been selected to represent the whole analog set determines the accuracy of the digital

representation.

The ability for digital systems to interact with the real world is of great importance. Weather satellites need to translate weather information such as cloud locations, temperature fluctuations, etc. into digital data in order to transmit this to computers on earth for analysis. Digital cellular phones take human speech, digitize it, encode it and transmit it via radio waves, which are analog. These wave eventually are received, redigitized, decoded, and played over the listener's phone speaker. Even a computer keyboard takes finger pressure and translates this into a digital representation of a letter. All of these applications necessitate converting analog, real-world data into a digital representation. The devices that perform this action, analog-to-digital (A/D) converters, are the subject of current research.

1.1 A/D Converters

The ability to perform high-speed and/or high-resolution A/D conversion is essential in a wide variety of applications, such as recording/analysis of scientific data and on-the-fly audio or image data processing. A/D converters take analog signals that are continuous in time and magnitude, such as human speech or the temperature in a room, and discretize them in both time and magnitude. This is performed in two stages. The continuous-time analog signal is sampled periodically in time, taking only specific values of the waveform (Figure 1-1(b)). Then each of those time-samples are then discretized in magnitude, "rounded" to a specific, discrete magnitude that most closely represents the true value (Figure 1-1(c)). This leads to defining two important figures-of-merit for describing A/D conversion: sampling rate and sample resolution. The ability to increase the sampling rate, which is typically measured in Hertz (Hz) or samples-per-second, allows more information to be sent in a given time interval. The increase of the sample resolution, which is measured in bits-per-sample, increases the sensitivity of the information that is collected.

Due to error introduced by noise and quantization, a practical maximum limit is set on the these parameters. In general, the existing state-of-the-art A/D converters follow a trend in which for every doubling of the sampling rate, a bit of resolution is lost [63]. Depending on

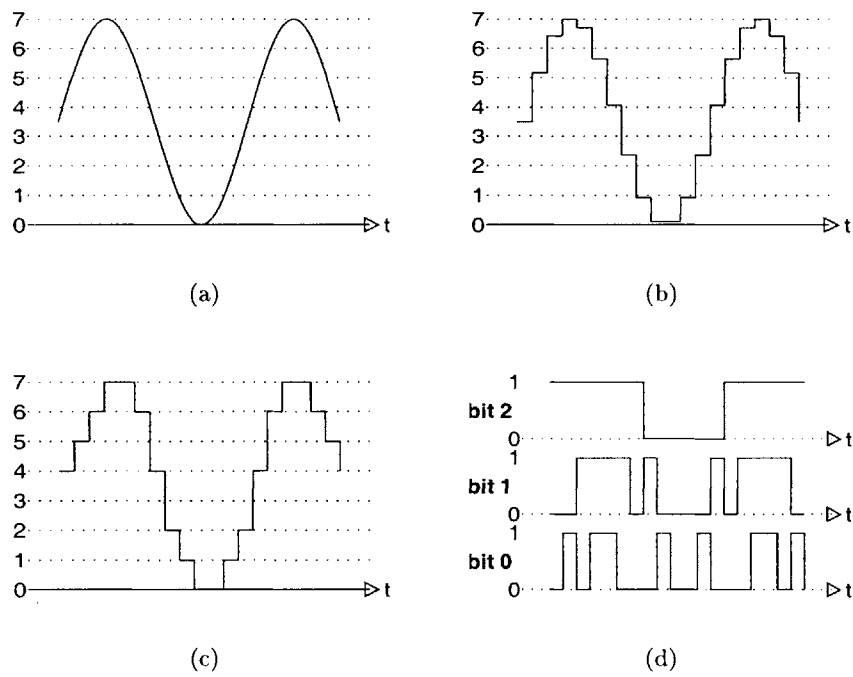


Figure 1-1: (a) Analog sine wave. (b) Sine wave discretized in time. (c) Sine wave discretized in time and magnitude. (d) Sine wave discretized into binary channels.

the application, a high sampling rate is accompanied by a mediocre resolution, or vice-versa. For example, certain video applications require 14-bits at 2 Megasamples/second (MSPS) while other audio applications require 24-bits at 96 kilosamples/second [4]. Figure 1-2 shows a scatter-chart of currently-available A/D converters. Most of these A/D converter systems are implemented electrically. Since the essentially analog input is typically electrical, this choice makes sense. Electrical systems are inherently high-speed due to electron transport speeds and lifetimes. The current state-of-the-art converters are primarily implemented with IC transistor technology [4].

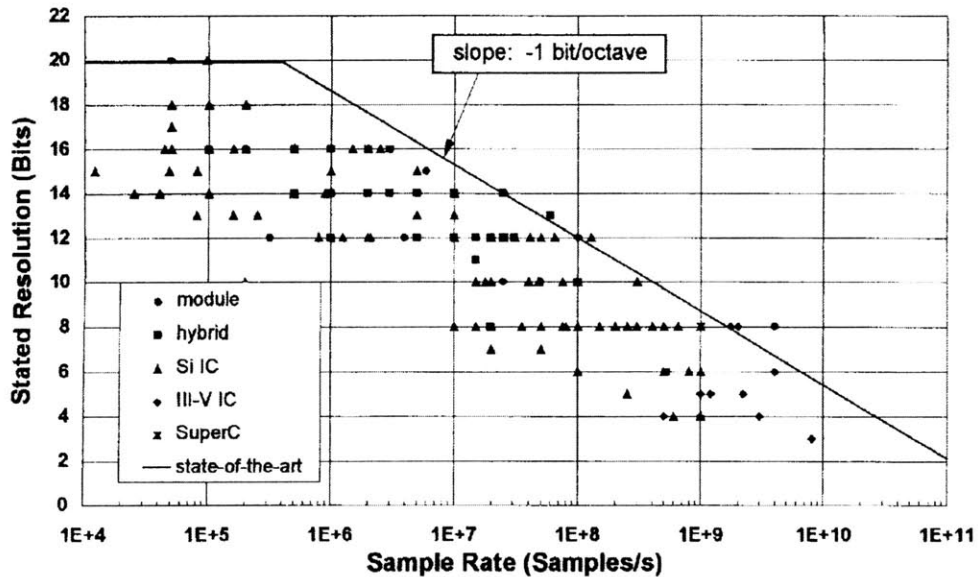


Figure 1-2: Resolution and sampling rate for currently-existing A/D converters [63]

1.2 Optical A/D Converters

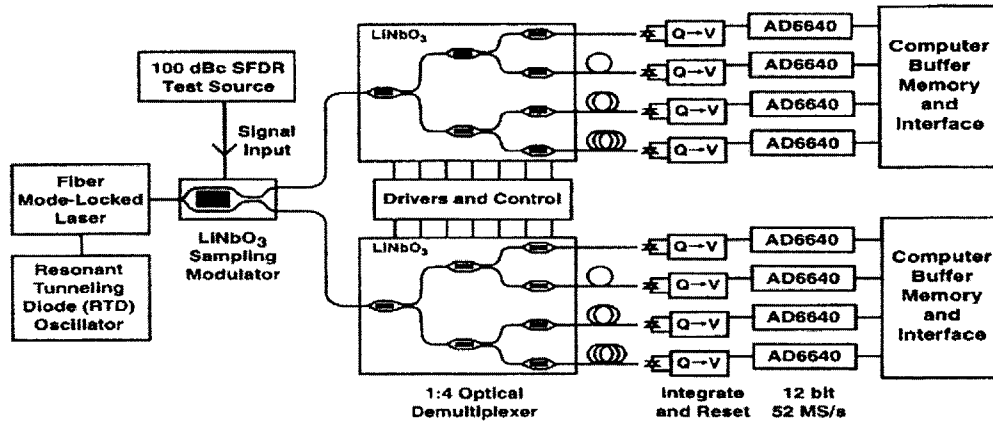
Applications are being developed that require A/D conversion at high speeds and greater sensitivity. As the need for faster, higher-resolution converters arises, new techniques of conversion are being explored. The current goal for the next state-of-the-art converters is to create a 10 GHz, 12-bit resolution A/D converter, which is necessary for certain data col-

lection applications. A/D conversion has traditionally been implemented with all-electrical components. All-electrical converters are bottlenecked in sampling rate and resolution by electrical sample-and-hold circuitry [59].

In order to overcome the bottleneck, alternative methods of conversion are being explored. The most promising alternative is to perform optical A/D conversion. Optical A/D conversion is not limited in sampling rate, since it employs optical pulses to bypass the need for high-speed electrical sample-and-hold circuitry. There is also no cross-talk between the sampling clock (which is optical) and the RF data signal (which is electric).

There are several methods that employ photonics to achieve higher speed and resolution A/D conversion [18, 56]. One of the currently researched methods uses a laser which produces periodic optical pulses. This periodic laser pulse train serves as the sampling clock for the sampling sub-system. The analog electrical input signal modulates the voltage input of an electro-optic modulator (EOM), whose optical input is the laser pulse train. As each pulse passes through the EOM, its amplitude is modified by the voltage level of the electrical input. Thus, the optical input pulses can "read" the radio-frequency (RF) electrical input. The output is an amplitude-modulated train of optical pulses that represent the discretized analog signal. These optical samples are then converted into electrical step waveforms before they are turned into bits. However, there are still speed limitations on the electrical components that perform amplitude-digitization. Therefore, the optical-to-electrical sub-system implements a 1:4 time demultiplexer that splits the optical signal into four optical signals that are $\frac{1}{4}$ the data rate of the original (Figure 1-3). These optical samples are then turned into time-discrete electrical step waveforms using an optical detector/integrator (sample-and-hold system) [56]. These lower-frequency electrical signals can then be digitized by a traditional electrical A/D converter, which converts these time-discrete electrical waveforms into 12 discrete electrical bit waveforms. The bit waveforms are then collected by a computer and then post-processed to multiplex the information into its original order. This setup has been proposed in [59]. Figure 1-3 shows the diagram of this system. The advantage of this system is by using the demultiplexer, the limitations

of sampling rate of the electrical digitizers can be overcome by splitting the signal into slower components. By using optical components, limitations of speed and resolution can be



CFM2 Fig. 1. 208-MS/s phase-encoded time-demultiplexed optical sampling system comprised of (i) a fiber laser mode-locked using a resonant tunneling diode (RTD) oscillator, (ii) a dual-output LiNbO₃ Mach-Zehnder interferometer, (iii) a pair of 1:4 optical time-demultiplexers, (iv) an array of integrate-and-reset circuits, (v) an array of 12-bit quantizers (AD6640) operating at 52 MS/s, and (vi) a computer for performing control, system calibration, and phase demodulation.

Figure 1-3: Schematic of Proposed Optical A/D system [59]

A quantitative analysis on the maximum achievable resolution for a given sampling frequency leads to a study of the noise present in a practical system and a classification of the different noise phenomenon [63]. In the proposed optical A/D converter, the noise introduces itself at different segments of the system. The first, quantization noise, arises from the fact that when an analog signal is translated into a discrete magnitude, error from the 'rounding-off' process is created. Quantization noise is inherent even in an ideal A/D converter. Other noise sources are non-ideal and contribute to the deviation of the output from the ideal case. This noise can effectively make the lowest significant bits of the converter useless, depending on the ratio of the noise to the signal, or signal-to-noise (SNR)

ratio. The effective usable bits can be calculated, given the SNR:

$$N_{eff} = (SNR(dB) - 1.76)/6.02 \quad (1.1)$$

where N_{eff} is the effective number of bits and $SNR(dB)$ is the signal-to-noise ration [dB]. The greatest sources of error come from the noise introduced by the optical pulse train. An ideal pulse train has evenly spaced pulses in time and each equal in magnitude. Optical pulses can have variations in amplitude, which produce variations in the magnitude of the sampled RF signal (Figure 1-4(b)). This is known as amplitude jitter and has a nominal effect on the increase of the system's noise. A more cogent source of error is the variations of time between pulses that cause a non-periodic pulse train (Figure 1-4(c)). This source of error is known as timing jitter and is a parameter for pulse-producing lasers that is not well understood [14, 25, 62, 40].

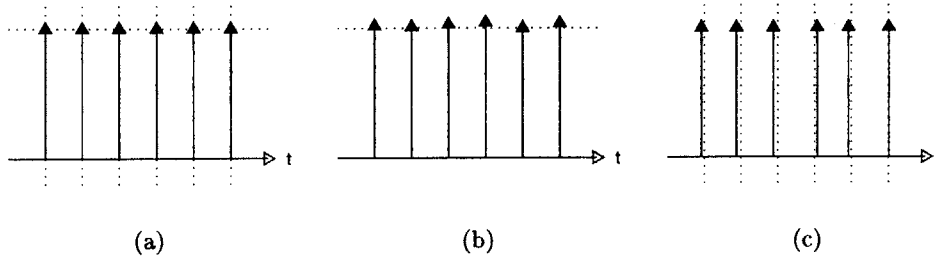


Figure 1-4: (a) Ideal pulse train. (b) Pulse train with amplitude jitter. (c) Pulse train with timing jitter.

The maximum achievable bit resolution can be calculated, given a timing jitter, τ_a :

$$B_{tj} = \log_2 \left(\frac{2}{\sqrt{3}\pi f_{samp}\tau_a} \right) - 1 \quad (1.2)$$

where B_{tj} is the maximum achievable bit rate due to timing jitter limitations and f_{samp} is the sampling frequency of the A/D converter [Hz]. For the proposed system, with a

sampling rate of 10 GHz and 12 bits per sample, this would imply a timing jitter of 4.5 fs. Even for a moderate sampling rate of 1 GHz at 12 bits/sample, a timing jitter of 45 fs is necessary. Currently, typical semiconductor pulsing lasers have timing jitters of hundreds of femtoseconds to picoseconds [13], well above that of the necessary specification to realize this high-speed system. Apparently, timing jitter is of utmost concern and remains as the most important parameter of a pulsed optical source. The challenge lies in creating a laser source that meets the specifications of the proposed system, which necessitates a drastic decrease in timing jitter.

Several varieties of laser design exist that are capable of producing periodic pulse trains. Examples include gain-switching, Q-switching, and modelocking [58]. Because of jitter, repetition rate, and other concerns, only modelocked lasers have been found as suitable sources for use in high-speed optical A/D converters (Figure 1-9).

1.3 Modelocking

In a laser, an optical resonator confines the optical field and promotes optical amplification due to stimulated emission [11]. The resonator confinement is accomplished in one dimension by two partially reflective mirrors that keep the light within the laser cavity. A fraction of that light is transmitted through the mirrors; this light that escapes is the observed output of a laser. In a simple laser design, these mirrors create Fabry-Perot resonances of the optical electro-magnetic field when a lasing steady-state is reached. A 1-dimensional resonant cavity can theoretically support a countably infinite number of these Fabry-Perot resonances (see Section 2.4.2). This produces a frequency comb where the resonance peaks, called modes, are separated by the round-trip frequency of the Fabry-Perot cavity (Figure 1-5(a)).

Due to the laser's active region's gain bandwidth, only one or a few of these modes exist in an above-threshold laser steady-state condition. Typically, the phase of these modes are uncorrelated. This produces a laser output that is randomly distributed in time but relatively constant due to the high frequency of the optical light. When the phases of these

modes are locked together so that they do not drift with respect to each other (or at most drift linearly, causing a time drift to the entire pulse), then the output of the light becomes a pulse train. A simple explanation for this is that the inverse Fourier transform of an infinite train of evenly-spaced frequency impulses is an infinite train of evenly-spaced impulses in the time-domain. These time-domain spikes correspond to optical pulses. Due to the finite gain bandwidth of the laser, only a finite number of frequency-domain peaks are available. This corresponds to a non-ideal impulse in the time-domain, i.e. an optical pulse with a finite, non-zero pulse width (Figure 1-5(b)). Since the Fabry-Perot resonance frequencies of the different modes are integral multiples of the round-trip frequency of the cavity, the pulse train exists at a mode separation at the round-trip frequency of the cavity also. Hence, the laser is modelocked and the output is an optical pulse train at the round-trip time of the Fabry-Perot cavity.

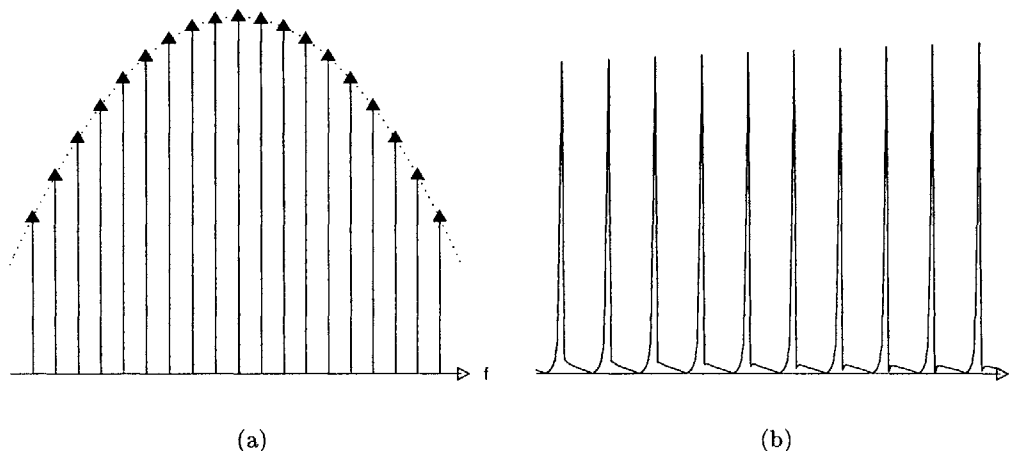


Figure 1-5: (a) Frequency-domain and (b) Time-domain representations of modelocked pulses

Modelocked lasers have the best chance of producing pulses that can meet the specifications to build the proposed A/D converter system. Prior results from this class of lasers promises the closest specifications in jitter and repetition rate to the proposed system. The repetition rate of modelocked lasers are determined by the round-trip frequency (or some

harmonic) of the laser resonator. Modelocked lasers have exhibited repetition rates of over 100 GHz [22], well beyond the specifications of the proposed system. Since the phases of the modes are correlated, the time variation between pulses is reduced. Actively mode-locked lasers have exhibited timing jitter values as low as $50 - 100 fs$ [33, 6, 15], whereas gain-switched lasers have timing jitter values typically greater than 1 ps [17, 40].

Modelocking has been achieved in a variety of material systems and configurations. Solid-state crystal modelocked lasers were the first demonstrated modelocked lasers. They utilize a solid-state crystal active element and typically employ free-space optics to define a resonant cavity. They provide high-power, short pulse width, low jitter pulses [19], however they are not usable in practical, high-volume applications due to their cost and size. Another currently researched method is fiber ring laser modelocking. Fiber ring lasers employ lengths of Erbium-doped fiber to provide a cost-effective gain-medium waveguide that can be looped into a ring configuration. Free-space optics are placed in the path of the ring geometry to produce modelocking. Fiber ring lasers are excellent choices for a modelocking, providing reasonably low jitter and smaller size than their solid-state crystal counterparts, but they continue to demand a relatively large volume due to the fiber lengths and optics [26].

The method explored in this thesis is semiconductor diode laser modelocking. Traditionally, semiconductor laser modelocking was performed by using semiconductor modelocking segments coupled together through free-space optics [16]. The facet reflectivity of the segments is kept to a minimum by anti-reflection coating and the light is typically focused through lenses. While typically smaller in real-estate than the other modelocking methods, the use of bulk optics necessitates sizable area constraints. However, the field of integrated circuits provides the ability to monolithically integrate all necessary modelocking components onto a single semiconductor wafer. Typical dimensions for a monolithic semiconductor modelocked laser wafer are less than a square millimeter and a few hundred microns thick. Fabrication techniques allow for massive parallel manufacturing, yielding low-cost, high-performance modelocked laser sources. The drawbacks are lower pulse power, and slightly higher timing jitter than their fiber ring laser counterparts.

The two major classifications of modelocking are active and passive modelocking. They are presented below in the context of semiconductor modelocked lasers but are general for all modelocked devices.

1.3.1 Active Modelocking

A general active modelocking scheme is shown in Figure 1-6. It consists of two major sections: (a) an active modulation section that is modulated by an RF signal at the round-trip frequency of the cavity and (b) a waveguide section that provides a cavity for the pulses to propagate through. The RF signal is typically a sinusoid but can be any sharply peaked function of current. This current modulation produces a carrier density modulation which in turn produces a photon gain modulation within the active section. Given an existing pulse within this cavity, it will enter the active section at the round-trip frequency of the cavity. If it has modelocked, then the pulse should propagate through the active section while the photon gain within that section is at its peak. When the pulse is not present in the cavity, the gain should be lower than the peak, until the pulse returns again to the active section. This time-dependent gain function causes the photon field to be highest only when the gain is highest, thus producing a pulse that propagates at the round-trip frequency of the cavity.

Rather than a time-domain explanation, a frequency-domain explanation can be used to explain this modelocking phenomenon. A frequency comb exists due to the Fabry-Perot resonances of the cavity. Each frequency mode is separated by the round-trip frequency of the cavity, but the time-domain profile is random due to the uncorrelated phases of the Fabry-Perot modes. The RF modulation, being at the round-trip frequency of the cavity, causes a non-linear coupling between the Fabry-Perot modes of the laser cavity, allowing energy from each mode to couple into their neighboring modes. This energy coupling also implies a phase coupling, since the photons carry with them their phase. Eventually, a steady-state solution of this mode coupling is a total homogeneity of phase. The phase locking implies the time-domain profile of the photon field (which is the inverse Fourier

transform of the frequency mode train) is a pulse train.

1.3.2 Passive Modelocking

Passive modelocking again requires at least two major segments, as shown in Figure 1-8: (a) a saturable absorber section and (b) a gain section. The purpose of the saturable absorber section, given a pulse propagating through it, is to attenuate the pulse, thus shortening its pulse width. Because of loss saturation in the saturable absorber, there will be a non-linear attenuation of the pulse. As the pulse enters the absorber, the front end of the pulse is attenuated as photons are absorbed by the material and excite electrons into the conduction band. As more and more of the pulse propagates through the absorber region, more of it is absorbed and the carrier density rises. This results in a reduction of the loss of the section, since there are fewer excitable valence electrons. If there is sufficient energy within the pulse, this will cause the material to approach transparency, which is the state of no loss or gain (the absorption is saturated). Hence, the end result is the pulse's leading edge is attenuated while the trailing edge is not. This effectively results in "shaving off" the front edge of the pulse and shortening the pulse width. If the gain is also saturable, the opposite effect occurs as the pulse propagates within the gain section. The leading edge of the pulse will be amplified while the trailing edge will not as much, thus resulting in a widening of the pulse. In a passively-modelocked laser, the competition of the saturable absorber's pulse narrowing and the gain section's pulse broadening leads to a steady-state round-trip condition in which the pulse propagates through the laser and returns to its original position and direction in exactly the same shape. The pulse has effectively been narrowed, broadened, broadened again, and narrowed back to its original shape.

Active modelocking is useful when low jitter pulses are desired. This is due to the fact that the RF modulation source serves also as a stabilizer of pulse period. The RF source, while inherently noisy itself, stabilizes the pulse period more effectively than without the source. Passive modelocking has no such stabilizing source and therefore has much higher timing jitter. Passive modelocking, however, is not limited in repetition rate by the

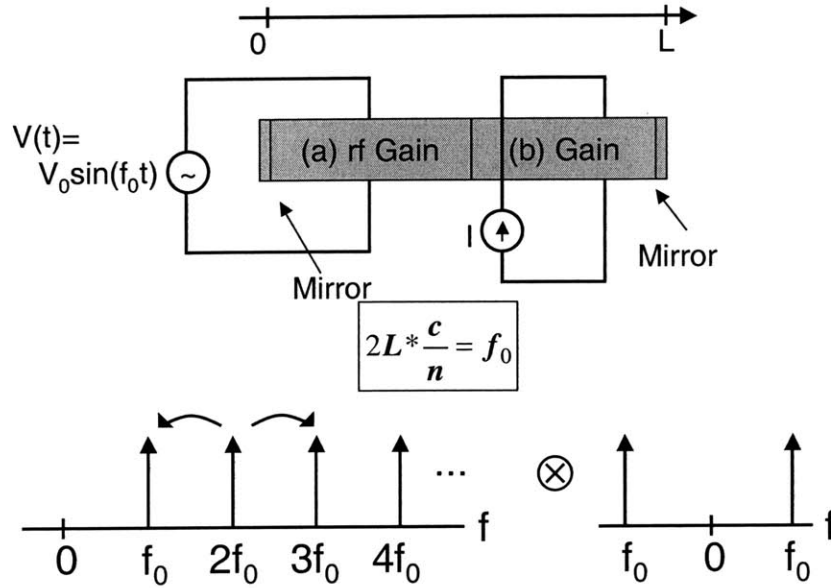


Figure 1-6: General active modelocking scheme: (a) active section (b) waveguide section. Energy is coupled from each mode to its neighbors.

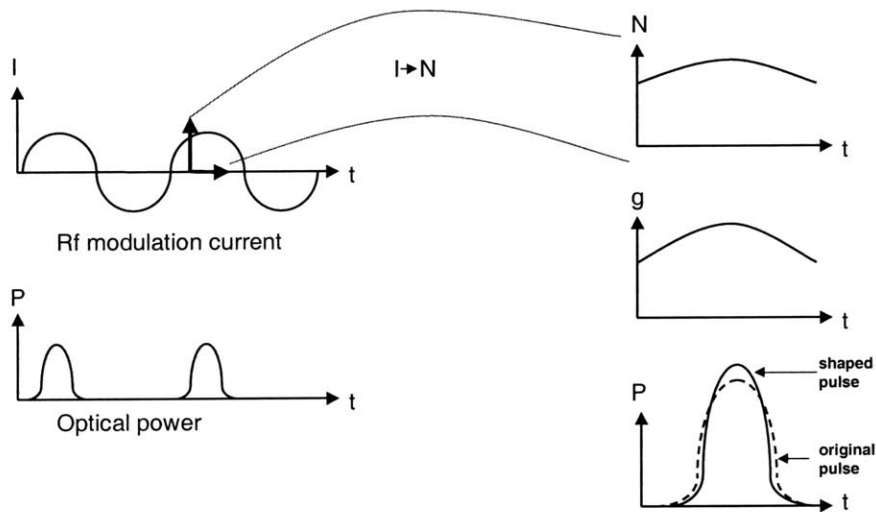


Figure 1-7: Time domain explanation of active modelocking. The photon gain is highest when the pulse inhabits the RF Gain region.

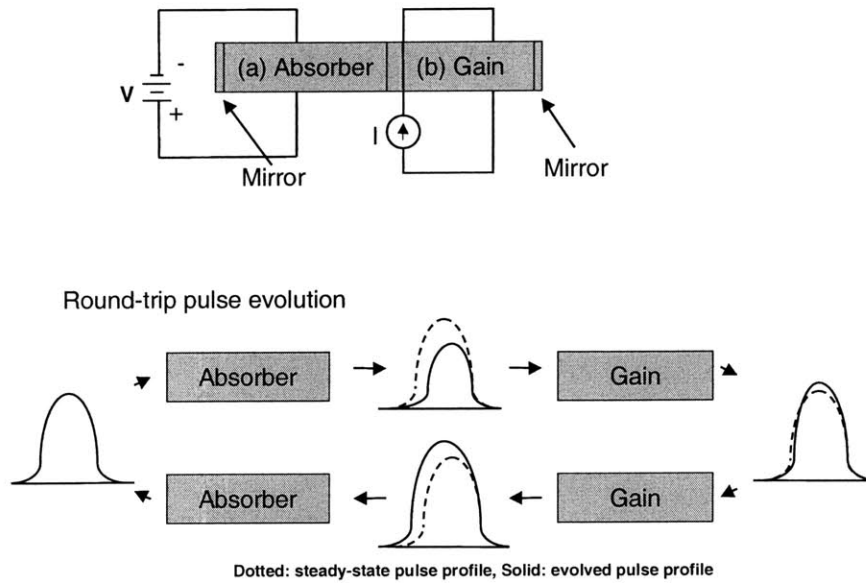


Figure 1-8: General passive modelocking scheme: (a) saturable absorber section (b) gain section

maximum obtainable RF source frequency, which typically cannot rise above 50 GHz. Since a source is not needed, the upper-bound on the repetition rate is not bottlenecked by this. Rather, the repetition rate is defined solely by the length of the laser, since this determines the round-trip frequency of the laser. Practically, there is a maximum repetition rate that is imposed by absorber to gain ratios [39].

1.3.3 Hybrid Modelocking

It is not a large step forward to realize a system that utilizes both active and passive modelocking phenomena. A three-section device can be fabricated to provide an actively modulated section, a saturable absorption section, as well as a gain/waveguide section. This technique is known as hybrid modelocking [16] and it provides the benefits as well as deficits of both methods of modelocking. Typical figures of merit for the three laser designs are shown in Figure 1-9.

Modelocked lasers can be used for applications other than optical A/D conversion. It

TABLE I
COMPARISON OF MULTISEGMENT STRUCTURE PERFORMANCE

Cavity Type	Modulation Technique	Pulse width (ps)	Spectral Width (GHz)	Time-Bandwidth Product	Pulse Energy (pJ)	Repetition Rate (GHz)	Wavelength (μm)	Active Region	Reference
Ext.	Active Two-Seg.	1.4	342	0.48	0.28	3	1.3	Bulk	[7]
Ext.	Passive Two-Seg.	2.5	720	1.8	0.7	5	0.84	4 QW	[22]
Ext.	Hybrid Two-Seg.	2.5	1000	2.5	0.8	5	0.84	4 QW	[22]
Ext.	Hybrid Three-Seg.	1.9	900	1.71	0.18	6	0.83	Bulk	[16], [27]
Mon.	Active Two-Seg.	13	330	4.3	0.19	5.5	0.84	4 QW	[22]
Mon.	Hybrid Three-Seg.	6.5	540	3.5	0.18	5.5	0.84	4 QW	[22]
Mon.	Passive Two-Seg.	10	400	4.0	0.25	5.5	0.84	4 QW	[22]
Mon.	Passive Two-Seg.	5.5	550	3.0	0.53	11	0.84	4 QW	
Mon.	Hybrid Three-Seg.	2.2	500	1.1	0.03	21	1.58	4 QW	
Mon.	Passive Two-Seg.	1.3	600	0.78	0.02	41	1.58	4 QW	[38]
Mon.	Q-Switch Two-Seg.	15	2400	36	4	1	0.825	Bulk	
Mon.	Gain-Switch Two-Seg.	13	4000	52	3.4	1	0.822	Bulk	

Figure 1-9: Semiconductor modelocked laser comparison [17]

is used for performing pump-probe experiments for exploring carrier dynamics. A "pump" pulse excites the sample of interest in which a "probe" pulse follows after some time delay and is detected. The detection of the probe pulse tells how the material has been affected by the pump pulse and the time delay between pulses. It is a useful technique for measuring carrier lifetimes.

1.4 Thesis Overview

This thesis concentrates on the development of modelocked semiconductor lasers that will eventually be used in an A/D converter system. Modelocked lasers exhibit the lowest jitter of optical pulse sources and can produce pulses faster than 100 GHz [9, 3]. This thesis will study the dynamics of modelocked laser diodes (MLLD) in order to improve performance and optimize design.

Chapter 1 provides motivation for the work in this thesis, as well as a brief overview

of modelocking. Chapter 2 goes into the various experimental and theoretical methods of physical laser characterization. Chapter 3 critically analyzes the split-step Fourier method and discusses its limitations. Chapter 4 presents the split-step finite difference (SSFD) method and uses the method to derive trends for design purposes. Chapter 5 summarizes the works presented in this thesis.

Chapter 2

Characterization

In order to better understand the characteristics and quality of a laser design, one must analyze the various parameters that determine the performance of the laser. For example, knowing the DC lasing threshold is important to understanding where to bias a laser when modelocking (See Chapters 3 and 4). These laser parameters can be derived through theory or determined experimentally. A careful choice of which method to use for each parameter is important. Certain parameters are easily determinable through experiment, and their results can typically be more accurate than a theoretical value. However, others are difficult to impossible to determine through experiment and a theoretical approach is necessary. This chapter first discusses the design of the lasers used in this thesis. It then introduces the various laser parameters and provides several approaches to determining them. A discussion of sources of error and the accuracy of each approach follows most techniques.

2.1 Laser Design

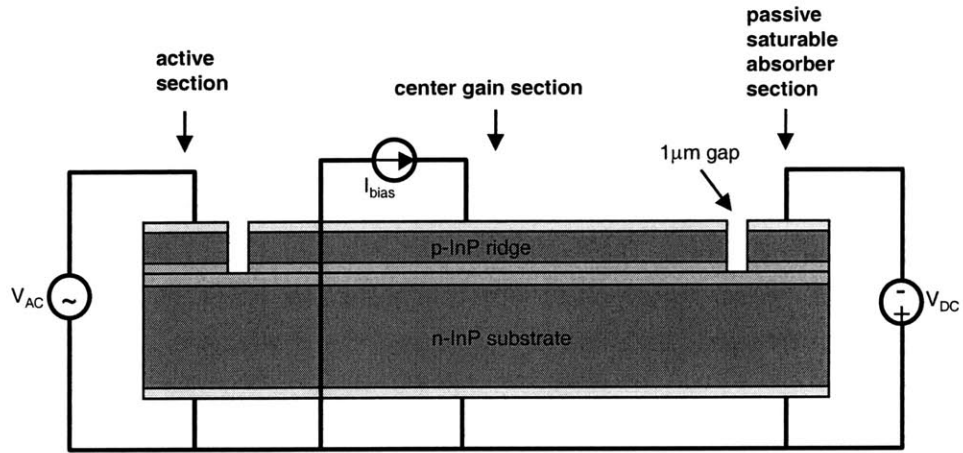
The laser used in all modelocked experiments is a 1550 nm Fabry-Perot quantum well laser designed and processed by Farhan Rana at MIT and grown by Patrick Abraham at the University of California, Santa Barbara. The substrate is $3 - 5 \times 10^{17} \text{ cm}^{-3}$ S-doped n-type InP (uncertainty due to growth calibration). The six quantum wells are 70 \AA thick $1.55 \mu\text{m}$

InGaAsP with +1% strain. The barriers are 70Å thick 1.18μm InGaAsP with no strain. The ridge layer is $5 \times 10^{18} \text{ cm}^{-3}$ Zn-doped p-type InP and is 1.5μm thick. Ridge widths were processed in 1.5 and 2.0μm widths. Figure 2-1 shows the hybrid modelocked laser profile, including the biasing scheme, and band structure.

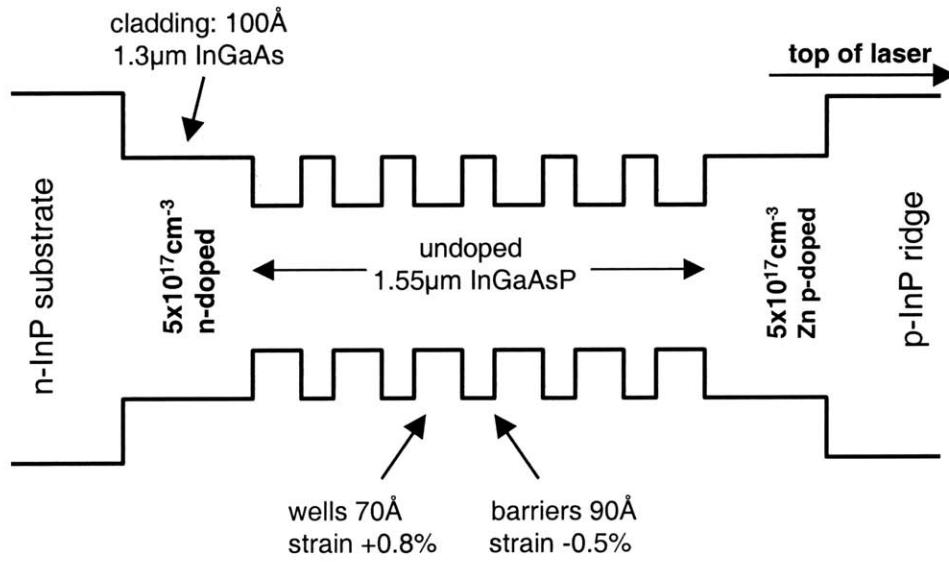
The laser is current- and index-guided by etching a ridge (1.5μm and 2.0μm widths) through the p-type InP down to but not including the active region. A very thin layer of oxide is then deposited on the entire top of the wafer. The oxide allows a layer of polyimide to be deposited. The polyimide is spun on and cured. The entire wafer surface is then planarized to the height of the ridge surface. Ohmic contacts are then deposited on the ridge surface and entire wafer backside.

All subsections of the modelocked laser, including active region, passive region, and gain region are integrated onto a single wafer. The three sections were electrically isolated by etching two 1μm wide channels through the transverse direction of the ridge (see Figure 2-2). The etching of these two channels was included in the same step as the etching of the ridge itself, therefore the channels extend down to the active region. During the polyimide spinning step, polyimide was able to fill the channel to provide a planar surface for the metallization. The ohmic contacts were deposited over the ridge areas, excluding the channels. The inter-section resistance was measured to be greater than 1MΩ.

An additional growth was prepared by E.P.I., a foundry in England. This laser design was used primarily in the characterization techniques found in this chapter. The major differences are the number and size of the quantum wells and the ridge dimensions. The bottom n-doped region was doped at $3 - 5 \times 10^{17} \text{ cm}^{-3}$. Five 60Å quantum wells with +0.8% strain were separated by 100Å barriers with -0.5% strain. The separate confinement heterostructure (SCH) layers were 120nm thick; both n- and p-type layers were doped $1 \times 10^{17} \text{ cm}^{-3}$. Both the SCH and barriers were 1.3μm InGaAsP. The p-type ridge was doped $5 \times 10^{17} \text{ cm}^{-3}$ and was 1.5μm thick and several different widths were processed, including 3, 4, and 5μm. Figure 2-3 shows the band structure of this alternate laser design.

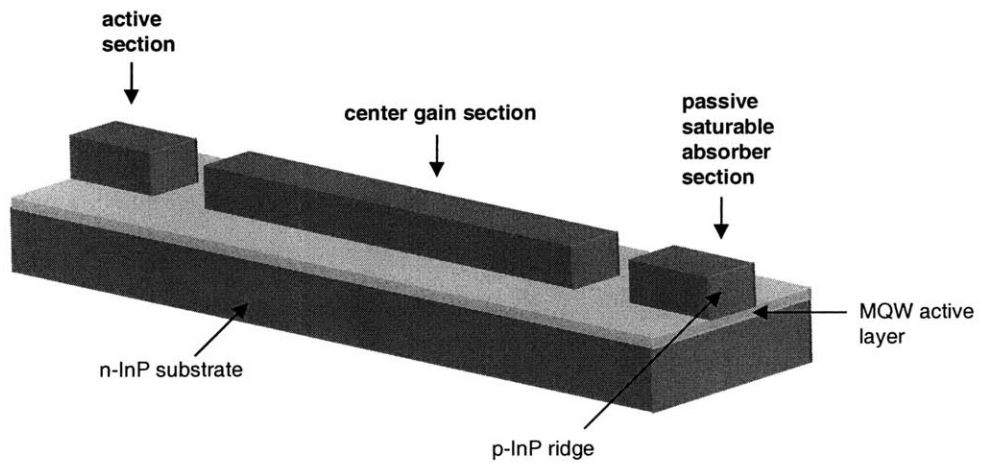


(a)

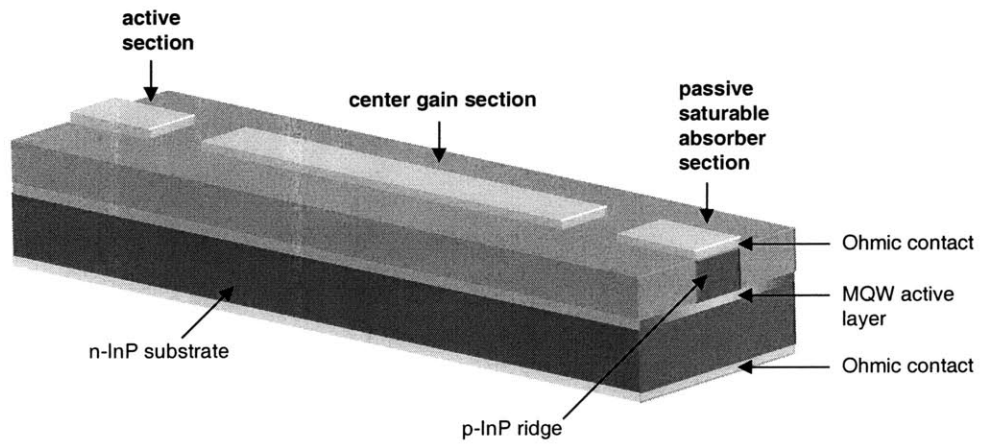


(b)

Figure 2-1: (a) Side view of laser, including biasing scheme. (b) Band structure of active region.



(a)



(b)

Figure 2-2: Schematic of hybrid laser design: (a) without (shown for detail) and (b) with polyimide planarization.

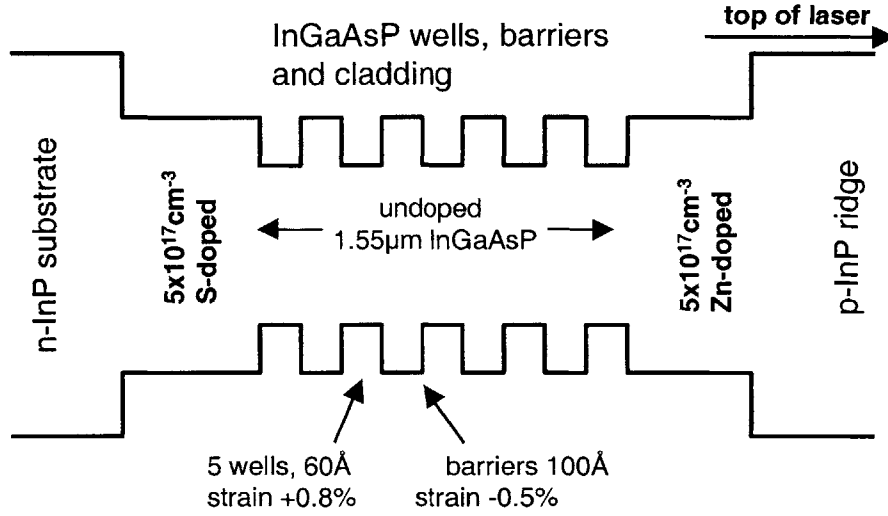


Figure 2-3: E.P.I. laser design

2.2 Laser Rate Equations

A basic but powerful model for continuous wave (CW) laser operation describes the time rate of change of the carrier concentration and photon concentration [11]. These equations are:

$$\frac{dN}{dt} = \frac{\eta_i I}{qV} - \frac{N}{\tau_c} - v_g g N_p \quad (2.1)$$

$$\frac{dN_p}{dt} = \Gamma v_g g N_p + \beta_{sp} R_{sp} - \frac{N_p}{\tau_p} \quad (2.2)$$

where N is the carrier concentration [cm^{-3}], t is time [s], η_i is the internal quantum efficiency, I is current [A], q is the fundamental electron charge [C], V is voltage [V], τ_c is the carrier lifetime [s], v_g is the photon group velocity [m/s], g is the differential gain [cm^{-1}], N_p is the photon density [cm^{-3}], Γ is the photon confinement factor, β_{sp} is the spontaneous emission factor, R_{sp} is the rate of spontaneous emission [$cm^{-3}s^{-1}$], and τ_p is the photon

lifetime [s]. The carrier lifetime, τ_c , and the photon lifetime, τ_p , are abbreviations for:

$$\frac{N}{\tau_c} = AN + BN^2 + CN^3 \quad (2.3)$$

$$\frac{1}{\tau_p} = v_g(\alpha_i + \alpha_m) \quad (2.4)$$

where for low carrier concentrations, A is the trap recombination coefficient [s^{-1}], B is the bimolecular recombination coefficient [$cm^{-3}s^{-1}$] (accounts for spontaneous emission), C is the Auger recombination coefficient [$cm^{-6}s^{-1}$] (see Section 2.4.6 for explanation at high carrier concentrations), α_i is the internal loss [cm^{-1}] (due to material loss), and α_m is the distributed mirror loss [cm^{-1}]. It is important to note that the recombination coefficients in the carrier lifetime equation only take on these definitions under low carrier densities when Boltzmann statistics hold. Under high carrier densities, the Fermi statistics of the electron occupancy take on more complicated dependencies rather than a simple integral-degree polynomial expansion. Section 2.4.6 explains this in further detail. The internal loss is due to heavy-hole to light-hole intervalence band absorption. This is a function of carrier density and photon energy, and will be described in the next section. The mirror loss, α_m , is due to the coupling of photon energy out of the two mirror facets, but the definition distributes this loss over the length of the cavity. It is defined as:

$$\alpha_m = \frac{1}{L} \ln \frac{1}{R} \quad (2.5)$$

where L is the Fabry-Perot cavity length [cm] and R is the power reflectivity of the end mirror facets. The spontaneous emission rate, R_{sp} , comes from Equation 2.3 and for low carrier densities takes the form:

$$R_{sp} = B \cdot N^2 \quad (2.6)$$

Under high carrier densities, R_{sp} has a weaker carrier density dependence as explained in Section 2.4.6.

Finally, an optical power output equation can be derived for current values above threshold:

$$P = \eta_i \left(\frac{\alpha_m}{\alpha_i + \alpha_m} \right) \frac{h\nu}{q} (I - I_{th}) \times \frac{1}{2} \quad (2.7)$$

where h is Planck's constant [$J \cdot s$] and ν is the fundamental lasing wavelength. The subscript "th" is used to represent the variable value at the threshold condition. Thus, I_{th} represents the current needed to reach the threshold condition. Frequently, we define:

$$\eta_d = \frac{\eta_i \alpha_m}{\alpha_i + \alpha_m} \frac{1}{2} \quad (2.8)$$

where η_d is known as the differential quantum efficiency. Since spontaneous emission dominates for sub-threshold regimes, a power/facet equation below threshold can be derived:

$$P_{sp} = \eta_c \eta_i \eta_r \frac{h\nu}{q} I \quad (2.9)$$

where η_r is the radiative efficiency and η_c is the collection efficiency. η_r is the fraction of carrier recombination that is accounted for by spontaneous emission:

$$\eta_r = \frac{R_{sp}}{(N/\tau_c)} \quad (2.10)$$

A brief explanation of each term in Equations 2.1 and 2.2 are as follows. In the carrier rate equation, the first term on the right-hand side accounts for carrier injection into the active region from a current source. The second term accounts for carrier relaxation due to interactions in the semiconductor. The third term accounts for carrier recombination due to stimulated emission from the lasing modes. In the photon rate equation, the first term on the right-hand side accounts for the photon creation rate due to stimulated emission into the lasing mode. The second term accounts for spontaneous emission coupling into

the lasing mode. The third term accounts for photon absorption losses due to interactions with the semiconductor. Further information on the laser rate equations can be found in Chapter 2 of [11].

It is important to characterize these laser parameters to better understand the quality of its design and help explain its performance. The remainder of this chapter is devoted to the determination of the parameters which are found in the laser rate equations and their supplemental equations.

2.3 Theoretically-Derived Parameters

2.3.1 Group Velocity (v_g)

The photon group velocity represents the speed at which photon energy propagates. In terms of laser pulses, this is the velocity of the pulse as it propagates within the semiconductor. This is different from phase velocity, which is the speed at which the carrier frequency (in this case, the frequency that corresponds to a 1550nm free-space wavelength) propagates. The group velocity is determined by knowing the group index of the material. Since the laser is heterogeneous, the index is spatially dependent. The group index is found by determining the photon field profile within the laser cavity and performing a weighted average of the different indexes by the percentage photon density of each section. Since the index is wavelength dependent (due to material dispersion effects), the group velocity, v_g , will be also:

$$v_g = \frac{c}{n_g} \quad (2.11)$$

where n_g is the group velocity. Since the wavelengths within the linewidth of a laser typically span a short range, the group velocity can usually be approximated as constant. A method to determine group index is explained in Section 2.4.4.

2.3.2 Confinement Factor (Γ)

The confinement factor, Γ , represents the percentage of the steady-state photon energy that lies in the active region of the semiconductor. In a Fabry-Perot laser, the photon field propagates along the axial direction (the axis as defined in the direction of the laser ridge, or z-axis, as conventionally defined). The active region is defined as the region in the laser that stimulated emission occurs. This will be within the quantum wells, since they provide electron and hole confinement. Since the active region extends the entire axial length as well as the entire plane of the laser, the confinement of the laser field in these two directions is 100%. The quantum wells, however, only cover a small portion of the vertical direction and therefore the photon field extends well beyond them. The confinement factor can be determined theoretically by knowing the structure dimensions and solving for the steady-state photon field as confined by the cladding and quantum wells. This is accomplished by performing a 2-dimensional solution of the photon field within the cavity. Once the field profile is determined, the percentage of the photon field that lies within the multiple quantum wells is added up, which becomes the confinement factor. This simulation was written by Farhan Rana. Figure 2-4 shows this solution for the laser under study. Using the 2-D solver, $\Gamma = 0.00918$ for each of the quantum wells in the E.P.I. laser. Summing up the total confinement factor for all five quantum wells yields a total $\Gamma = 0.0459$.

2.3.3 Mirror Reflectivity (R)

The mirror reflectivity can be determined simply by knowing the group index of the photon field within the semiconductor, as well as the index outside the cavity. A simple boundary condition solution gives the transmission and reflection through a mirror facet.

$$r = \frac{n_1 - n_2}{n_1 + n_2} \quad (2.12)$$

$$t = \frac{2n_2}{n_1 + n_2} \quad (2.13)$$

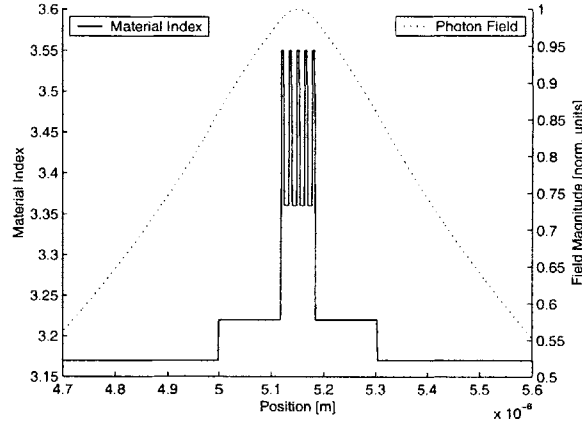


Figure 2-4: Field and index profile in laser core, E.P.I. growth

where n_1 and n_2 are the group indices of the initial material and transmitted material. Typically, the initial material is semiconductor and the transmitted material is air. r and t represent the field reflectivity and transmission, respectively. R represents the power reflectivity where $R = |r|^2$. T is the power transmission where $T = |t|^2$. The variability of this value usually comes from the quality of the mirror facets. A cleanly cleaved facet should give a near-theoretical value. For a group index of 3.7, the power reflectivity, $R = 0.33$. By measuring the length of the laser, a theoretical value for α_m can be determined using Equation 2.5.

2.4 Experimental Parameters

2.4.1 Loss (α_i) and Internal Quantum Efficiency (η_i) Measurements

By examining the above-threshold power equation (Equation 2.7), it is easy to find a differential slope of power per facet to current:

$$\frac{dP}{dI} = \eta_d \frac{h\nu}{q} \frac{1}{2} \quad (2.14)$$

Figure 2-5 shows how dP/dI is found.

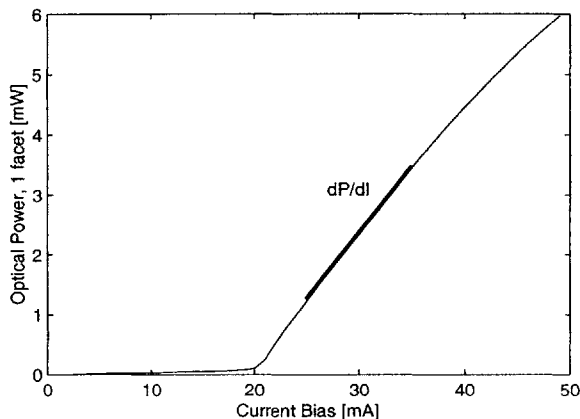


Figure 2-5: Typical Power vs. Current laser curve and representation of dP/dI , E.P.I. growth

The internal quantum efficiency, η_i , and the material loss, α_i , can be found using a commonly known technique of comparing the inverse mirror loss and differential quantum efficiency [36]. This method assumes no dependence on length for these two parameters. However, the mirror loss, α_m , changes as the length of the laser changes. In order to determine η_i and α_i we need two non-degenerate equations, obtainable by choosing two different-length lasers made from the same design. This is obtainable by cleaving two different lengths from the same material. Since data have a margin of error, we can increase the accuracy of this measurement by increasing the number of data points. This is accomplished by cleaving multiple laser bars of different lengths and measuring their η_d . From these η_d measurements their corresponding α_m can be determined. Using Equation 2.8, we can write a linear equation between $1/\eta_d$ and $1/\alpha_m$:

$$\frac{1}{\eta_d} = \frac{\alpha_i}{\eta_i} \frac{1}{\alpha_m} + \frac{1}{\eta_i} \quad (2.15)$$

A two-parameter linear fit can then be made on $1/\eta_d$ versus $1/\alpha_m$ to obtain values for η_i and α_i . Figure 2-6 shows parameter fits for the modelocked laser material.

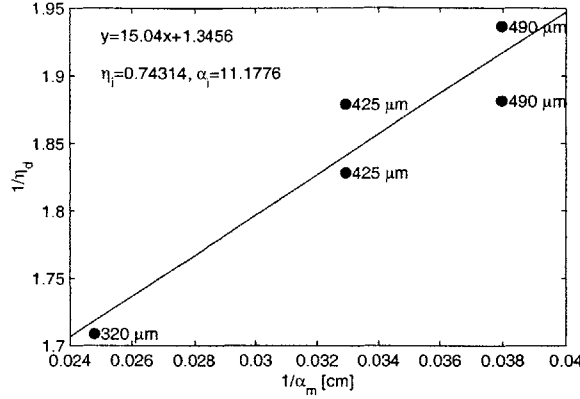


Figure 2-6: Linear fit of $1/\eta_d$ versus $1/\alpha_m$ to determine α_i and η_i , E.P.I. growth

The values obtained through this method as shown in the graph are $\eta_i = 0.74$ and $\alpha_i = 11.2$. A confidence estimation can be performed on this method by calculating the magnitude of deviation on the calculated results due to deviations in the experimental data.

A quantification of the error in η_i and α_i respectively is:

$$(\Delta\eta_i)^2 = \left[\Delta\alpha_m \left(\frac{\partial\eta_i}{\partial\alpha_m} \right) \right]^2 + \left[\Delta\eta_d \left(\frac{\partial\eta_i}{\partial\eta_d} \right) \right]^2 \quad (2.16)$$

$$= \left[\Delta\alpha_m \left(\frac{\eta_d\alpha_i}{\alpha_m^2} \right) \right]^2 + \left[\Delta\eta_d \left(1 + \frac{\alpha_i}{\alpha_m} \right) \right]^2 \quad (2.17)$$

$$(\Delta\alpha_i)^2 = \left[\Delta\alpha_m \left(\frac{\partial\alpha_i}{\partial\alpha_m} \right) \right]^2 + \left[\Delta\eta_d \left(\frac{\partial\alpha_i}{\partial\eta_d} \right) \right]^2 \quad (2.18)$$

$$= \left[\Delta\alpha_m \left(\frac{\eta_i}{\eta_d} - 1 \right) \right]^2 + \left[\Delta\eta_d \left(\frac{\alpha_m\eta_i}{\eta_d^2} \right) \right]^2 \quad (2.19)$$

where the Δx values signify the deviation from the true value of x . By the chain rule, we can expand the $\Delta\alpha_m$ into terms which are directly measurable:

$$(\Delta\alpha_m)^2 = \left[\Delta R \left(\frac{\partial\alpha_m}{\partial R} \right) \right]^2 + \left[\Delta L \left(\frac{\partial\alpha_m}{\partial L} \right) \right]^2 \quad (2.20)$$

$$= \left[\Delta R \left(\frac{1}{LR} \right) \right]^2 + \left[\Delta L \left(\frac{1}{L^2} \ln R \right) \right]^2 \quad (2.21)$$

For typical values: $L = 300\mu m$, $n_g = 3.2$, $\eta_i = 0.74$, $\eta_d = 0.6$, we obtain $R = 0.2744$, $\alpha_m = 43cm^{-1}$ and

$$\Delta\alpha_i = \sqrt{(28.3\Delta R)^2 + (335\Delta L)^2 + (88.6\Delta\eta_d)^2} \quad (2.22)$$

For a value of $\alpha_i = 10cm^{-1}$, we can estimate the percentage error on α_i due to a 10% error on each of the measured quantities. If

$$\Delta R = 0.1R \Rightarrow \frac{\Delta\alpha_i}{\alpha_i} = 0.078 \quad (2.23)$$

$$\Delta L = 0.1L \Rightarrow \frac{\Delta\alpha_i}{\alpha_i} = 0.10 \quad (2.24)$$

$$\Delta\eta_d = 0.1\eta_d \Rightarrow \frac{\Delta\alpha_i}{\alpha_i} = 0.53 \quad (2.25)$$

This result shows that the measurement of η_d is crucial to obtaining a good value for α_i . A similar estimation for the error in η_i give us

$$\Delta\eta_i = \sqrt{(0.39\Delta R)^2 + (4.64\Delta L)^2 + (1.23\Delta\eta_d)^2} \quad (2.26)$$

Performing the same error estimation:

$$\Delta R = 0.1R \Rightarrow \frac{\Delta\eta_i}{\eta_i} = 0.014 \quad (2.27)$$

$$\Delta L = 0.1L \Rightarrow \frac{\Delta\eta_i}{\eta_i} = 0.019 \quad (2.28)$$

$$\Delta\eta_d = 0.1\eta_d \Rightarrow \frac{\Delta\eta_i}{\eta_i} = 0.10 \quad (2.29)$$

This shows that the calculation of η_i is not very dependent on the accuracy of the length or the reflectivity, and has a moderate dependency on η_d . There is high confidence in the measurement of the length to within $10\mu m$. The index is calculable theoretically (see Section 2.4.4) and is accurate within 10%. The largest error occurs with the measurement of η_d . As shown in Figure 2-5, the slope bends as the bias increases, due to laser heating

reducing the internal quantum efficiency. Therefore, the bias at which to measure the slope is not trivially determinable. [49] also discusses the error in this technique.

Note that α_i and η_i are temperature dependent. This technique assumes that there is a weak temperature dependence and that the temperature of the laser changes very little over the range of biases. Note also that the parameter, α_i , is wavelength dependent and that this method is suitable to determine α_i only for the lasing wavelength. A more powerful method is describe in Section 2.4.5.

2.4.2 Derivation of Fabry-Perot Modes

A derivation of the Fabry-Perot modes will shed light upon a method to determine the group index and loss parameters of the material. It is assumed that the photon fields exist within the laser cavity as steady-state standing wave patterns. Given an initial electric field that propagates along the axial direction of the Fabry-Perot cavity, one can find the total transmission assuming partially reflective mirrors. Figure 2-7 shows a Fabry-Perot cavity of length L and field transmission coefficients t_1 and t_2 .

Without loss of generality, E_0 originates at the left-hand mirror and propagates towards the right. It picks up a phase change as it propagates through the Fabry-Perot cavity; for a dz change in distance, it picks up $e^{-jk dz}$ phase, where k is the wave number within the cavity and

$$k = 2\pi n_g / \lambda \quad (2.30)$$

where λ is the free-space wavelength. At each of the facets, the electric field is reflected back by $r_{1,2}$ where $|r_{1,2}|^2 = 1 - |t_{1,2}|^2$ and transmitted through the facet by $t_{1,2}$. Hence, after one reflection off the right-hand wall, the transmitted field is:

$$E_t = E_0 e^{-jkL} t_2 \quad (2.31)$$

The reflected portion makes another round-trip through the cavity. After two reflections

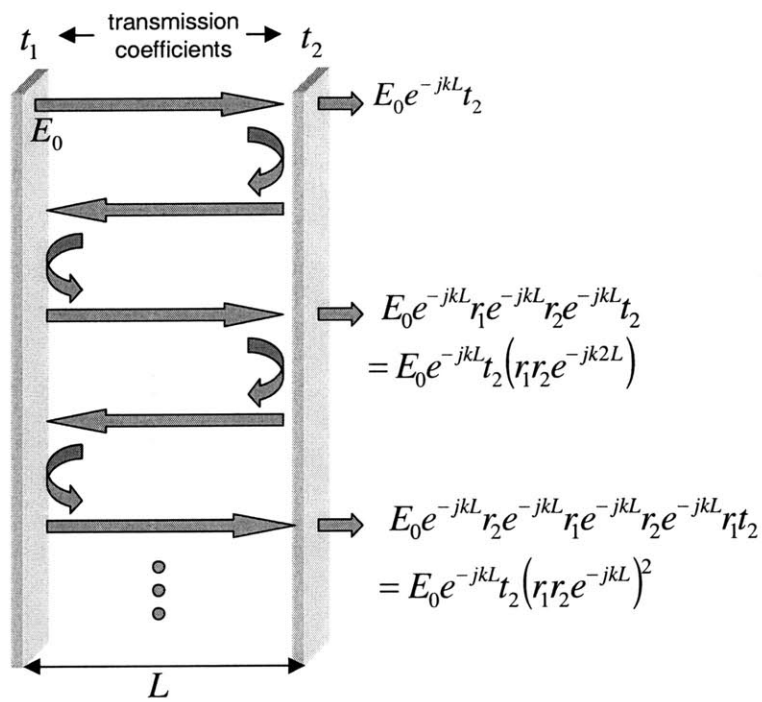


Figure 2-7: Representation of Fabry-Perot modes

off the right-hand facet, the transmitted field is the first plus the second:

$$E_t = E_0 e^{-jkL t_2} + E_0 e^{-jkL} r_2 e^{-jkL} r_1 e^{-jkL} t_2 \quad (2.32)$$

The pattern is evident. In closed form, the entire transmitted field is:

$$E_t = E_0 e^{-jkL t_2} \sum_{n=0}^{\infty} \left(r_1 r_2 e^{-j2kL} \right)^n = \frac{E_0 e^{-jkL t_2}}{1 - r_1 r_2 e^{-j2kL}} \quad (2.33)$$

The power density, P [W/m^2], is:

$$P = \frac{|E_t|^2}{\mu c} \quad (2.34)$$

where μ is the magnetic permeability constant [H/cm]. Therefore, the optical power detected is an explicit function of wave number and therefore, of wavelength:

$$P = \frac{|E_0 t_2|^2}{1 + R_1 R_2 - 2r_1 r_2 \cos(2kL)} \frac{1}{\mu c} \quad (2.35)$$

where k is defined in Equation 2.30.

Putting the proportionality constants aside, it can be seen that this function will be periodic with respect to λ . The function will be at its maximum when the cosine term is at its smallest, or 1 and the function will be at its minimum when the cosine term equals -1 . This corresponds to:

$$\text{Maximum : } 2k_{max}L = 2\pi m \quad (2.36)$$

$$\text{Minimum : } 2k_{min}L = \pi(2m + 1) \quad (2.37)$$

where m is any integral number. Solving for the wavelengths which give maximums and

minimums:

$$\lambda_{max} = \frac{2Ln_g}{m} \quad (2.38)$$

$$\lambda_{min} = \frac{4Ln_g}{2m + 1} \quad (2.39)$$

A representation of this is shown in Figure 2-8

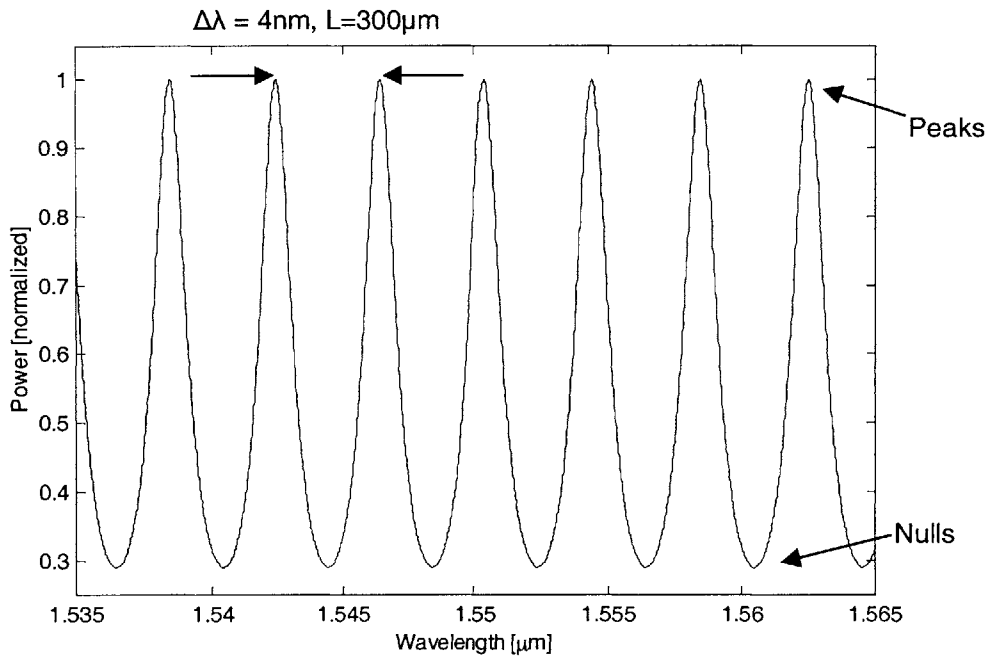


Figure 2-8: Simulation of Fabry-Perot field spectrum in $n_g = 1$ medium.

Further insight into the Fabry-Perot modes comes when we translate the peak wavelengths into their corresponding frequencies:

$$\omega_{max} = \frac{2\pi c}{\lambda_{max}} = \frac{c2\pi m}{n_g 2L} \quad (2.40)$$

It can be seen that the maximum frequencies occur at integral multiples of the round-trip frequency ($2\pi c/n_g 2L$) of the cavity. The peaks and nulls represent constructive and

destructive interference due to the feedback of the cavity boundaries.

2.4.3 Measuring the Fabry-Perot Modes

In order to experimentally observe the Fabry-Perot modes of a laser cavity, it is necessary to obtain the power versus wavelength information of the output light. The Fabry-Perot modes depend on the gain structure of the laser. Therefore, it is best to examine the optical spectrum below threshold. The spontaneous emission of the laser will still have a wavelength-varying super-structure due to wavelength-dependent gain (see Figure 2-10), but the gain varies slowly with respect to the Fabry-Perot mode spacing. A problem may arise as the laser length becomes very short, but typically the laser will not lase for lengths where this is a concern. Also, if the laser length is too long, the Fabry-Perot modes will not be resolvable within the resolution bandwidth of the measuring instrument.

The experimental setup included a Hewlett-Packard 70950B optical spectrum analyzer (OSA), with a resolution bandwidth of 0.08 nm, which was used to capture the optical power from one of the laser facets. The light was coupled into a multi-mode fiber through a pair of lenses anti-reflection (AR) coated at 1550nm. The lenses' foci were adjusted by mounting the lenses onto 3-axis translation stages. Figure 2-9 shows a schematic of the test setup.

This setup allowed for enough spontaneous emission to register above the noise floor of the OSA, however, the tail ends of the spectrum, away from the gain peak, tend to become noisy, which shows up as spurious data in measurement techniques that employ the Fabry-Perot modes. Since this technique is valid for all current bias levels below threshold, near-zero current levels scans can be attempted. However, the amount of light coupled into the OSA will tend to become very noisy, especially for the lower current bias levels. At times, scan averaging was necessary to decrease the noise level so that a suitable measurement could be performed. In order to decrease the time necessary for a complete scan and to improve the resolution of the scan, the entire wavelength range was typically split into smaller wavelength portions, in which scans were performed in each. Figure 2-10 shows an

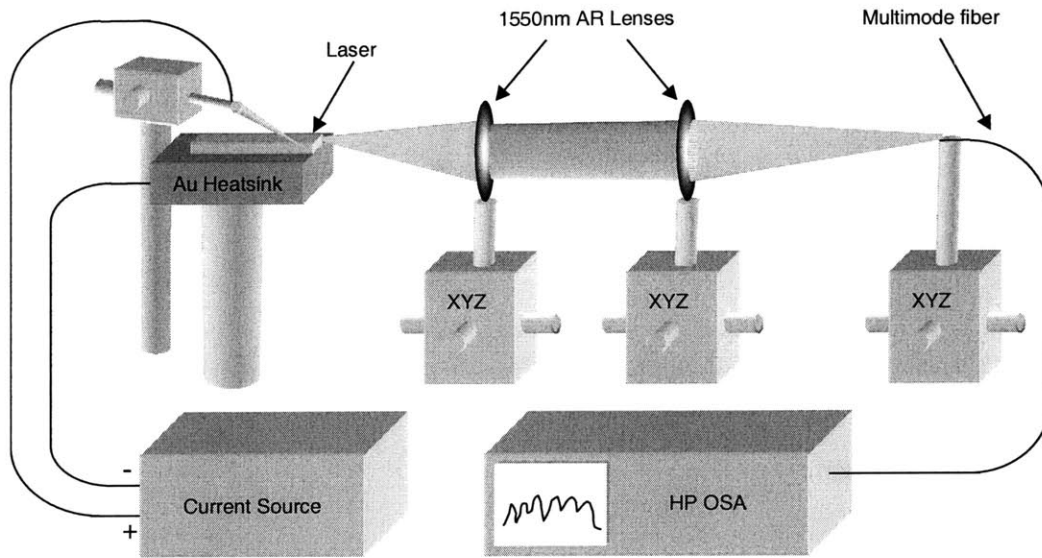


Figure 2-9: Schematic of test setup

example of an OSA trace that shows the Fabry-Perot peaks as well as the gain structure of the laser. Typically, this range would be split into small 10-20nm scan ranges which would be pieced together in the end.

Error introduced by the measurement device's resolution bandwidth (in this case 0.08 nm) can be analyzed by understanding how the error is introduced. In order to determine the optical power at each given wavelength, the OSA integrates the optical power over a non-zero interval of wavelength. The larger the interval, the larger the power registered, since more light will be integrated. On a first-pass approximation, the integrating window can be modeled as a square window centered around the wavelength in concern. Essentially, the ideal spectrum is convolved with the window to produce the recorded spectrum. A deconvolution with the assumed window shape will give an estimate of the ideal spectrum, minus the error due to the OSA's resolution bandwidth. Simulations of Fabry-Perot modes of this laser system with and without the resolution bandwidth error were performed. The error for loss measurements (see Section 2.4.5) was found to be less than 4% for typical val-

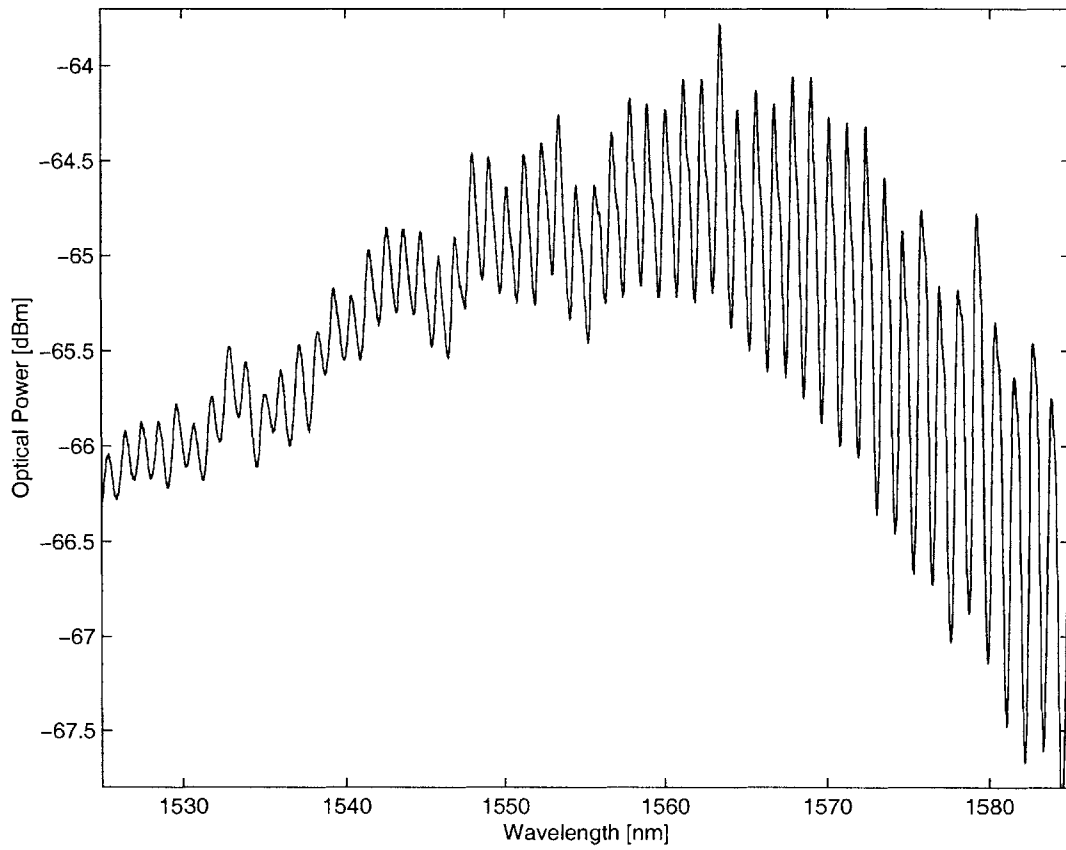


Figure 2-10: Typical OSA trace for a laser below threshold, showing the Fabry-Perot resonances, E.P.I. growth, $L=300\mu m$, width= $5\mu m$, 10mA bias, $20.2^{\circ}C$

ues. Therefore, the resolution bandwidth error from the measurement device was neglected in all future measurements. Further analysis on the error due to resolution bandwidth can be found in [8], which also provides a variant method that is less sensitive to noise. A theoretical quantification of the error can be found in [32] where the method described by Hakki and Paoli and in [8] are compared.

2.4.4 Group Index Measurements

In order to measure the group index of the laser, we can take advantage of the Fabry-Perot mode structure to give us insight to the characteristics of the cavity. This is a standard method of determining index of materials. By knowing the wavelengths of two adjacent peaks of the Fabry-Perot mode structure, one can determine the group index, n_g . Given two adjacent wavelengths, λ_1 and λ_2 , where $\lambda_1 = \frac{2Ln_g}{m+1}$ and $\lambda_2 = \frac{2Ln_g}{m}$:

$$(m + 1) - (m) = \left(\frac{2Ln_g}{\lambda_1} \right) - \left(\frac{2Ln_g}{\lambda_2} \right) = 1 \quad (2.41)$$

which gives us:

$$n_g = \frac{\lambda_1 \lambda_2}{2L\Delta\lambda} \quad (2.42)$$

where $\Delta\lambda = \lambda_2 - \lambda_1$. The wavelength that corresponds to this group index is approximately the average of λ_1 and λ_2 . The group index can now be found as a function of wavelength. Figure 2-11 shows the group index as a function of wavelength.

The group index for this laser structure around the lasing wavelength is approximately $n_g = 3.6 - 3.7$. This matches well with a group index of 3.7 cited in the literature for a similar InGaAsP material system [31].

2.4.5 Loss/Gain Curve Measurements

The Fabry-Perot modes can be used to perform overall gain spectrum measurements [21]. This measurement technique was developed by B. Hakki and T. Paoli in 1973. The code is

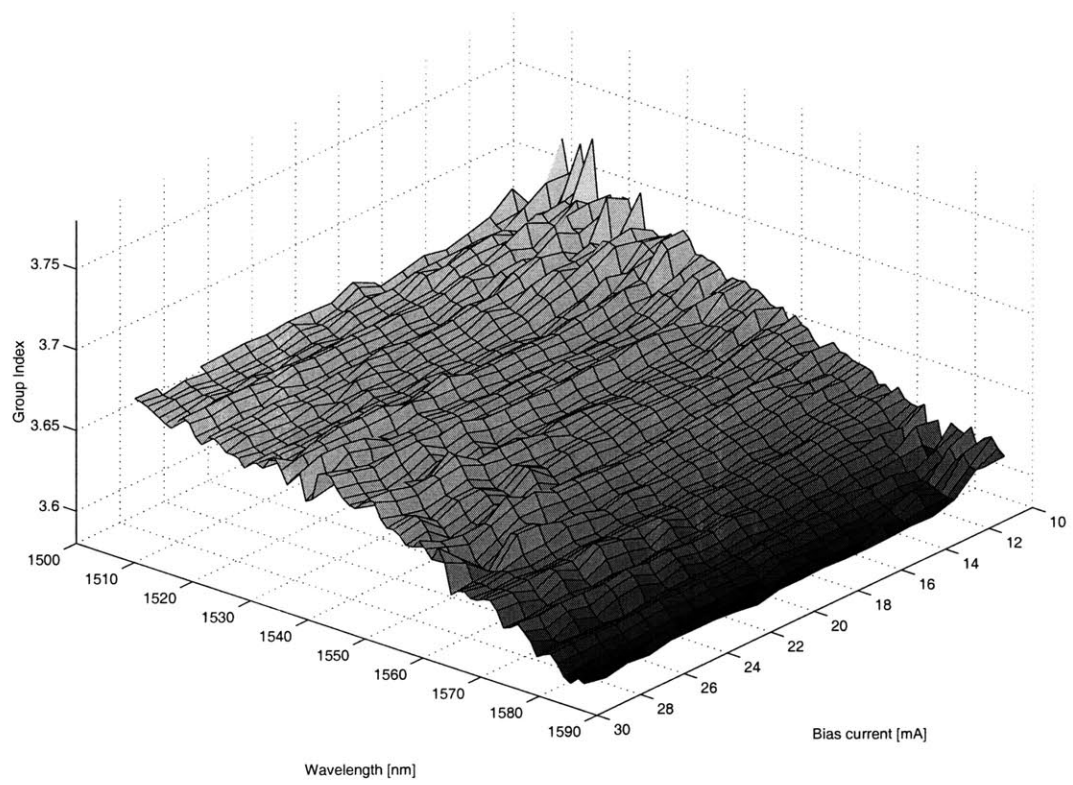


Figure 2-11: Index spectrum for different biases, E.P.I. growth, $L = 300\mu\text{m}$, $W = 5\mu\text{m}$, $T = 293.2\text{K}$

found in Appendix A, written in **Matlab**. We can modify Equation 2.33 to include gain within the cavity due to material absorption. We can redefine k to include an imaginary term that will account for gain:

$$k \Rightarrow k + \frac{1}{2}j\alpha(\lambda) \quad (2.43)$$

where we have defined the overall gain coefficient, α , to be wavelength-dependent. Hence, the total field transmission becomes:

$$E_t = \frac{E'_0}{1 - r_1 r_2 e^{-j2kL} e^{\alpha(\lambda)L}} \quad (2.44)$$

where we have defined $E'_0 = E_0 e^{-j2kL} e^{\alpha(\lambda)L} t_2$ for simplicity. Minimum and maximum field transmission values can be found by varying k , as above.

$$\text{Maximum : } E_{max} = \frac{E'_0}{1 - r_1 r_2 e^{\alpha(\lambda_{max})L}} \quad (2.45)$$

$$\text{Minimum : } E_{min} = \frac{E'_0}{1 + r_1 r_2 e^{\alpha(\lambda_{min})L}} \quad (2.46)$$

We will assume that if this Fabry-Perot minimum and maximum are adjacent then the gain parameter is slowly-varying enough to allow us to say that they will be equal for the two: $\alpha(\lambda_{max}) = \alpha(\lambda_{min}) \equiv \alpha(\lambda)$. Now, defining the power density that corresponds to these two as P_{max} and P_{min} :

$$P_{max} = \left(\frac{|E'_0|}{1 - r_1 r_2 e^{\alpha(\lambda)L}} \right)^2 \quad (2.47)$$

$$P_{min} = \left(\frac{|E'_0|}{1 + r_1 r_2 e^{\alpha(\lambda)L}} \right)^2 \quad (2.48)$$

we can then obtain the gain formula:

$$\alpha(\lambda) = -\frac{1}{L} \ln \left(\sqrt{R_1 R_2} \frac{\sqrt{P_{max}} + \sqrt{P_{min}}}{\sqrt{P_{max}} - \sqrt{P_{min}}} \right) \quad (2.49)$$

Since the power term is a fraction, only the ratio of the peak and null powers are necessary for this technique to work, which is where the utility of this function lies. We can allow for coupling loss to the OSA without undermining the technique. The same data acquisition technique used for determining the group index was used here as well. Since the wavelength for a determined gain parameter is approximate, the gain can be measured in several ways: using a peak and 1) its left-hand null, 2) its right-hand null, or 3) averaging the two. Negligible difference was found in the different methods. This supports the argument that the net gain curve varies slowly with respect to the Fabry-Perot mode spacing. Figure 2-12 shows a typical net gain curve for a short Fabry-Perot laser made from the same material as the modelocked laser. Another note is that this method works in sub-threshold conditions. In a laser's lasing mode the gain cannot be calculated since the lasing peak adds too much structure to the gain curve. However, useful data can be pulled from everywhere save the gain peak. One can see the clamping of the gain peak at 24mA.

The net gain curve actually represents

$$\alpha(\lambda) = \Gamma g(\lambda) - \alpha_i \quad (2.50)$$

since the loss is attenuated with rising gain. For InGaAsP materials, α_i is relatively constant over large wavelengths [20], while $g(\lambda)$ is not. Thus, knowing α_i and Γ allows us to find $g(\lambda)$. The theoretical method of finding Γ is explained in Section 2.3.2. α_i can be found through the method described in Section 2.4.1. Another method of finding α_i is through analysis of the gain curve. Gain is positive when there is carrier population inversion and negative when there are fewer carriers than electron-hole pairs. In the former case, there are enough carriers for stimulated emission to win over photon absorption by electron-hole pairs. In the latter, the opposite is true. For wavelengths larger than the bandgap wavelength, there should theoretically be zero quantum well absorption, since the light is too low energy to be absorbed by a valence electron. So, $g(\lambda)$ should go to zero at higher wavelengths (smaller energy) and α_i should be the dominant term. If one examines the net gain curve for various bias currents, the losses should therefore converge to a single value for wavelengths well

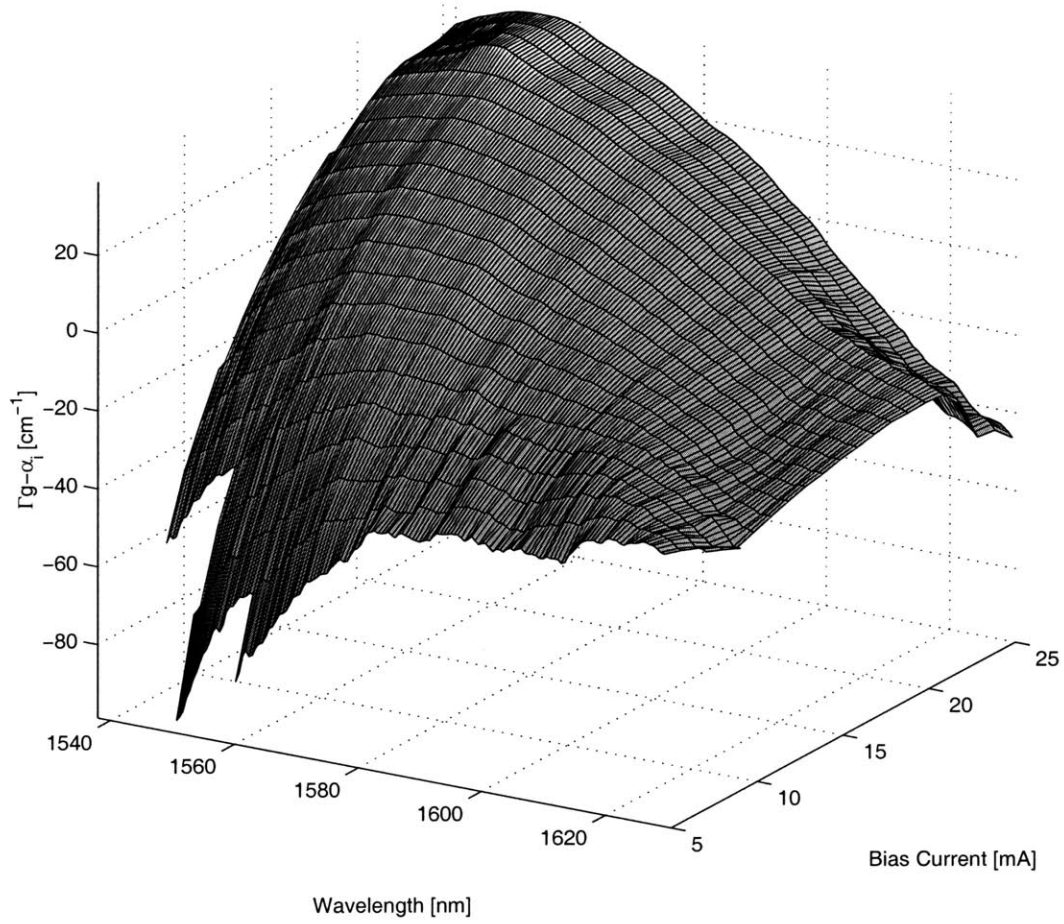


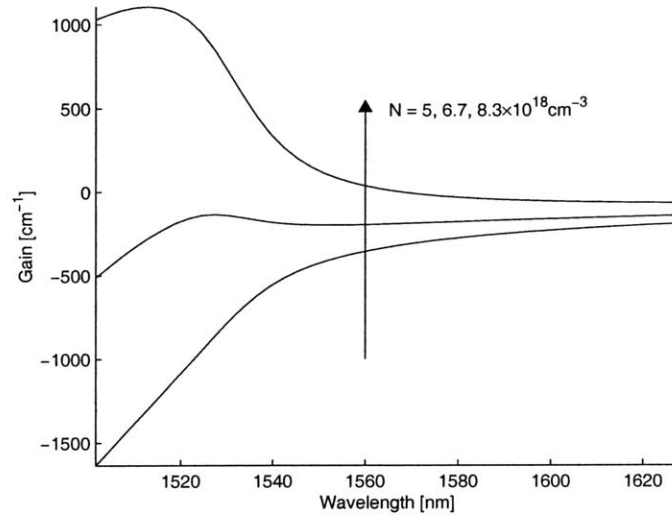
Figure 2-12: Overall material gain ($\Gamma g - \alpha_i$) for different biases, E.P.I. growth $L = 320\mu\text{m}$, $W = 3\mu\text{m}$, $T = 293.2\text{K}$

above 1550nm. Figure 2-12 somewhat shows this convergence if examined for wavelengths above 1620nm. However, it can be seen that the convergence is not perfect, rather there seems to be a large range of loss values that cover the range of biases.

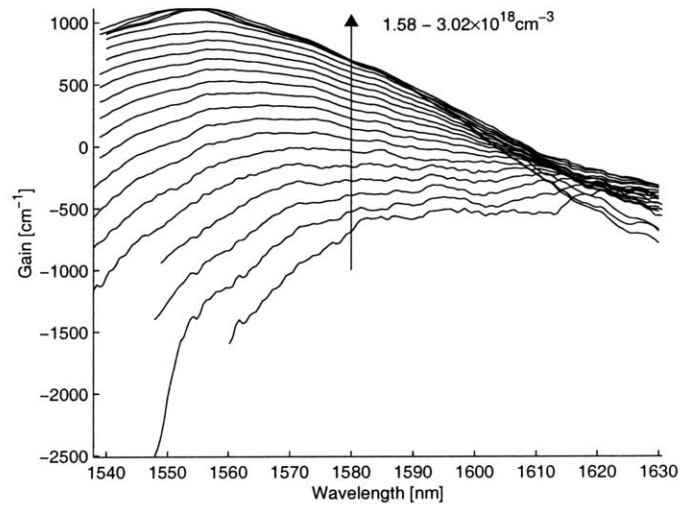
By adding a theoretically derived internal loss, α_i , and dividing by the confinement factor, Γ , we can plot the gain spectra, as shown in Figure 2-13(b). Using a gain simulation written by Farhan Rana, we can compare the experimentally extracted gain with our theoretical expectations (Figure 2-13(a)). We can compare expected carrier densities by converting the current bias to carrier density using the assumption that steady-state, sub-threshold carrier injection equals carrier recombination (See Equation 2.53. This calculation assumes recombination coefficients of: $A = 1 \times 10^8 s^{-1}$, $B = 1 \times 10^{-10} cm^3 s^{-1}$, $C = 1 \times 10^{-28} cm^6 s^{-1}$. Note the shift in the gain peak and the difference in carrier density by a factor of approximately three. Note also that the experimental curves do not converge to $g = 0$ for higher wavelengths as does the theoretical curves. It is likely that there are alternate sources of loss within the cavity that should account for the discrepancy between the experiment and theory.

Experimental loss data from Casey et al. [20] on bulk p-type InP can be used to compare with this value for α_i . Since the doping concentration is different for various waveguide layers, an effective α_i can be found by weighting the different sections' α_i by their respective confinement factor. Each section's α_i can be determined by interpolating loss spectra from the data in [20]. Both sets of data are plotted in Figure 2-14, along with the loss curve taken at 17mA bias. The x-axis has been converted from wavelength to energy. The graph shows that the experimental data does not match well with the theoretically calculated loss curves. As the energy decreases (wavelength increases) the loss takes a steeper dependence as seen in the slope of the experimental loss curve. Also, the loss is overall much greater.

It is possible that the sensitivity of the measurement falls off significantly in the range of wavelengths that this should happen; this leads to error in the loss determination and convergence may not show up. It is also apparent from Figure 2-12 that the loss does not



(a)



(b)

Figure 2-13: Gain (g) spectrum from (a) theoretical simulation (b) Hakki-Paoli experimental extraction. E.P.I. growth $L = 320\mu m$, $W = 3\mu m$. Theory: $T = 300K$. Experiment: $T = 293.2K$

converge due to the unusually large wavelength dependence on the loss at high wavelengths. Using this method, a value of α_i should lie between $\alpha_i = 20 - 30\text{cm}^{-1}$. This value is also different from the α_i that was measured using the method described in Section 2.4.1, which measured $\alpha_i = 11.2\text{cm}^{-1}$ (Dotted line in Figure 2-14).

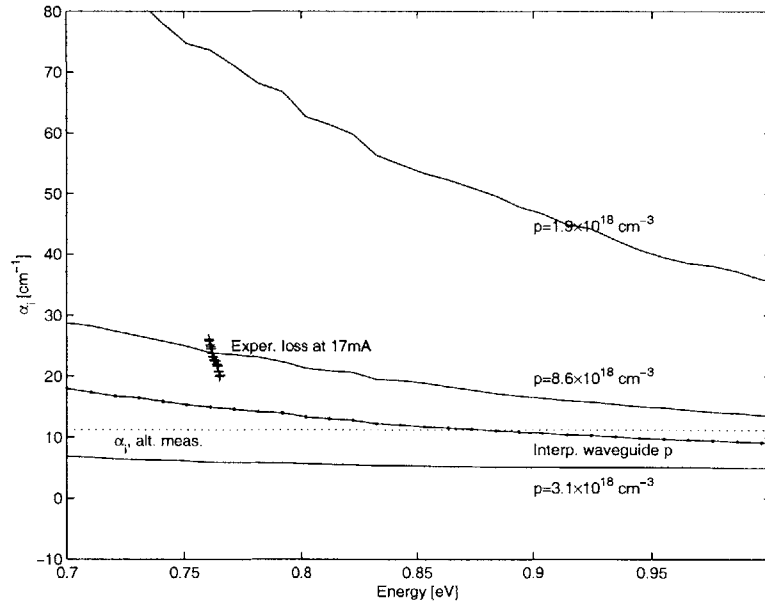


Figure 2-14: Theoretical loss curves and experimental loss, E.P.I. growth, $L = 320\mu\text{m}$, $W = 3\mu\text{m}$, $T = 293.2\text{K}$, $I = 17\text{mA}$

The accuracy of this method is analyzed in [45]. Their analysis shows that lasers with typical reflection coefficients may underestimate the gain curve as it falls away from the peak gain. The measurement technique assumes a pure axial wave. However, there are transverse k-vector modes that are captured by the measurement device since the spontaneous emission light is not captured at a singularity. Their methods of correction for this involve shrinking the collection device's aperture size (using a single-mode fiber), or using a spatial mode filter between the laser facet and the collection device aperture.

2.4.6 Recombination Coefficients

The carrier lifetime is highly dependent on the carrier concentration, as shown in Equation 2.3. Equation 2.3 describes the carrier density dependency on the carrier lifetime under the Boltzmann approximation (low carrier densities). As the carrier density increases, the Boltzmann approximation breaks down and must be replaced by the full Fermi-Dirac distribution function. This causes each term to take on a weaker dependency on N . For example, the spontaneous emission rate can be approximated with a more complete polynomial fit [11]:

$$R_{sp} = B_0 \cdot N^2 - B_1 \cdot N \quad (2.51)$$

Each of the other terms can similarly be expanded, including lower-order terms. When summed together, an equation of the form of Equation 2.3 can still be used, except the coefficients no longer stand for their original definitions. In essence, each new term of A , B , and C contain dependencies from each recombination force.

Carrier Lifetime Determination through Gain

Several techniques exist for measuring the carrier lifetime, τ_c , in semiconductor lasers. The most basic method is by using pump-probe techniques to directly measure the decay rate of the carriers [65]. A curve fit can be performed on the decaying carrier density to determine the recombination coefficients. Another high-speed method involves measuring the turn-on time between electrical step input and the corresponding optical output [12]. An all-electrical method was developed by G.E. Shtengel et al. that employs an R-L-C modeling of the laser [57]. The parameters for this model are determined by measuring the electronic frequency response of the laser and fitting the parameters to the real and imaginary parts of the frequency response.

For bias current levels well below threshold, the stimulated emission term, $v_g g N_p$, can be neglected in Equation 2.1. In steady-state, the carrier population does not change and

the current is completely accounted for by carrier recombination:

$$\frac{dN}{dt} = \frac{\eta_i I}{qV} - \frac{N}{\tau_c} = 0 \quad (2.52)$$

Replacing N/τ_c with the individual recombination terms, we get:

$$\frac{\eta_i I}{qV} = \frac{N}{\tau_c} = AN + BN^2 + CN^3 \quad (2.53)$$

A method for determining N for a given current bias that does not require high-speed methods is by referencing a peak gain vs. carrier density graph. Since we can find the peak gain for a given current bias by examining the loss curves found in the previous section, we can find the carrier density for that current bias through a g vs. N graph (Figure 2-15). This method was first performed by Ongstad et al. in 1998 [48]. The g vs. N graph was theoretically calculated by Farhan Rana at different active region temperatures. Negligible core heating was assumed, so a temperature of 300K was used for all recombination calculations.

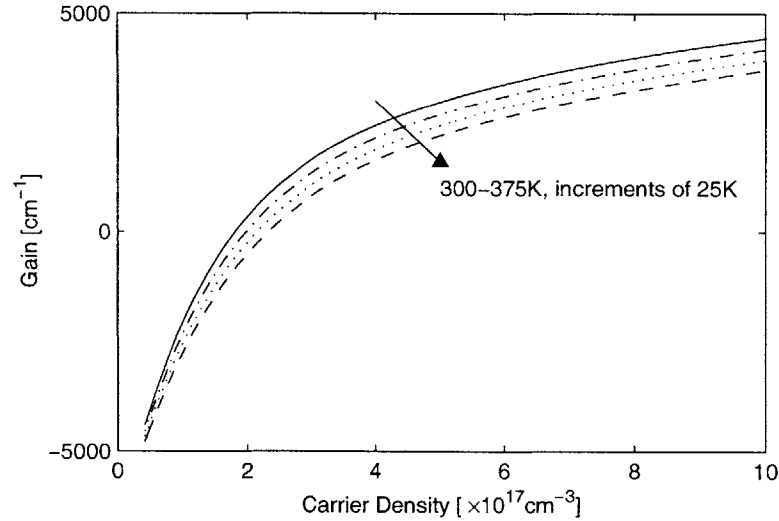


Figure 2-15: Peak gain (g) versus carrier density (N) for different quantum well temperatures, E.P.I. growth

Once a relationship between I (or J) and N is determined, a 3rd-degree polynomial fit can be used to determine the values of A , B , & C in Equation 2.3. Figure 2-16 shows data for two different lasers of the same material. Note on the first data set (F00-Bin9) the characteristic clamping of the threshold carrier density above 2200 mA/cm^2 . It also shows various attempts to fit the data to different values of recombination coefficients. The value of A is neglected, since this is an unimportant factor for high carrier densities. The value for the recombination coefficient, B , was assumed to lie at approximately $B = 10^{-10}$. Various values of the Auger coefficient and perturbations on B resulted in relatively poor data fitting. As shown, the experimental data seem to fit a curve below threshold that has a positive second derivative (bows upward) and therefore do not fit well to the theory. Even with scanning through different values of A and B , there is no reconciliation with the second derivative curving upward.

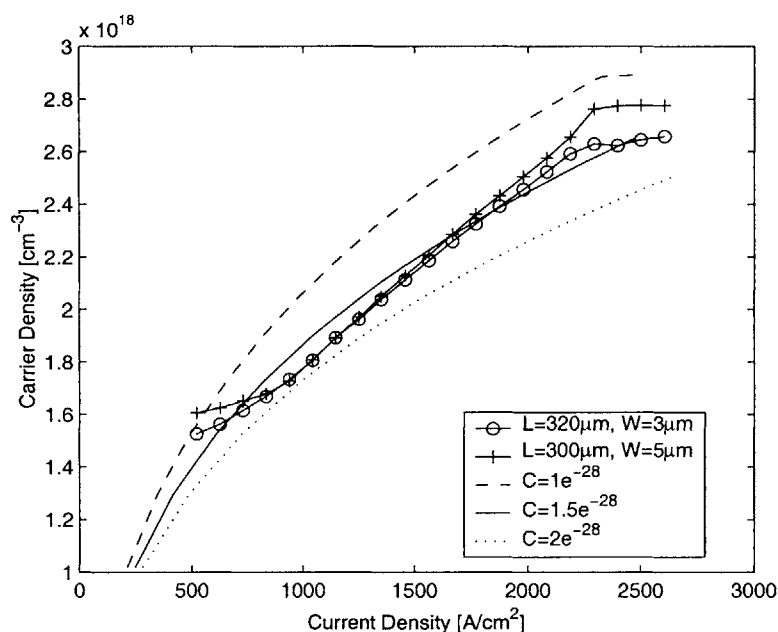


Figure 2-16: Current Density (J) versus carrier density (N) theory and data, E.P.I. growth. $A = 1.1 \times 10^8$, $B = 1 \times 10^{-10}$, $T = 293.2K$

Carrier Lifetime Determination through Spontaneous Emission

Another method developed by C.Y.J. Chu and H. Ghafouri-Shiraz looks at the spontaneous emission power versus bias at low sub-threshold currents [10]. This method takes advantage of the fact that at low carrier densities the Auger recombination term is very weak and Equation 2.53 becomes:

$$\frac{\eta_i I}{qV} = \frac{N}{\tau_c} = AN + BN^2 \quad (2.54)$$

Also, the coefficients take on their low-carrier density definitions described in Section 2.2. Also using Equation 2.9, a parameter fit can be made to this data to obtain values for A and B . A value for C can also be found but the accuracy of this value for small carrier densities is not reliable. Figure 2-17 shows a fit to the L-I curve at low biases. The theoretical curve is shown for comparison and was derived from spontaneous emission calculations, and a curve fit produces: $A = 1.1 \times 10^8 s^{-1}$ and $B = 9.4 \times 10^{-11} cm^3 s^{-1}$. The unknown collection efficiency, η_c of the diode is not easily determinable. Therefore, a range of values for η_c is taken and curve fits for the recombination parameters is performed. The expected value of B (which should be around $10^{-10} cm^3 s^{-1}$ for InGaAsP) is well-known and does not vary greatly from composition to composition. A value of η_c is chosen such that the fitted B parameter matches the expected value. The values for A and C are determined from this. Figure 2-18 shows the various recombination parameters as a function of η_c . The values derived from assuming $B = 1.0 \times 10^{10} cm^3 s^{-1}$ are: $A = 1.0 \times 10^9 s^{-1}$, $C = 2.5 \times 10^{-27} cm^6 s^{-1}$. Quoted values for C from [11] for bulk $1.55 \mu m$ InGaAsP is $C \approx 7 - 9 \times 10^{-29} cm^6 s^{-1}$. The experimentally-derived value is much higher than the expected value and it is unsure as to the source of error.

2.5 Summary

The modelocked laser is $1.55 \mu m$ semiconductor multi-quantum well design with a polyimide confined ridge waveguide. The various laser parameters were determined through a combi-

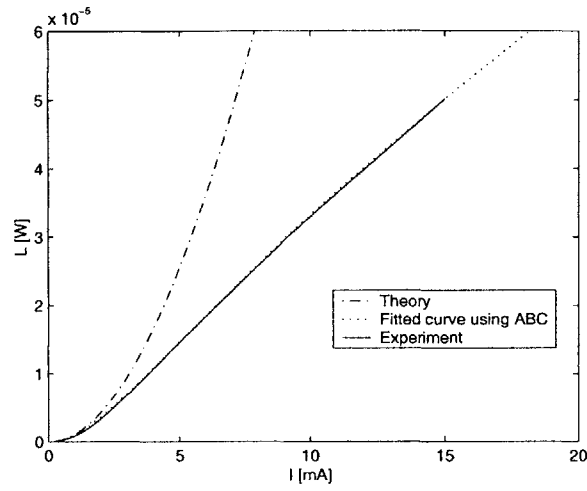


Figure 2-17: L-I curve for biases well below threshold along with fitted parameters

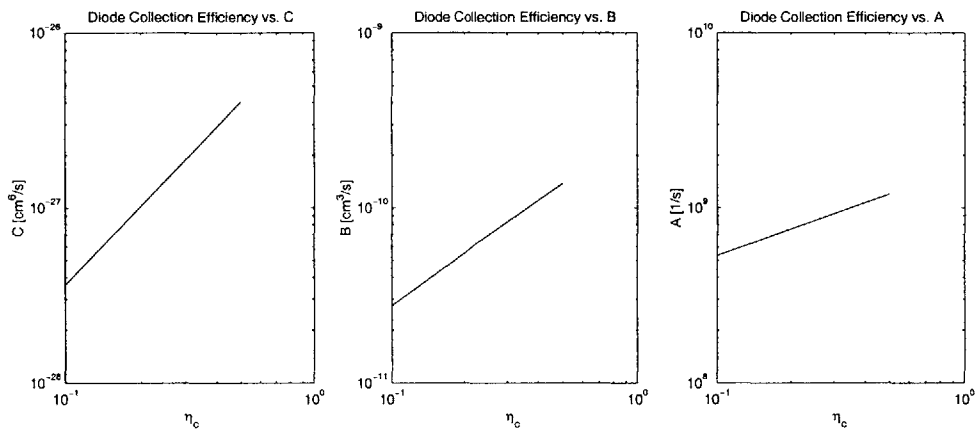


Figure 2-18: A , B , and C parameters as a function of η_c , as fitted to L-I curve

nation of theory and experiment. Despite the redundancy of parameters that the techniques can be used for, each can be used as a check for an alternative method.

On the theoretical end, a suite of laser simulations written by Farhan Rana can be used to determine gain spectra ($g(\lambda)$), mode profiles, confinement factor (Γ), group index (n_g), carrier-dependent gain ($g(N)$), and power versus current bias ($P(I)$).

Experimentally, by performing DC L-I characterization of different-length bars, we can determine values of temperature- and length-independent internal loss (α_i) and internal quantum efficiency (η_i). Extensive use of sub-threshold optical spectrum techniques were used to determine group index (n_g) and gain spectrum ($\alpha(\lambda), g(\lambda), \alpha_i$).

Additionally, using a combination of theory and experiment allows us to predict carrier recombination coefficients (A, B, C) and hence, the carrier lifetime.

Chapter 3

Theory and Split-Step Simulations

In order to design higher performance modelocked diode lasers, it is necessary to gain a better understanding of how they function and the parameters that govern their operation. Work is done to improve various figures of merit, such as reducing pulse width, timing jitter, increasing pulse energy, to name a few. A thorough theoretical model must be developed in order to allow the designer to explore the different possibilities of laser design. This chapter introduces a theoretical formalism developed by Agrawal et al. [2] for traveling wave rate equations. The various pulse shaping mechanisms will be explained. Using this formalism, we introduce a modelocked laser simulation originally developed by Helkey [27] and Derickson [16] based on a partial space integration of the rate equations and a split-step method of pulse propagation. The testing of the simulation will be explained. Results from the simulation will be shown and a discussion on its limitations will follow. We will find that the split-step method is informative and intuitive but its approximations limit its usefulness as a modelocked laser design tool.

3.1 Laser Parameters

This section uses direct results from Chapter 2. Unless otherwise noted, the parameters used in the results from this section are listed in Table 3.1. All illustrative figures ex-

Table 3.1: Laser Parameters

Parameter	Symbol	Value	Unit
Carrier wavelength	λ_0	1.55	μm
Effective group index	n_g	3.7	
Facet reflectivity	$R_{1,2}$	0.274	
Confinement factor	Γ	0.0482	
Gain coefficient	g_0	1864	cm^{-1}
Transparency	N_{tr}	1.82×10^{18}	cm^{-3}
	N_s	unused	cm^{-3}
Differential gain, (Gain sect.)	a_{gain}	1.02×10^{-15}	cm^2
Differential gain, (Sat absorber)	a_{sa}	5.12×10^{-15}	cm^2
Internal quantum efficiency	η_i	0.77	
Internal loss	α_i	11.2	cm^{-1}
Trap recombination coefficient	A	0	s^{-1}
Bimolecular recombination coefficient	B	1×10^{-10}	$cm^3 s^{-1}$
Auger recombination coefficient	C	1×10^{-28}	$cm^6 s^{-1}$
Saturable absorber lifetime	τ_{SA}	unused	s
Linewidth enhancement factor (Gain sect.)	α_G	2	
Linewidth enhancement factor (Sat. Abs.)	α_{SA}	2	
Gain bandwidth factor	t_2	5×10^{-13}	s
Dispersion	β_2	$g_p t_2^2$	$cm^2 s^{-1}$
Active region thickness	d	42	nm
Ridge width	W	1.5	μm
Length of active section	L_{act}	100	μm
Length of saturable absorber	L_{sa}	80	μm
Length of gain region	L_{gain}	3500	μm

cept Figures 3-6, 3-7, 3-10, and 3-14 were created using the split-step method discussed in Section 3.4.1 using one laser segment, unless otherwise noted.

3.2 Traveling Wave Rate Equations

A simple formalism for the photon and carrier density rates has been developed by Bowers et al. [5] that follow from the equations discussed in Section 2.2. These equations simply

take the photon density and introduce a spatial derivative to account for wave propagation.

$$\begin{aligned}\frac{\partial S^+(z, t)}{\partial t} + v_g \frac{\partial S^+(z, t)}{\partial z} &= v_g(\Gamma g_p - \alpha_i)S^+(z, t) + \Gamma\beta_{sp}R_{sp} \\ \frac{\partial S^-(z, t)}{\partial t} - v_g \frac{\partial S^-(z, t)}{\partial z} &= v_g(\Gamma g_p - \alpha_i)S^-(z, t) + \Gamma\beta_{sp}R_{sp}\end{aligned}\quad (3.1)$$

$$\frac{\partial N(z, t)}{\partial t} = \frac{\eta_i I}{qV} - \frac{N}{\tau_c} - v_g g_p (S^+(z, t) + S^-(z, t)) \quad (3.2)$$

where the group velocity, v_g , is given in Equation 2.11 and the peak gain, g_p , and carrier lifetime, τ_c are carrier density dependent. τ_c follows Equation 2.3 while the peak gain follows

$$g_p(N) = g_0 \ln \left(\frac{N + N_s}{N_{tr} + N_s} \right) \quad (3.3)$$

g_0 , N_s and N_{tr} are fitting parameters for the g_p vs. N dependency [11]. The peak gain is defined more thoroughly in Section 3.3.2. N_{tr} , the transparency carrier density, has a physical meaning when $N = N_{tr}$. In this case the gain, g , equals zero and the gain is transparent to the propagating wave. All variables are as described in 2.2 except now S^+ and S^- represent the forward- and reverse-propagating photon densities [cm^{-3}].

Two traveling photon density equations are needed to account for densities traveling in the $+/-z$ directions. These equations account for many pulse shaping effects that will be introduced in this chapter, but fail to take in account any effects on the phase of the electromagnetic photon field such as self-phase modulation or dispersion. The mirror loss, α_m , is left out of these equations, and is left as boundary conditions when a solution to these equations is needed.

The formalism developed by Agrawal and Olsson [2] deals with propagating electric

fields and therefore, can include phase effects:

$$\frac{1}{v_g} \frac{\partial E^\pm(z, t)}{\partial t} \pm \frac{\partial E^\pm(z, t)}{\partial z} = \frac{\Gamma g_p}{2} (1 - j\alpha) E^\pm(z, t) - \frac{\alpha_i}{2} E^\pm(z, t) + \frac{1}{2} (\Gamma g_p t_2^2 - j\beta_2) \frac{\partial^2}{\partial t^2} E^\pm(z, t) \quad (3.4)$$

$$\frac{\partial N(z, t)}{\partial t} = \frac{\eta_i I}{qV} - \frac{N}{\tau_c} - \frac{\Gamma g_p}{h\nu\mu v_g} |E^+(z, t) + E^-(z, t)|^2 \quad (3.5)$$

where E^\pm are the forward- and reverse-propagating electric fields [V/cm], α is the linewidth enhancement factor (typically 2-5 in semiconductor lasers), t_2 is the gain bandwidth parameter [s], β_2 is the dispersion parameter [s^2/cm], $h\nu$ is the energy quantum per photon [J], and μ is the magnetic permittivity [$\Omega s/cm$]. Spontaneous emission rates are neglected in these equations. This is a good approximation since the pulse power is much greater than the spontaneous emission term. The real terms correspond to gain and attenuation rates of the propagating pulse and the imaginary terms correspond to phase changes. The factor of 1/2 accounts for the fact that the photon density and hence the wave power is proportional to the square of the electric field. We can normalize the electric field, E^\pm , into A^\pm so that $|A^\pm(z, t)|^2 = P(z, t)$, where $P(z, t)$ is the power at a given point in the pulse. Rewriting the equations gives us [2]:

$$\frac{1}{v_g} \frac{\partial A^\pm(z, t)}{\partial t} \pm \frac{\partial A^\pm(z, t)}{\partial z} = \frac{\Gamma g_p}{2} (1 - j\alpha) A^\pm(z, t) - \frac{\alpha_i}{2} A^\pm(z, t) + \frac{1}{2} (\Gamma g_p t_2^2 - j\beta_2) \frac{\partial^2}{\partial t^2} A^\pm(z, t) \quad (3.6)$$

$$\frac{\partial N(z, t)}{\partial t} = \frac{\eta_i I}{qV} - \frac{N}{\tau_c} - \frac{\Gamma g_p}{h\nu W d} |A^+(z, t) + A^-(z, t)|^2 \quad (3.7)$$

using the fact that

$$S^+(z, t) + S^-(z, t) \approx \frac{\Gamma}{h\nu v_g W d} |A^+(z, t) + A^-(z, t)|^2 \quad (3.8)$$

where W is the laser width [cm] and d is the quantum well thickness [cm]. The equation is approximate because the photon density cannot account for wave interference effects as can the right-hand side. Each term in the field rate equations shapes the pulse: either by gain/attenuation or phase changes. The next section discusses these pulse-shaping mechanisms.

3.3 Pulse-Shaping Mechanisms

The pulse-shaping mechanisms in Equation 3.6 can be explained individually by analyzing the dependence of each rate. The first term, $\Gamma g_p \frac{1}{2} A^\pm(z, t)$, is the gain/loss saturation term; the second, $-\gamma \alpha \Gamma g_p \frac{1}{2} A^\pm(z, t)$, is the self-phase modulation term; the third, $-\alpha_i \frac{1}{2} A^\pm(z, t)$, is the internal loss; the fourth, $t_2^2 \Gamma g_p \frac{1}{2} \frac{\partial^2}{\partial t^2} A^\pm(z, t)$, is the gain bandwidth term; the fifth, $-\gamma \beta_2 \frac{1}{2} \frac{\partial^2}{\partial t^2} A^\pm(z, t)$, is dispersion. These terms can be categorized into non-linear and linear effects, and are described in the following sections.

3.3.1 Non-linear Effects

Since the gain term is also carrier density dependent and the change in the carrier density is coupled to the traveling field equations, each term that includes gain is non-linear. The most important pulse shaping mechanism is gain and loss saturation.

Gain/Loss Saturation

The gain/loss saturation term deals with gain due to stimulated emission of carriers where g_p follows Equation 3.3. In a quantum well without significant photon density, the last term in Equation 3.7 is negligible and in steady state the first two rate terms on the right hand

side balance each other.

$$\frac{\eta_i I}{qV} = \frac{N_{SS}}{\tau_c} \quad (3.9)$$

where N_{SS} is the steady-state carrier density without significant photon density. In a gain medium, the steady-state gain, g_{SS} , is positive. When a pulse travels through this medium, the pulse is amplified through stimulated emission, which causes the carrier density to drop through this previously neglected last term in Equation 3.7. As the carrier density drops, the gain also decreases, meaning less stimulated emission. As the pulse travels through the gain region, more and more carriers recombine through stimulated emission and the gain continues to drop. The result of this is a greater amplification in the front edge of the pulse (when the gain is highest) and the least amount in the trailing edge. If the pulse energy is sufficiently high, the gain will approach zero as the carrier density reaches transparency ($N \approx N_{tr}$) and the trailing edge will pass through unaffected by the gain.

In a saturable absorber, the carriers are swept out of the quantum wells by reverse biasing the diode. The carrier sweep out time can be described by a lifetime that is different from a forward-biased laser diode. Karin et al. develop a model that describes the relationship between the carrier lifetime and the reverse bias voltage [34, 60]. Instead of injecting carriers to improve the stimulated emission rate, the carrier density is reduced well below transparency level so that photons will be absorbed at a higher rate. Hence, the steady-state gain becomes negative. As a laser pulse passes through the saturable absorber, the photons are absorbed by the valence electrons, creating free carriers. As the pulse is absorbed, the absorption magnitude is reduced, approaching zero. As a result, the leading edge is attenuated more than the trailing edge.

Figure 3-1 shows examples of gain and absorption saturation. Note the broadening of the full width at half maximum (FWHM) pulse width in (a) and the narrowing of the FWHM pulse width in (b). Note also that the pulse center-of-mass drifts earlier in time in (a) and lags behind in (b). Typically, in a two-section passively modelocked laser (Figure 1-8), the gain section broadens the pulse while the absorber section narrows the pulse. The

gain section also has the effect of "pushing" the pulse ahead of its group velocity while the absorber section "drags" the pulse slower than its group velocity. It is not intuitive that the gain and absorber saturation effect balance such that a modelocked pulse reaches a steady-state in which these non-linear effects exactly cancel each other in a single round-trip. In terms of pulse shaping, if the net round-trip effect is narrowing, there needs to be other pulse broadening mechanisms to prevent the pulse from narrowing to a delta function. If the net effect is pulse broadening, then the pulse will eventually vanish and the conditions for modelocking are not met. The dominant pulse broadening effect that allows for a finite FWHM pulse is gain bandwidth (see Section 3.3.2). In terms of pulse "walking", the net effect is a speeding up or slowing down of the group velocity. This is an interesting result of gain/loss saturation that changes the true round trip frequency of the laser.

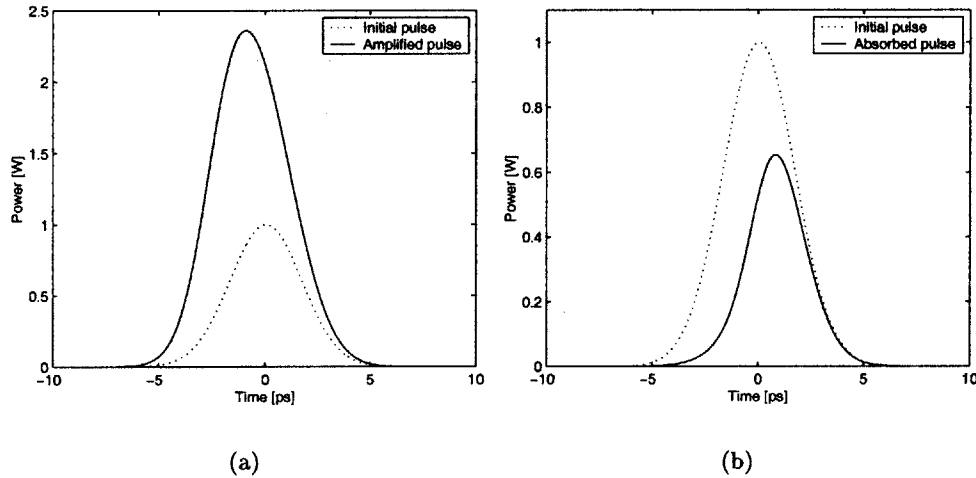


Figure 3-1: Examples of (a) gain and (b) absorption saturation effects. $L_{gain} = L_{sa} = 50\mu\text{m}$, $I_{gain} = 4\text{mA}$, $g_{sa} = -9539\text{cm}^{-1}$

Figure 3-2 shows the pulse center-of-mass drifting earlier in time as it propagates through a gain medium. Note the pulse energy growing as well as the drift effect. Note also that for small pulse energies (darker pulse lines) the gain sees little saturation effect (the entire pulse is amplified uniformly resulting in no FWHM broadening). For large energies (lighter pulse

lines), only the front part of the pulse sees amplification while the trailing edge follows the original pulse envelope. The opposite effect occurs for absorption regions; the pulse tends to lag in time due to the front end of the pulse becoming attenuated.

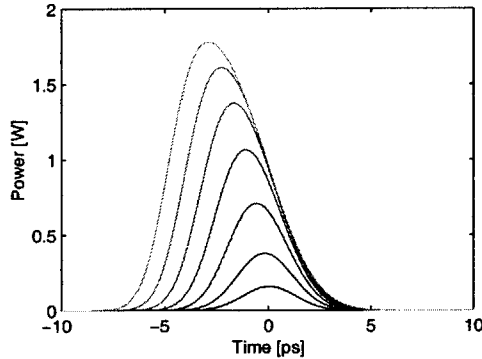


Figure 3-2: Example of pulse drifting due to gain saturation; pulse evolves with lighter pulse color. Each pulse represents one round-trip propagation from the previous. $t = 0$ follows the propagation at the pulse's group velocity. $\alpha = 0$, $L_{gain} = 50\mu m$, $I_{gain} = 3mA$

In a passively modelocked laser, the dominant pulse shaping mechanisms are gain and absorption saturation. In order to see the conditions necessary to produce modelocking, it is necessary to show the evolution of a pulse through a two-section passively modelocked laser. Figure 3-3(a) shows the evolution of a pulse through the different mediums. The top picture shows the original pulse; each subsequent picture shows the evolution of the pulse through the different regions: the gain region, absorption region, and a mirror reflection, respectively. In the second to fourth plots the left axis and solid line correspond to the pulse power profile, the right axis and dotted line correspond to the shaping potential, which is essentially the ratio of the shaped pulse power profile to the input pulse power profile. Each shaping potential is multiplied with the pulse directly above to create the respective pulses.

The second picture shows gain saturation through a gain medium. Note the increase in pulse energy. The shaping potential starts out at early times (from $-10ps$) at the unsaturated gain value (where $N = N_{SS}$). As the pulse propagates through the gain medium, the gain is reduced and approaches zero (transparency), as shown as a decreasing

shaping potential with increasing time. The output trailing edge follows the original trailing edge shape.

The third picture shows absorption saturation through an absorber region. Note the front end of the pulse is attenuated. The shaping potential begins at its unsaturated absorption value (a fraction) and then saturates towards transparency, similarly to the gain region's shaping potential. Note also that the peak pulse power remains the same, unlike in the gain region. This occurs because the number of carriers it takes to reach transparency in the absorber region is smaller than in the gain region. This corresponds to a smaller pulse energy requirement to saturate the section (i.e. bring the gain to zero). This figure demonstrates the lower saturation energy (E_{sat}) for the absorber region. This is a crucial effect in modelocked lasers.

The fourth picture shows mirror reflectivity. The value of the power reflectivity is 0.2744, calculated from a group index of $n_g = 3.2$ to air. Note the uniform shaping potential and the drop in pulse energy.

Figure 3-3(b) shows the pulse power profiles at each stage, on the same axis and scale, for comparison purposes. The pulse evolves with increasingly lighter pulse line colors (from black to light gray). The pulse energy increases significantly through the gain region but decreases marginally through the absorber region, demonstrating the higher saturation energy of the gain region. The saturation energy's importance is demonstrated in Figure 3-3(c).

Figure 3-3(c) shows the total shaping potential of the pulse through the three regions. The three shaping potentials were multiplied together to create the overall shaping potential. At early times, the potential is just the multiplication of the three unsaturated gains. Since the absorber saturates faster (due to a lower E_{sat}), the total potential begins to see more gain than loss and the potential rises during the early part of the pulse. As the gain region slowly saturates, the overall potential is reduced. This produces a bell-shaped potential. It is necessary that the shaping potential has a gain lower than one at both tails and rises above one in the center. This shape attenuates the tails of the pulse and allows the peak to grow, thus narrowing the pulse and simultaneously allowing the pulse to maintain a

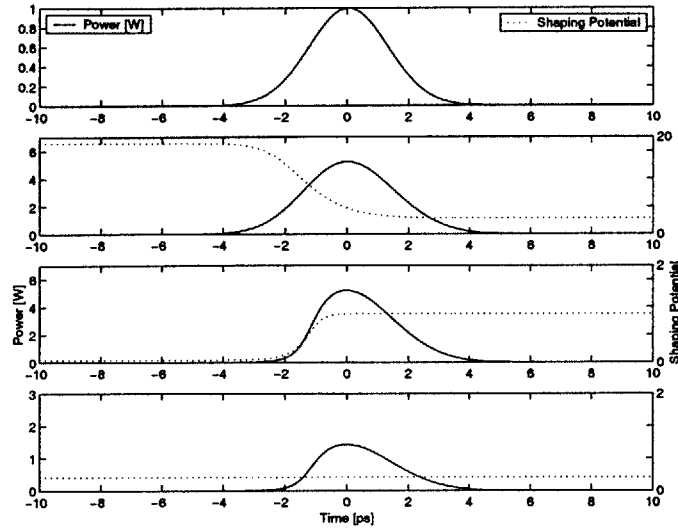
constant energy. Without another force to balance this pulse-narrowing effect, the pulse would narrow without bound. A separate pulse-broadening effect is necessary to reach a steady-state. The dominant pulse-broadening effect is through finite gain bandwidth and secondarily through dispersion coupled with self-phase modulation. (See Section 3.3.2). If the gain were above one at the tails, it would not be possible to reach a steady-state pulse. The gain would cause the tails of the pulse to grow regardless of shape, thus broadening the pulse continuously. This corresponds to a continuous wave (CW) lasing case. Hence, there is a regime of operation in a modelocked laser that corresponds to modelocking and also CW operation.

Self-Phase Modulation

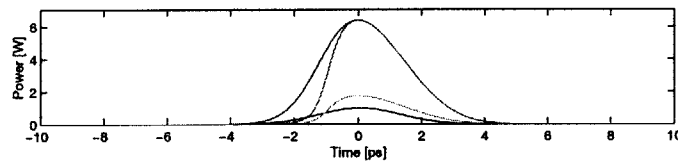
The self-phase modulation term differs from the gain saturation term only by a factor of $-j\alpha$. The imaginary term describes the effect that the change in gain has on the instantaneous index of the material. As the index changes, the instantaneous frequency deviates from the actual carrier frequency. The linewidth enhancement factor, α , is defined as

$$\alpha = 2k_0 \frac{\frac{d\bar{n}}{dN}}{\frac{dg}{dN}} \quad (3.10)$$

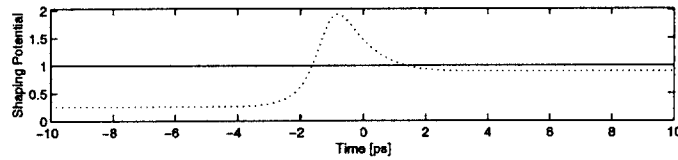
where k_0 is the wave number of the carrier frequency in free space and \bar{n} is the effective index. The phase velocity is inversely proportional to the index. As a pulse passes through a gain section in the laser, the carrier density (and hence the gain) goes down as carriers are utilized in stimulated emission. By the Equation 3.10 and 3.6, this means that the index goes up as the gain goes down. As the index increases while the pulse passes through the gain region, the phase velocity decreases. This causes the phase of the pulse to "lag" from the leading edge phase, essentially causing the sinusoidal electromagnetic waves to "stretch out", producing a momentarily negative instantaneous frequency. As the gain saturates, the gain and index become constant again, and the phase becomes constant. This causes the instantaneous frequency to revert back to zero. The exact opposite effect happens in an



(a)



(b)



(c)

Figure 3-3: (a) Pulse evolution with shaping potentials. Each evolved pulse is shown with the shaping potential used to create it from the previous pulse (directly above). Top picture is the original pulse. The following pictures show evolution due to gain saturation, absorption saturation, and mirror reflection, respectively. (b) Pulses on an absolute scale (pulse evolves with lighter pulse color). (c) Total shaping potential, including unity line. $L_{gain} = L_{sa} = 50\mu m$, $I_{gain} = 6mA$, $g_{sa} = -1.244 \times 10^4 cm^{-1}$, $\alpha = 0$

absorber region, where the gain increases as the pulse passes through the laser region. This causes the index to decrease, thus causing a "bunching up" of the electromagnetic waves and an increase to the instantaneous frequency. Figure 3-4 shows chirping effects in both gain and absorption regions. By itself, self-phase modulation is not responsible for any pulse shaping since it only affects the phase of the pulse. However, coupled with other effects such as dispersion, where different frequencies propagate at different velocities, self-phase modulation can produce significant pulse shaping. If the linewidth enhancement factor is large enough, the change in the phase from the leading edge to the trailing edge becomes larger and the pulse's spectrum spreads from its ideal transform-limited state. This spread in the spectrum could be great enough to allow dispersive effects to greatly affect the pulse shape. In an extreme case, multiple pulses can form as the cavity dispersion spreads the pulse energy in time.

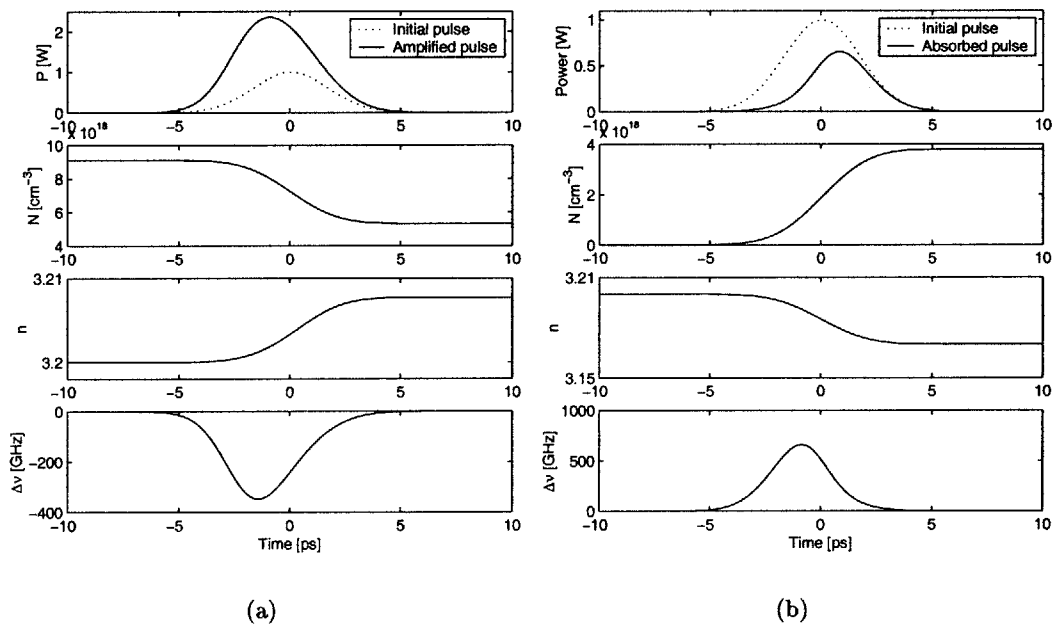


Figure 3-4: Self-phase modulation effects due to linewidth enhancement factor. $\alpha = 2$. Graphs shown are Power (P), Carrier density (N), index (n), instantaneous frequency (f). $L_{gain} = L_{sa} = 50\mu\text{m}$, $I_{gain} = 4\text{mA}$, $g_{sa} = -9539\text{cm}^{-1}$

Active Gain Modulation

Active gain modulation can essentially be accounted for by varying the injection current, I , in time. Typically, this current is modulated sinusoidally, however sharper peaked functions have been generated using other methods, such as step recovery diodes [46] or nonlinear transmission lines [51]. As the injection current is modulated, it is expected that the carrier density and hence, the gain of the active section is also modulated. If the repetition rate of the modulation is slow, then the current can be treated as quasi-static and a linear proportionality can be found between the current and carrier density. However, for fast modulation (well above 1 GHz), this is not the case, since the injection modulation is dampened by the other recombination rates within the carrier rate equation (Equation 3.7).

If the gain is modulated at the round-trip frequency of a traveling pulse within the resonant cavity, then one can see that the pulse will tend to arrive in the active modulation section at the peak of the time-dependent gain function. If the pulse arrives ahead of the peak, the gain function at that point will be increasing in time, and more pulse amplification will be given to the trailing edge, thus pulling the pulse backward in time. If the pulse arrives in the active section behind the gain peak, the gain will be decreasing in time and preference will be given to the growth of the pulse's leading edge, thus pulling the pulse forward in time. Essentially, the time-dependent gain function serves to corral the pulse into the gain peak.

It was mentioned that a DC gain region in a modelocked laser can increase the group velocity of the pulse by pushing it forward in time, hence it will arrive in the active section always ahead of the gain peak. The AC modulation in an active section will attempt to pull the early pulse backward; the pulling force getting increasingly stronger the earlier the pulse. Eventually, a balance of the two forces is reached and the pulse will appear in the active region slightly ahead of the gain peak but always propagates at the modulation frequency of the radio frequency (RF) current modulation. This can be seen in Figure 3-5. Each pulse profile represents a pulse zero-centered at the modulation period. In the passive case, the pulse does not arrive exactly at the modulation period, rather it drifts linearly. In

the active case, the pulse initially drifts from the center of the gain peak (always centered at $t = 0$) until it settles slightly ahead of the gain peak (negative time). This phenomenon, known as dynamic detuning [47], can serve as a supplementary pulse shaping force since the pulse is effectively "pushed" against the wall of the gain function.

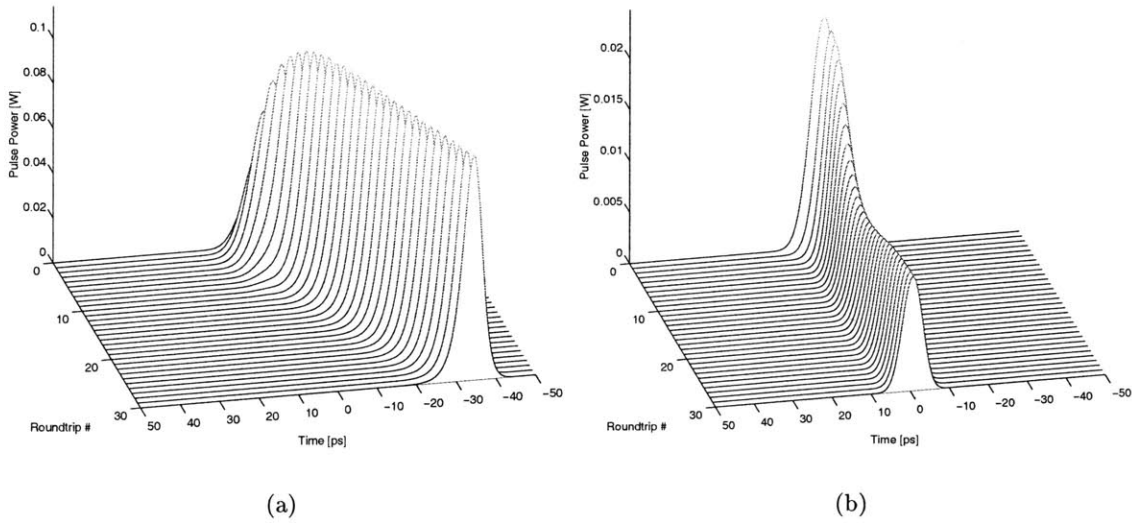


Figure 3-5: Examples of (a) pulse drifting due to dominant gain saturation in a 2-section passively modelocked laser and (b) pulse drift cancelling in a 2-section active modelocked laser. $L_{sa} = L_{act} = 80\mu m$, $L_{gain} = 3500\mu m$, $\omega_M = \frac{v_g}{2(L_{act} + L_{gain})}$, $I_{gain} = 63mA$, $g_{sa} = -1864cm^{-1}$, $I_{RF} = 5mA$, $g_{act} = -9159cm^{-1}$

3.3.2 Linear Effects

Gain Bandwidth

Gain is dependent on carrier density, temperature, and wavelength. Figure 3-6 shows typical gain curves for the UCSB laser at 300K and several carrier densities. The data was generated by a theoretical gain spectrum calculator written by Farhan Rana. Since the energy within a modelocked laser is typically small, a core temperature near room temperature is suitable. The unsaturated carrier density is determined by the current bias and

recombination times of the laser. It is expected that the fundamental lasing frequency lies at the peak of this gain curve. The frequency pulse-train of a modelocked laser should have an envelope that spans only a small fraction of the gain curve, near the peak. Therefore, in order to provide a simple model to allow for gain bandwidth effects, a second-order fit to the gain curve at the peak can be made. The equation to be fit is:

$$g(\omega) = g_p(N) [1 - t_2^2(\omega - \omega_0)^2] \quad (3.11)$$

where $g(\omega)$ is the frequency-dependent gain [cm^{-1}], g_p is the peak unsaturated gain of the laser [cm^{-1}] defined in Equation 3.3, t_2 is the optical bandwidth parameter [s], and ω_0 is the gain peak's center frequency. Figure 3-7 shows how the fit is performed. The spectrum of a pulse envelope, $\tilde{A}(\omega)$ will be filtered by the gain curve as:

$$\tilde{A}_{out}(\omega) = \tilde{A}_{in}(\omega) e^{-\frac{1}{2}\Gamma\omega^2 t_2^2 g_p L} \quad (3.12)$$

where $\tilde{A}_{in}(\omega)$ is the Fourier transform of the input pulse envelope [W], $\tilde{A}_{out}(\omega)$ is the Fourier transform of the output pulse envelope [W], and L is the length of the propagation through the material [cm].

An analytic $1ps$ Gaussian pulse has a standard deviation width in frequency of $1/1ps = 1THz$. It can be seen that this pulse only has a spectrum that spans a small portion of the gain curve. As the pulse gets narrower through gain/absorption saturation, the spectrum becomes broader. The gain bandwidth has the effect of "shedding" the side frequencies of a pulse train and is illustrated in Figure 3-8. The gain bandwidth narrows the spectrum, thus broadening the pulse, and is the primary balancing force that allows a pulse to reach a steady state.

Dispersion

Material dispersion accounts for the relative difference in phase velocities of different frequencies. A linear dependence of phase on the frequency results in a time delay but a

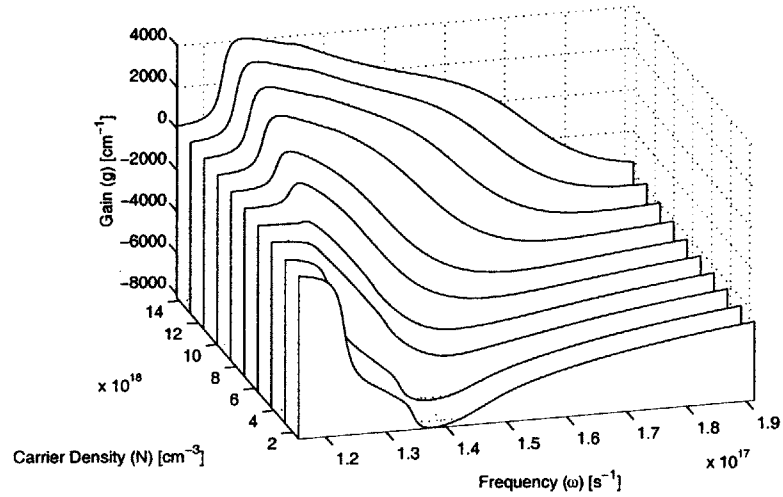


Figure 3-6: Gain vs. wavelength at 300K and several carrier densities

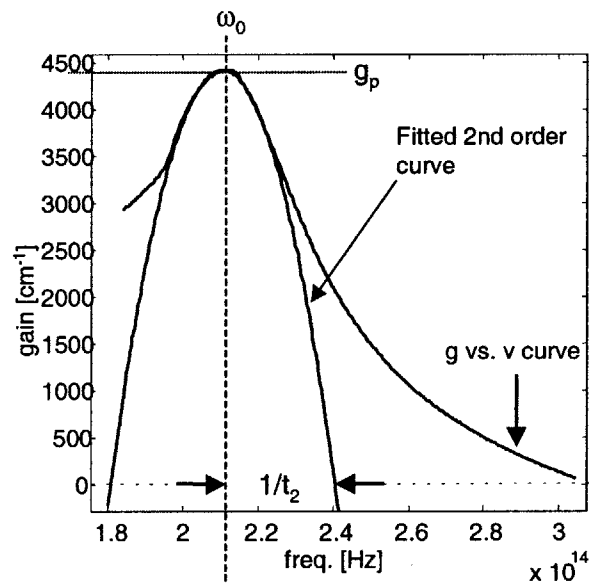


Figure 3-7: Determination of g_p , ω_0 and t_2 . The fit is second-order.

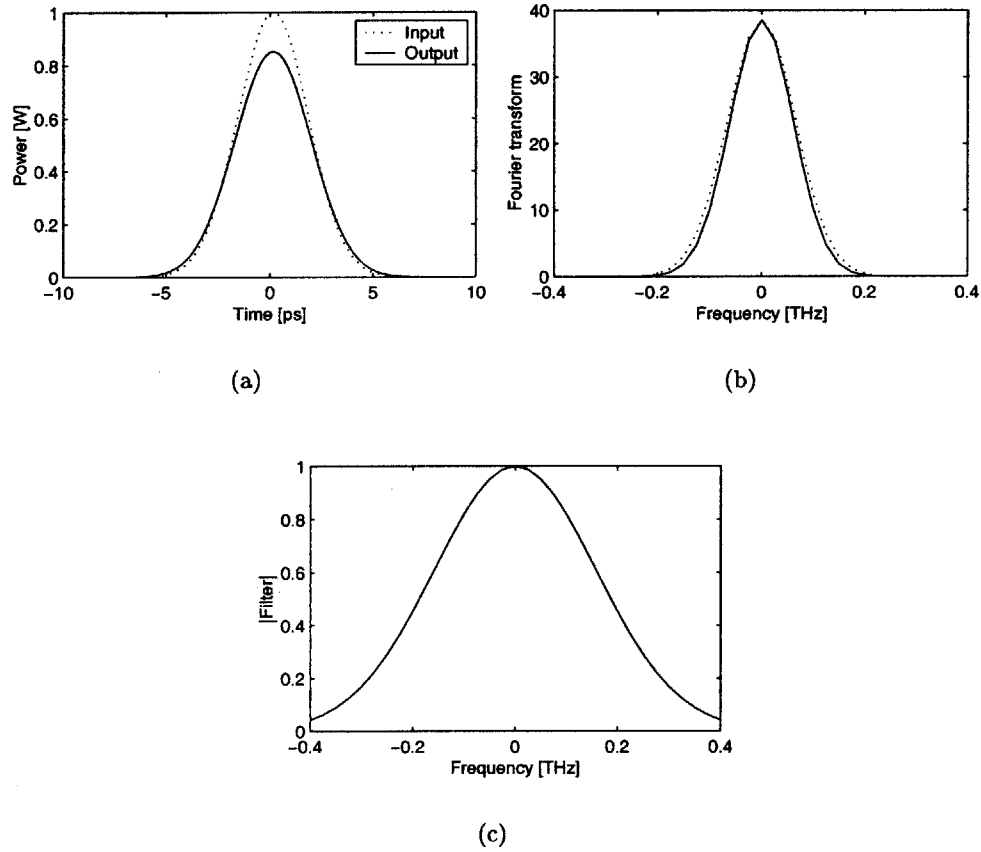


Figure 3-8: Example of pulse broadening due to finite gain bandwidth. (a) shows the input pulse and the broadened pulse. (b) shows the input and broadened spectrum. (c) shows the magnitude of the filter. $t_2 = 1 \times 10^{-13} s$, $g_p = 2 \times 10^4 cm^{-1}$, $L = 50 \mu m$ The gain was increased for illustrative purposes.

second-order frequency dependence results in relative velocity differences between frequencies. The material dispersion parameter, β_2 , measures the strength of this dependence. Figure 3-9 illustrates the effect of dispersion on an unchirped Gaussian pulse. A typical approximate of the dispersion parameter is

$$\beta_2 = \Gamma g_p t_2^2 \quad (3.13)$$

Similarly to the filtering performed by the gain bandwidth parameter:

$$A_{out}(\omega) = A_{in}(\omega) e^{-j\frac{1}{2}\omega^2\beta_2 L} \quad (3.14)$$

where the imaginary number implies a phase-filtering effect.

3.4 Simulations

There are many methods that have been developed to simulate modelocking. The most straight-forward method is to solve Equations 3.6 and 3.7 using finite difference methods [5, 67]. These methods discretize the time and space derivatives and solve them using differential approximations. Typically, the relationship between dt and dz is known through the group velocity:

$$v_g = \frac{dz}{dt} \quad (3.15)$$

Therefore, it is possible just to solve a finite difference problem using the total time derivative

$$\frac{dS^\pm}{dt} = \frac{\partial S^\pm}{\partial t} + v_g \frac{\partial S^\pm}{\partial z} \approx \frac{S^\pm(t + \Delta t, z + \Delta z) - S^\pm(t, z)}{\Delta t} \quad (3.16)$$

We obtain the space dependence through the group velocity. Jones et al. improve on the finite difference method by approximating the finite band width of the gain function using a non-parabolic frequency dependence that results in a first-derivative in space [31]. This

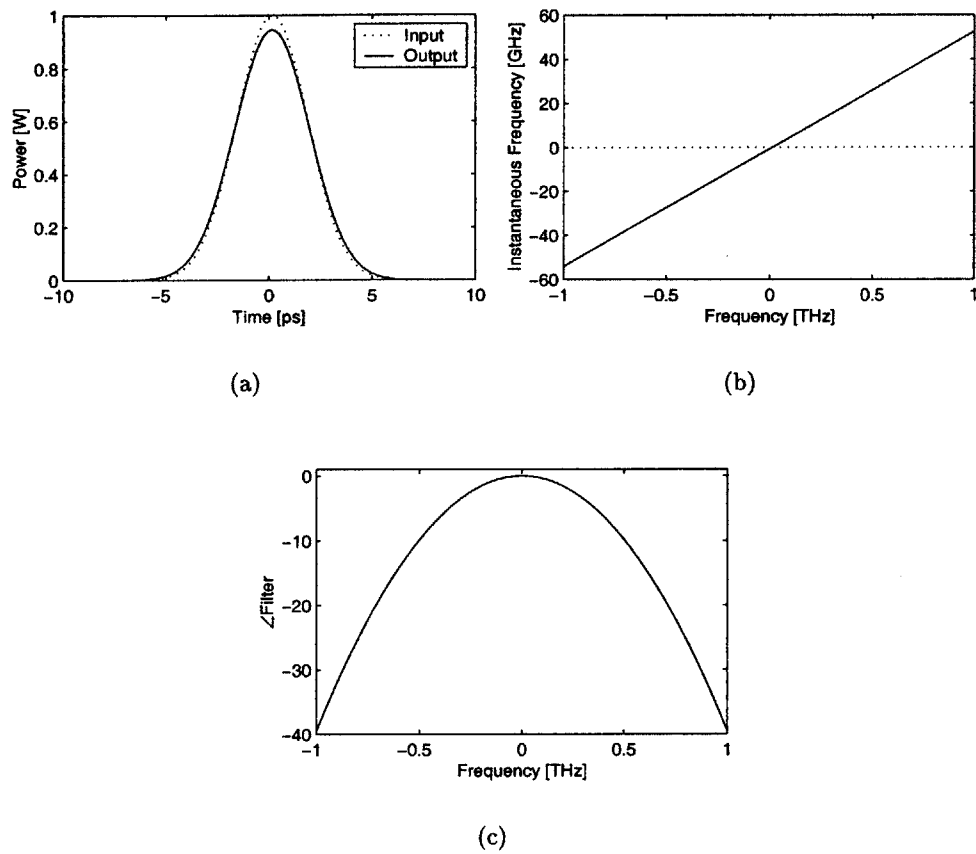


Figure 3-9: Example of pulse broadening due to dispersion. (a) shows the unchirped input pulse and the broadened pulse. (b) shows the instantaneous frequency. (c) shows the phase of the filter. $\beta_2 = 4 \times 10^{-22} \text{ cm}^2/\text{s}$, $L = 50 \mu\text{m}$

method is discussed in Chapter 4.

3.4.1 Split-step method

The method explored in this chapter deals with a computationally efficient method that involves passing a pulse through a partially-integrated space segment followed by a frequency-domain filtering. The partial integration was developed by Helkey et al. [27, 28] for use with the traveling photon density rate shown in Equations 3.1 and 3.2. The additional frequency-domain filtering was initially developed by Agrawal [1]. The implementation presented here follows Derickson and uses traveling field equations developed by Agrawal [2].

The method's approach is to split a laser cavity into discrete sections in space. A pulse in the time domain is passed through each discrete section, allowing the traveling wave rate equations to shape the pulse as it propagates from one edge to the other. In order to perform an efficient propagation of the pulse, the split-step method groups the non-linear and linear terms into two groups, first performing a non-linear shaping followed by a linear-term filtering. An analytic integration of the non-linear terms in the traveling wave equations (Equation 3.6) can be performed using justifiable approximations [2]. The remnant linear terms can be represented as a frequency-domain filter.

The major approximations to Equation 3.6 are listed below:

1. A linear carrier density dependency on the gain:

$$g(N) = a(N - N_{tr}) \quad (3.17)$$

where a is the differential gain [cm^2]. The value of a can be approximated as the slope of the logarithmic g vs. N at a given N . It is necessary to realize that the differential gain is higher for a saturable absorber region than for a gain region, therefore two values of a are necessary to describe the two different regions. This can be seen by comparing the slopes at a carrier density below and above N_{tr} in a typical g vs. N graph (Figure 2-15). This again implies that it is easier to reach transparency for a

saturable absorber region rather than a gain region for a given absolute gain/loss.

2. Small internal loss (α_i). Internal loss is approximated as zero in the derivation of the partial integration. This is valid if $\Gamma g \gg \alpha_i$, which is true when the carrier density is much higher than transparency. For a short, monolithic modelocked laser, this is achieved only with sufficiently high bias currents. The high bias current can replenish the carrier density well above transparency before the circulating pulse returns.
3. The pulse is much shorter than the carrier recombination time. This allows the gain saturation effects to occur while being able to neglect the carriers refreshing to its steady state value while the entire pulse passes through a section of the semiconductor. This is a valid approximation since a typical pulse width is $1 - 10ps$ while the carrier lifetime is on the order of ns . This assumption becomes less reasonable when the carrier lifetime is enhanced within a saturable absorber section. Karin et al. find typical lifetimes within a saturable absorber to be $5 - 50ps$ [34].

Non-linear Effects Step

In order to obtain the analytic partially integrated solutions found in [2], we neglect dispersion and a frequency-dependent gain. Following the forward traveling pulse as it propagates at the group velocity gives us:

$$\frac{dA}{dz} = \frac{1}{v_g} \frac{\partial A}{\partial t} + \frac{\partial A}{\partial z} = \frac{\Gamma g}{2} (1 - j\alpha) A - \frac{\alpha_i}{2} A \quad (3.18)$$

Stating explicitly the relationship between the normalized field, A , and the power, P :

$$A(z, t) = \sqrt{P(z, t)} e^{j\phi(z, t)} \quad (3.19)$$

allowing us to break the preceding equation into a magnitude and phase part:

$$\frac{dP}{dz} = (\Gamma g - \alpha_i)P \approx \Gamma g P \quad (3.20)$$

$$\frac{d\phi}{dz} = -\frac{1}{2}\alpha\Gamma g \quad (3.21)$$

Here we make the assumption that the internal loss is smaller than the gain. For a given length, L , we propagate the pulse, thus integrating these equations from 0 to L . This leads to:

$$P_{out}(\tau) = P_{in}(\tau)e^{h(\tau)} \quad (3.22)$$

$$\phi_{out}(\tau) = \phi_{in}(\tau) - \frac{1}{2}\alpha h(\tau) \quad (3.23)$$

where

$$\tau = t - \frac{z}{v_g} \quad (3.24)$$

so that we can follow the pulse as it propagates at the group velocity and

$$h(\tau) = \Gamma \int_0^L g(z, \tau) dz \quad (3.25)$$

We have defined $P_{out} \equiv P(L)$ and $P_{in} \equiv P(0)$ to represent the end and beginning points of the section of length L .

We now analyze Equation 3.7. Immediately before the pulse passes through the length L section, we can make the assumption that the carrier density has refreshed itself to the steady state value where there is a lack of photon density. Algebraically, this amounts to setting A to zero to solve the steady state carrier density:

$$\frac{\eta_i I}{qV} = \frac{N_{ss}}{\tau_c} \Rightarrow N_{ss} = \frac{\eta_i I}{qV} \tau_c \quad (3.26)$$

where N_{ss} represents the steady state carrier density, similar to Equation 3.9. This repre-

sents the unsaturated carrier density before the pulse propagates through the section. Using Equation 3.17, we obtain the unsaturated gain, g_{ss} :

$$g_{ss} = a(N_{ss} - N_{tr}) \quad (3.27)$$

Using Equations 3.7, 3.17, and 3.27 we obtain

$$\frac{\partial g}{\partial \tau} = \frac{g_{ss} - g}{\tau_c} - g \frac{P}{E_{sat}A} \quad (3.28)$$

where

$$E_{sat} \equiv \frac{h\nu Wd}{a\Gamma} \quad (3.29)$$

The saturation energy, E_{sat} , is a measure of the amount of pulse energy it takes to saturate the gain. We integrate Equation 3.28 from $z = [0, L]$ and multiply by the confinement factor, using Equations 3.25,3.20 to arrive at

$$\frac{\partial h}{\partial \tau} = \frac{\Gamma g_{ss}L - h}{\tau_c} - \frac{P_{in}}{E_{sat}} (e^h - 1) \quad (3.30)$$

The first term on the right-hand side represents the rate at which the integrated gain attempts to return to its steady state, unsaturated value. The second term represents the saturation of the integrated gain due to photons traveling through the section. Solving for Equation 3.30 gives us

$$h(\tau) = -\ln \left(1 - \gamma e^{-\frac{U_{in}(\tau)}{E_{sat}}} \right) \quad (3.31)$$

where

$$U_{in}(\tau) = \int_{-\infty}^{\tau} P_{in}(\tau') d\tau' \quad (3.32)$$

and γ is solved by recognizing the unsaturated integrated gain, $h(-\infty)$:

$$h(-\infty) = \Gamma g_{ss} L = -\ln(1 - \gamma) \quad (3.33)$$

so

$$\gamma = 1 - e^{-\Gamma g_{ss} L} = 1 - \frac{1}{G_0} \quad (3.34)$$

where we have made the definition

$$G_0 \equiv e^{\Gamma g_{ss} L} \quad (3.35)$$

finally, we can write explicitly the closed form relationship between the input and output power and phase of a traveling pulse through a section of length L :

$$P_{out}(\tau) = \frac{P_{in}(\tau)}{1 - \left(1 - \frac{1}{G_0}\right) \exp\left(-\frac{U_{in}(\tau)}{E_{sat}}\right)} \quad (3.36)$$

$$\phi_{out}(\tau) = \phi_{in}(\tau) + \frac{\alpha}{2} \ln \left[1 - \left(1 - \frac{1}{G_0}\right) \exp\left(-\frac{U_{in}(\tau)}{E_{sat}}\right) \right] \quad (3.37)$$

These two equations allow us to relate the output and input pulses via the effects of gain/loss saturation and self-phase modulation.

Linear Effects Step

In order to account for the gain bandwidth and dispersion, we combine Equations 3.12,3.14 to obtain

$$A_{out}(\tau) = \mathcal{F}^{-1} \left[\tilde{A}_{in}(\omega) \exp\left(\frac{-\Gamma t_2^2 g_p L}{2} \omega^2\right) \exp\left(\frac{j\beta_2 L}{2} \omega^2\right) \right] \quad (3.38)$$

where \mathcal{F}^{-1} represents the inverse Fourier transform operator.

Algorithm

The split-step algorithm first requires a splitting of the laser structure into several sections. The initial pulse is represented in the time domain, as a function of τ , so that the time window can follow the pulse. As the pulse travels through each section, we first shape the pulse using Equations 3.36 and 3.37 in the time domain. Next, the pulse is shaped in the frequency domain via Equation 3.38. Then the pulse passes to the next section and the process repeats. Code in **Matlab** can be found in Appendix A. Figure 3-10 illustrates the simulation model. If an end facet mirror is reached, the pulse bounces back and travels through each section in reverse order. It is useful to examine the shape of the pulse after each round-trip consisting of one forward traversal along the entire laser cavity length and one full reverse traversal. The initial pulse guess will continue to be shaped after each round-trip until it reaches a steady-state solution after several round-trips through the modelocked laser. Figure 3-11 shows a snapshot of the pulse at each round-trip. The laser used in this illustration is two-section and contains a passive section and a gain section. Note the steady-state pulse width and energy after several round-trips. Note also the pulse drifting towards earlier times even after a steady-state shape is reached. This is due to the dominance of the gain saturation effect pulling the pulse forward, faster than its group velocity. This happens because the front of the pulse is amplified while the trailing edge isn't, hence the pulse center-of-mass is dragged forward, as described in Section 3.3.1.

The major difference between a gain section and a saturable absorber section is that $N > N_{tr}$ for the gain region and $N < N_{tr}$ for the absorber region. This implies that the initial unsaturated gain, g_{ss} , and the differential gain, a will be different for each section. For a gain section, $g_{ss} > 0$; for the saturable absorber, $g_{ss} < 0$. The a in the saturable absorber is bigger than the a in the gain section (See Figure 2-15). In addition, no frequency filtering is performed in saturable absorber regions since the gain curve is quite flat for low carrier densities (See Figure 3-6).

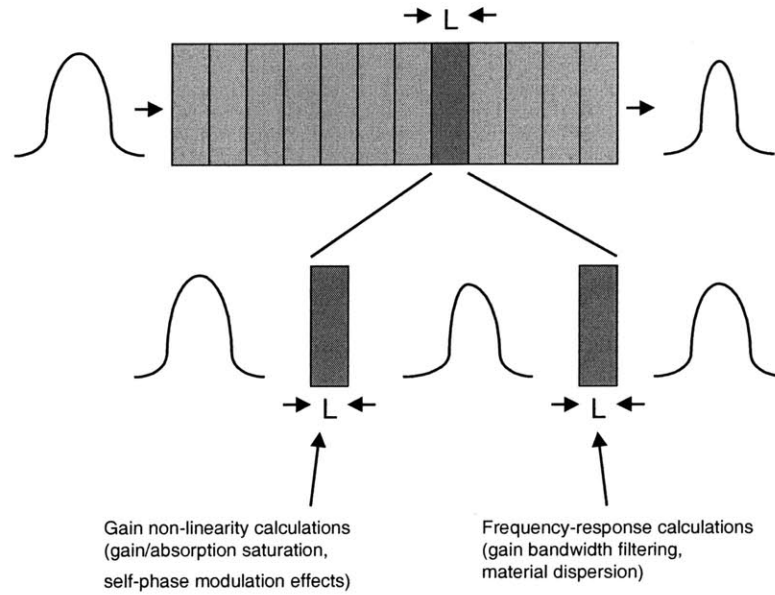


Figure 3-10: Explanation of split-step method

Actively modelocked sections need to be handled outside the regime of the analytic equations. Since the gain is time-dependent, there is no closed form solution to the relationship between the input and output pulse power. One approximation that can be made is to disregard the non-linear gain saturation effects and treat the gain as independent of the photon density. We can use Equation 3.26 to find the carrier density from the time-dependent current. Any arbitrary periodic current function can be used. Typically, a sinusoid is used but more sharply peaked functions can be substituted. Of course, the higher the frequency components of the current function are, the worse an approximation this turns out to be, since Equation 3.26 approximate a quasi-static solution. In addition to this, dispersion and gain bandwidth cannot be implemented since the gain is not constant as the pulse passes through the actively modulated section.

The more sections the laser is broken down into, the shorter each section will be and hence, the more accurate the solution will be. A simple convergence test is to show that the steady state pulse width and energy converge asymptotically to a single value as the

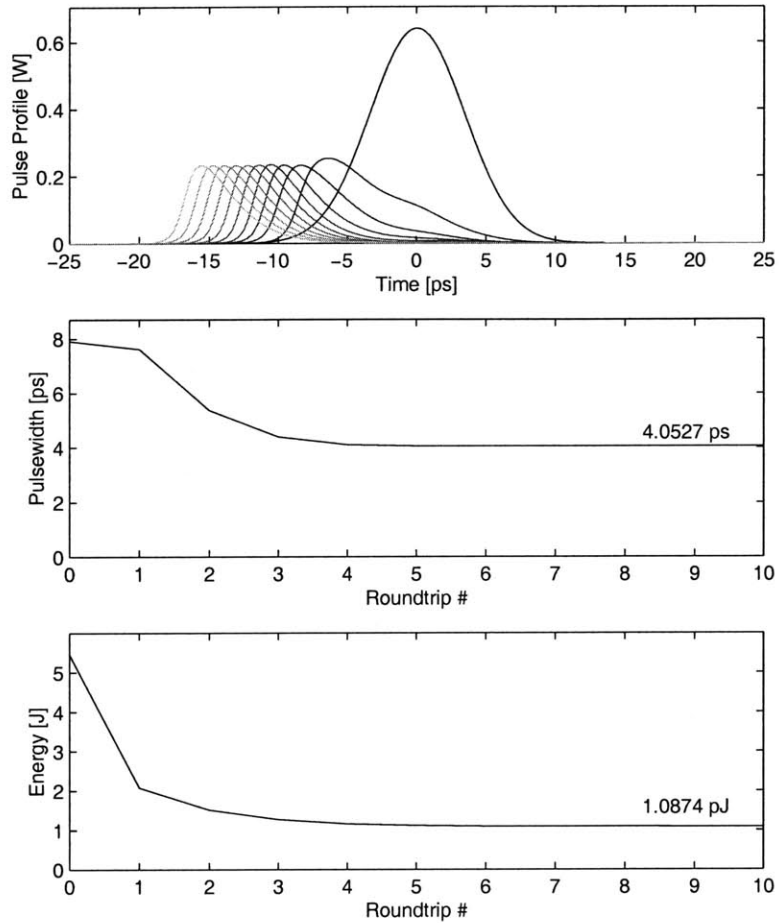


Figure 3-11: Pulse evolution from split-step simulation. Pulse evolves dark to light pulse lines. $I_{gain} = 63mA$, $g_{sa} = -7776cm^{-1}$. The saturable absorber was split into 4 sections of $20\mu m$ each; the gain section was split into 35 sections of $100\mu m$ each.

number of sections increases. This is shown in [28, 16].

3.4.2 Simulation Validity

In order to trust the results of any computer simulation, it is necessary to test its validity by examining simple cases where the simulation results can be checked with analytical results. This section explores the validity of the computer simulation in a collection of limiting cases.

Initial Condition-Independent Steady State

This simulation method uses an initial pulse guess, typically Gaussian, to seed the pulse shaping mechanisms. The user can define the initial pulse height [J] and pulse width [ps]. It is necessary to show that the steady-state pulse solution is independent of the initial guess. Figure 3-12 shows the pulse width and height evolution of several initial guesses. In Figure 3-12(a)&(b), the initial pulse energy is varied. In Figure 3-12(c)&(d), the initial pulse width is varied. In all cases, the steady-state pulse width and energy end up the same.

Gain Bandwidth and Dispersion

Two limiting cases are to test the effects of gain bandwidth and dispersion. This can be accomplished by turning off all effects save the one in question and examining how a pulse evolves through a given length of semiconductor.

Analytic expressions can be obtained that show the effects of, separately, gain bandwidth and dispersion for an unchirped Gaussian pulse input. Assuming an unchirped Gaussian pulse input, analytical expressions showing the effects of gain bandwidth and dispersion filtering can be derived.

First, we assume an unchirped Gaussian pulse input:

$$A_{in}(t) = Ae^{-\frac{t^2}{2\sigma^2}} \quad (3.39)$$

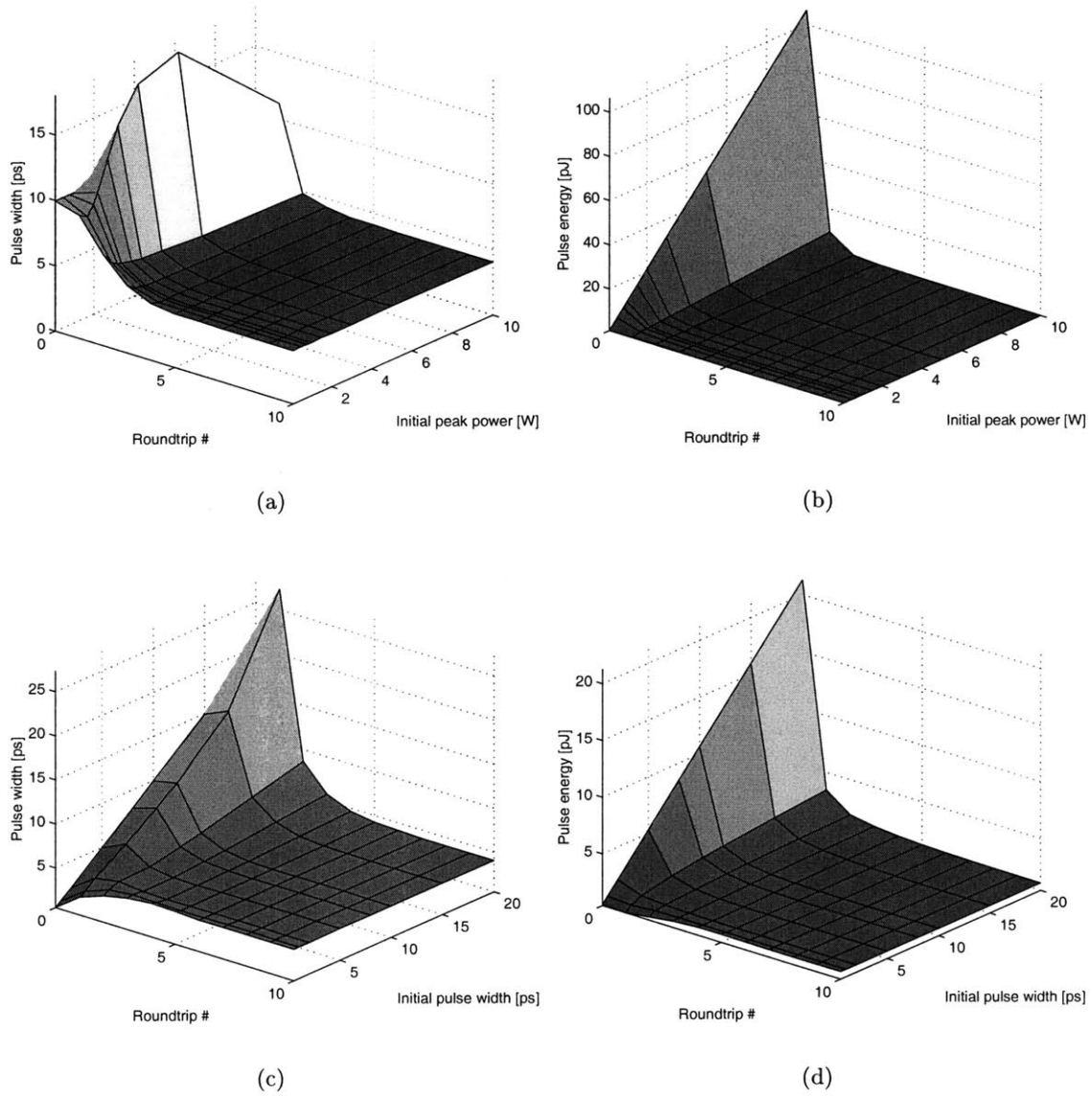


Figure 3-12: Pulse width [(a)&(c)] and pulse energy [(b)&(d)] evolution. (a)&(b) vary the initial pulse energy. (c)&(d) vary the initial pulse width. In all cases, the steady-state pulse width is 4.1ps , pulse energy is 1.1pJ . Laser parameters are the same as in Figure 3-11.

which has a Fourier frequency representation of

$$\tilde{A}_{in}(\omega) = A\sqrt{2\pi\sigma^2}e^{-\frac{\omega^2\sigma^2}{2}} \quad (3.40)$$

We can use the filter:

$$\tilde{A}_{out}(\omega) = \tilde{A}_{in}(\omega)e^{-\frac{\omega^2 G^2}{2}} \quad (3.41)$$

to represent the effects of gain bandwidth on the pulse, where

$$G^2 \equiv t_2^2 g_p L \quad (3.42)$$

The resulting filtered pulse in the frequency-domain is:

$$\tilde{A}_{out}(\omega) = AM\sqrt{2\pi(\sigma^2 + G^2)}e^{-\frac{\omega^2}{2}(\sigma^2 + G^2)} \quad (3.43)$$

where

$$M \equiv \sqrt{\frac{\sigma^2}{\sigma^2 + G^2}} \quad (3.44)$$

The filtered pulse in the time-domain is:

$$A_{out}(t) = AMe^{-\frac{t^2}{2(\sigma^2 + G^2)}} \quad (3.45)$$

and is still Gaussian. This shows that the Gaussian pulse is attenuated by M and widened from σ to $\sqrt{\sigma^2 + G^2}$.

A similar analysis can be performed for dispersion, where the filtering function is

$$\tilde{A}_{out}(\omega) = \tilde{A}_{in}(\omega)e^{-j\frac{\omega^2 D^2}{2}} \quad (3.46)$$

where

$$D^2 \equiv \beta_2 L \quad (3.47)$$

The filtered pulse in the time-domain also remains Gaussian:

$$A_{out}(t) = ANe^{-\frac{t^2}{2(\sigma^2 + jD^2)}} \quad (3.48)$$

where

$$N \equiv \sqrt{\frac{\sigma^2}{\sigma^2 + jD^2}} \quad (3.49)$$

The dispersed pulse is attenuated by $|N|$ and widened to $|\sigma^2 + jD^2|^{1/2}$.

Figure 3-13 shows a comparison of the split-step simulation frequency filtering (due to finite gain bandwidth and dispersion) to the analytical expressions. An unchirped Gaussian envelope was used as the input to both cases. In both cases the simulation exactly matches the analytic expressions in magnitude and only a small phase discrepancy occurs in the far tails of the Gaussian output. This is due to the very small magnitude of the pulse envelope at the edges of the window, contributing to error since the phase is determined by a ratio of real to imaginary portions. This has no effect on the pulse shaping, and the figures demonstrate the validity of the simulation in regards to gain bandwidth and dispersion.

Active Modulation

The split-step method using active modulation can be checked against an analytical model. A simple analytical model was developed by Siegman [58] and also Haus [23]. The formalism used in this thesis is found in [61]. The analytical model used here takes in consideration only active modulation, gain/loss, and finite gain bandwidth. It turns off any non-linear effect as well as dispersion. It linearizes the non-linearity of the active modulation by assuming a small-signal perturbation due to the short width of the pulse compared to the

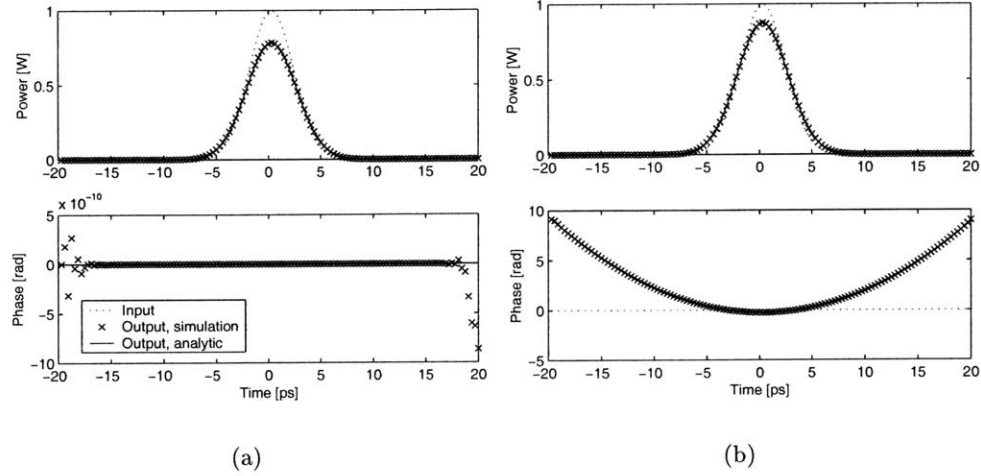


Figure 3-13: Comparison between analytic solution and simulation with (a) gain bandwidth only (b) dispersion only unchirped Gaussian Pulse input, $t_2 = 0.1ps$, $\beta_2 = 10^3ps^2m^{-1}$, $L = 10\mu m$, $g_p = 5 \times 10^4cm^{-1}$ (illustrative purposes)

width of the modulation period.

Assuming a ring cavity as shown in Figure 3-14, a pulse with power profile $v_m(t)$ propagates through the ring, where the subscript is the m -th pass through the cavity. Assuming a gain, g , and loss, α , for the respective sections, the next pass, $m + 1$, should resemble

$$v_{m+1}(t) = e^{gL-\alpha l}v_m(t) \approx (1 + gL - \alpha l)v_m(t) \quad (3.50)$$

if the exponent is sufficiently small enough.

We can now analytically write the various effects of each of the various sections on the pulse.

Expanding g to include finite gain bandwidth (as in Figure 3-7),

$$g(\omega) = g_0[1 - t_2^2(\omega - \omega_0)^2] \Rightarrow g(t) = g_0 \left(1 + t_2^2 \frac{d^2}{dt^2} \right) \quad (3.51)$$

using the inverse Fourier transform of the frequency-domain representation to obtain a

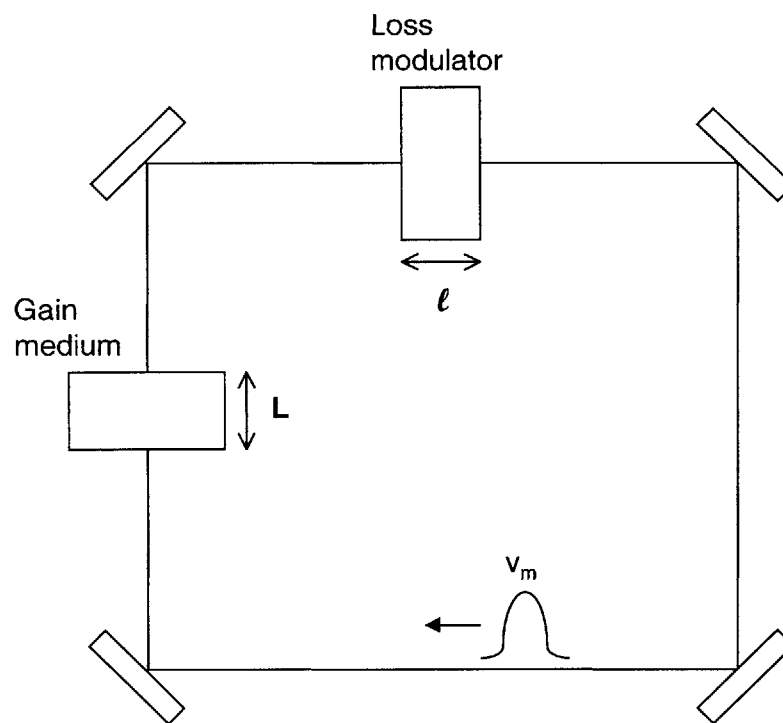


Figure 3-14: Diagram of ring cavity [61].

time-domain representation.

The loss section is modulated sinusoidally at a frequency, ω_M , which is the round-trip frequency of a pulse traveling in the ring cavity.

$$\alpha = \alpha_0[1 + 2M(1 - \cos \omega_M t)] \approx \alpha_0(1 + M\omega_M^2 t^2) \quad (3.52)$$

assuming the pulse passes through the loss section in a very short time interval around the minimum loss point ($t = 0$). At steady-state, this is a good assumption since the pulse will prefer to exist when the loss is least.

At steady-state, the $m + 1$ th pass should equal the m th pass:

$$v_{m+1}(t) = v_m(t) = \left[1 + g_0 L \left(1 + t_2^2 \frac{d^2}{dt^2} \right) - \alpha_0 l (1 + M\omega_M^2 t^2) \right] v_m(t) \quad (3.53)$$

which reduces to

$$\left[(g_0 L - \alpha_0 l) + g_0 L t_2^2 \frac{d^2}{dt^2} - \alpha_0 l M \omega_M^2 t^2 \right] v_m(t) = 0 \quad (3.54)$$

The solutions to this differential equation are Hermite Gaussians, whose lowest order solution is:

$$v_m(t) = V_0 \exp(-t^2/2t_0^2) \quad (3.55)$$

where

$$(g_0 L - \alpha_0 l)^2 = \alpha_0 l g_0 L t_2^2 \omega_M^2 M \quad (3.56)$$

and

$$t_0 = \sqrt{\frac{g_0 L t_2^2}{g_0 L - \alpha_0 l}} \quad (3.57)$$

Pulse evolutions using the split-step simulation can match the analytical solutions by turning off gain/loss saturation, self-phase modulation, and dispersion forces. Figure 3-15 shows pulse evolutions of three different initial Gaussian pulse widths. Only the middle one remains constant, since this used the predicted pulse width as an initial guess. In addition, the pulse shape remained perfectly Gaussian. Any arbitrary pulse energy, V_0 , can be used, since this turns out to be a free parameter in the analysis.

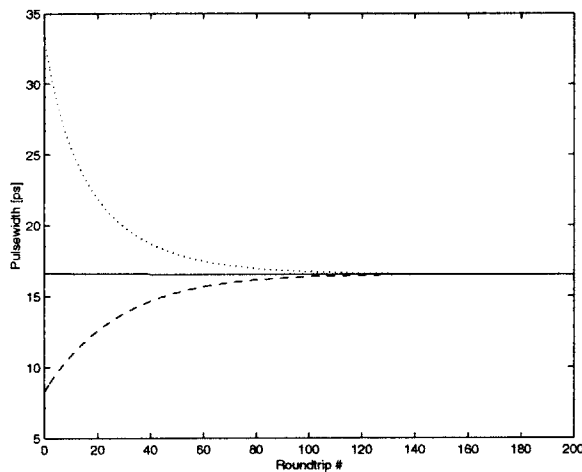


Figure 3-15: Pulse width evolution with various initial pulse widths. Each reach the same steady state. $L = l = 50\mu m$, $g_0 = 4cm^{-1}$, $\alpha_0 = 2cm^{-1}$, $M = 506.6059$, $\omega_M = 2\pi \times 1GHz$, $t_2 = 5ps$

3.4.3 Limitations and Improvements

The split-step method is a computationally efficient, instructional model of the pulse dynamics in a modelocked laser. It can take in account most of the dominant effects that govern pulse shaping within a semiconductor laser. Since the pulse is represented in the time-domain, insight can be gained by watching pulses evolve through each of the different sections.

However, there are many approximations that are made in this model that make it difficult to use this simulation technique as a design tool for building better modelocked lasers.

Active Modelocking Gain

As stated in Section 3.4.1, active modulation is treated poorly in this model. There are no gain saturation or self-phase modulation effects, nor are there gain bandwidth or dispersion effects. While the latter three effects are smaller effects, the lack of gain saturation can have a large effect on the actual pulse shaping. In addition, for short cavity lasers with high repetition rates, the carrier density does not track the injection current modulation. Therefore, erroneous time-dependent gain shapes will show up in the simulation.

It is possible to model the active modelocked sections in a different fashion, such as a finite difference method. However, this leads to a hybrid model simulation with added complexity.

Carrier Density Memory

Immediately before the pulse passes through each section of the laser, the carrier density is assumed to be at the unsaturated steady-state value, N_{ss} . Therefore, the gain is at its unsaturated value, g_{ss} . As stated in Section 3.4.1, this implies that the carrier density will always refresh to its steady-state value by the time the pulse returns to the section. In short cavity lasers with moderate current biases, this is not true, since the pulse visits each laser section at an average rate of two times the modelocked frequency. Furthermore, this is definitely not true for laser sections near the facets, since there is very little time between the propagation of the pulse through the section as it approaches the facet and the propagation as it goes away from the facet. The largest error will occur in these sections.

To this end, the split-step method will always predict unusually low current densities needed to achieve modelocking. Since gain is always refreshed, the current density need not be as high as it should be in order to predict modelocking. Therefore, it is difficult to use the method to predict threshold currents. This fact can be seen in [16], where design curves are stated only in terms of gain, not currents.

By introducing a carrier density state variable, we can keep track of the carrier density for each section division and easily calculate how much it changes due to the passage of a

pulse through the section. Since the length of each section and the time it takes to travel through it is linked by the group velocity, we can easily calculate the time step as the pulse goes from section to section. The carrier density can then be crudely updated each time step due to carrier relaxation and carrier injection via the current. This will allow us to have greater confidence in results given by short, high-repetition modelocked laser cavities, where the carrier density in a section is not refreshed to its steady-state value before the pulse returns to the section.

$$\frac{\partial N}{\partial t} \approx \frac{\Delta N}{\Delta t} \quad (3.58)$$

Using Equation 3.7, this leads to:

$$\Delta N_m = \left[\frac{\eta_i I}{qV} - \frac{N}{\tau_c} - \frac{\Gamma g_p}{h\nu W d} |A^+(z, t) + A^-(z, t)|^2 \right] \Delta t \quad (3.59)$$

where N_m represents the carrier density at the m -th section.

Analytical Solution Approximations

As stated in Section 3.4.1, the approximations made in order to obtain the analytical gain/loss saturation equations where that 1) $\alpha_i < \Gamma g(N)$ 2) a linear gain model and 3) no carrier refreshing during the period in which the pulse passes through the section.

Multiple Pulse Formation

Since the representation of the pulse is in the pulse's group velocity frame-of-reference, It is impossible to keep track of multiple pulse formation due to internal finite reflectivities. For example, if the modelocked laser had an external cavity and the facet facing the external cavity had a finite reflectivity (a non-ideal anti-reflective (AR) coating), then reflections will happen at this boundary. These reflections will cause multiple pulses to form, as noted in [28, 47]. The split-step model cannot keep track of all these pulses, since the representation is in the time domain, not in space.

3.5 Summary

In this chapter, the theory of the pulse-shaping mechanisms important in semiconductor modelocked lasers has been explained. The dominant effects discussed here are gain/loss saturation, self-phase modulation, dispersion and gain bandwidth. A split-step simulation method was presented, and tested for validity. The most important effects for determining steady-state pulse width and energy are gain/loss saturation and finite gain bandwidth. While the split-step model is informative and provides much intuition to the pulse shaping mechanisms found in a modelocked laser, its utility as a design tool is limited due to the approximations it makes.

Equations 3.1 and 3.2 are non-linear, coupled differential equations in two dimensions. An obvious method to solve them is through a finite difference solution, as stated in the beginning of Section 3.4. The next chapter is devoted to this simulation technique.

Chapter 4

Finite Difference Simulations

4.1 Introduction

Finite difference methods are simple, yet powerful, methods for finding solutions to complex differential equations. Several authors [31, 5, 44, 28] have applied finite difference methods to modelocked lasers by discretizing the laser rate equations. However, they do not implement the second-order effects of finite gain bandwidth and dispersion found in these equations. A new method is presented that improves on the existing algorithms found in the literature. This split-step finite difference (SSFD) method is a powerful and accurate method for theoretically exploring the dynamics of modelocked pulses and provides quantitative insight to modelocked laser design. It combines finite difference gain and non-Fourier filtering in a split-step scheme. In this chapter, the finite difference method is introduced and applied to the laser rate equations. A few currently published methods are reviewed with their strengths and weaknesses. For purposes of future research, a comprehensive list of alternative methods that lead to the SSFD method are presented. The SSFD method is then introduced and tested for validity. It is then used to provide performance trends in various parameter spaces for laser design purposes. In addition, promising, but not fully developed methods are also presented, including their advantages and issues.

4.2 Summary of Simulation Methods

This section provides a summary of the published simulation methods found in the literature. First, the previously introduced methods are restated for reference. Then, several other methods not previously mentioned are summarized.

The first method discussed in the thesis was the split-step method analyzed in Chapter 3. Derickson derives this method from the split-step Fourier method developed by Agrawal et al. [1] for use with fiber optic pulse propagation and the partial integration technique developed by Helkey et al. [28]. The approximations it utilizes renders it unsuitable for practical design work, however it provides good insight for understanding the behavior of modelocked lasers.

Several finite difference methods already exist. Carroll et al. develop a method originally developed for use with DFB lasers [31]. They provide the first insight in using a non-Fourier domain filter to approximate the finite gain bandwidth, paving the way for the development of the SSFD method.

Morton et al. publish a simple finite difference method and use it to model external cavity, single section active modelocked lasers [5]. Since the single section is used in a gain mode, the narrowing effect is provided by the active modulation and therefore will not suffer from unbounded narrowing like that discussed in Section 4.4.1. It is unsuitable for any laser with a passively-modelocked section.

For completeness, two methods of including gain bandwidth are mentioned. Schell et al. [55] implement a method similar to Carroll's method, but suffers from the same problems found in Section 4.6. They attempt to implement a Lorentzian-shaped gain spectrum in a difference equation, however their filtering is similarly asymmetrical, leading to group velocity issues.

Lowery develops the Transmission Line Laser Model (TLLM) [42, 41] and applies it to semiconductor modelocked lasers [44]. He expands the method to contain self-phase modulation effects [43]. Lowery uses a finite difference method for gain and transmission line theory to create a filter that simulates gain filtering. However, his filter is placed in

Table 4.1: Table of simulation methods. \checkmark = suitable application. \square = untested but suitable application. \dagger = limitations deter usage. suitable otherwise.

Method (Author)	active	passive	hybrid	external	monolithic	sub-ps	limitations
Split-step Fourier (Derickson) [16]		\checkmark		\checkmark		\checkmark	inaccuracies from approximations
Finite difference (Morton) [5]	\checkmark			\checkmark	\square		no filtering
Transmission-line laser model (Lowery) [43]	\checkmark	\square	\square	\checkmark		\square	filter has limited use
Finite difference, Lorentzian gain model (Schell/Schöll) [55]	\dagger	\dagger	\dagger	\dagger	\dagger	\dagger	incorrect filter
Finite difference, non-Fourier filter (Carroll) [31]	\dagger	\dagger	\dagger	\dagger	\dagger	\dagger	incorrect filter
Split-step finite difference (Lau)	\checkmark	\checkmark	\checkmark	\checkmark	\checkmark	\checkmark	filter has upper limit in usage

only a single part of the laser, namely one of the facets. This simplified solution is not as physical as the method in this thesis.

Also for completeness, a few non-finite difference methods are mentioned here. Several analytical methods are available [55, 54, 23, 61]. These assume functionally-dependent pulse shapes such as $\exp(-t^2)$ or $\cosh^{-2}(t)$ and allow only the function parameters to evolve as the pulse passes through the laser sections. A few methods do not assume an approximated pulse shape, rather perform an analysis entirely in the Fourier domain [24, 66]. These analytic methods frequently leave out secondary effects and impose other approximations in order to achieve a closed-form solution. Schell and Schöll develop an iterative method that transforms the pulse into its eigenfunction components, then amplifying them in the frequency domain [53]. Many approximations, such as infinite gain bandwidth and homogeneously biased (single contact) lasers, are made in this method.

4.3 Laser Rate Equations

Equations 3.4 and 3.5 or their normalized forms found in Equations 3.6 and 3.7 can be solved using approximate numerical methods for solving differential equations. The advantage of this method is that we can explicitly include all the effects listed in Section 3.3 in contrast to the split-step Fourier methods.

The coupled rate equations, in field form, are listed here for convenience:

$$\frac{1}{v_g} \frac{\partial E^\pm(z, t)}{\partial t} \pm \frac{\partial E^\pm(z, t)}{\partial z} = \frac{\Gamma g_p}{2} (1 - j\alpha) E^\pm(z, t) - \frac{\alpha_i}{2} E^\pm(z, t) + \frac{1}{2} (\Gamma g_p t_2^2 - j\beta_2) \frac{\partial^2}{\partial t^2} E^\pm(z, t) \quad (4.1)$$

$$\frac{\partial N(z, t)}{\partial t} = \frac{\eta_i I}{qV} - \frac{N}{\tau_c} - \frac{\Gamma g_p}{h\nu\mu v_g} |E^+(z, t) + E^-(z, t)|^2 \quad (4.2)$$

where it is important to remember the carrier density-dependence of the gain, g_p and carrier lifetime, τ_c :

$$g_p(N) = g_0 \ln \left(\frac{N + N_s}{N_{tr} + N_s} \right) \quad (4.3)$$

$$\tau_c = \frac{1}{A + BN + CN^2} \quad (4.4)$$

The spontaneous emission term seen in Equation 2.2 can be added, but it is important to understand the dynamics of the spontaneous emission term when adding it to a solution of the differential equations [30, 64]. Our initial conditions assume an existing pulse of arbitrary shape, therefore the use of the spontaneous emission term as a pulse-creating mechanism is unnecessary. The spontaneous emission term can also be used to simulate timing jitter but is left as a topic for future research. A diffusion term can also be added

to Equation 4.2, but it is a minor effect compared to the photon field term.

The two equations are coupled first-order non-linear differential equations and may also be written as a single second-order differential equation. They are space- and time-dependent.

4.4 Finite Difference Laser Rate Equations

4.4.1 First-Order Finite Difference Approximations

There are several flavors of finite difference methods that can be used to solve the equations. A simple choice of solution is by applying the forward-Euler method to the time derivative found on the left-hand side of Equation 3.1. Instead of allowing the time step to approach zero, $\Delta t \Rightarrow 0$, we can set it to a finite value.

$$\frac{dS^\pm(t)}{dt} \Rightarrow \frac{S^\pm(t + \Delta t) - S^\pm(t)}{\Delta t} \quad (4.5)$$

We have chosen to discretize the photon density equations, without loss of generalization, due to their simplicity. We have lost phase effects but they can be added in separately, as stated in Section 5.2. By noticing that the total time derivative (defined in Equation 3.16) consists not only of a propagation in time but also propagation in space, we can see that

$$S^\pm(t + \Delta t) \Rightarrow S^\pm(z \pm \Delta z, t + \Delta t) \quad (4.6)$$

where Δz and Δt are related by the group velocity, v_g :

$$\frac{\Delta z}{\Delta t} = v_g \quad (4.7)$$

Essentially, we have chosen the total time derivative to follow the photon density at the speed of propagation. Hence, we can see how the photon density increases and decreases

due to its interaction with the gain medium [67].

This method can easily account for all first-order derivative terms. However, since dispersion and gain bandwidth require second-order derivatives, they cannot be accounted for as easily. In this first-order approximation, all second-order derivatives are ignored. The final equation that relates the current time step to the next is:

$$S^\pm(z \pm \Delta z, t + \Delta t) = S^\pm(z, t) + \Delta t [v_g(\Gamma g_p(z, t) - \alpha_i)S^\pm(z, t)] \quad (4.8)$$

where g_p is written with space- and time-dependence to remind the reader that g_p depends on the carrier density, $N(z, t)$. The carrier rate equation is simpler since the partial equals the total derivative.

$$N(z, t + \Delta t) = N(z, t) + \Delta t \left[\frac{\eta_i I(z, t)}{qV} - \frac{N(z, t)}{\tau_c(z, t)} - v_g g_p(z, t)(S^+(z, t) + S^-(z, t)) \right] \quad (4.9)$$

4.4.2 Implementation

Implementation of these two equations has a simple and straightforward recipe.

1. Choose a sufficiently small time step (Δt) and the space step (Δz) can be found through the group velocity.
2. Split the laser cavity length into equally spaced segments of length Δz .
3. Create state variables for N_i , S_i^+ , and S_i^- , where i is used to enumerate each cavity segment (See Figure 4-1).
4. Choose an initial photon density of an assumed pulse within the cavity. One can set S^- to zero and place the seed pulse in S^+ .
5. Choose an initial carrier density. It is convenient to choose a uniform carrier density at transparency or at steady-state with no photons.
6. Propagate the pulse one time step, Δt , by calculating the state variables for the new time step.

7. Apply boundary conditions to couple S^+ and S^- together.
8. Repeat propagation until a steady-state is reached.

All the variables in Equation 4.8 can vary in time and space, thus leading to non-linearity in the rate equation solutions. Particularly, $g_p(z, t)$ and $\tau_c(z, t)$ can be found through Equation 4.3, since the carrier density, $N(z, t)$, at each time step is known. The injection current can also vary in space, in multi-section current-biased lasers, for example, and in time, leading to active modulation biased laser sections (See Figure 4-1).

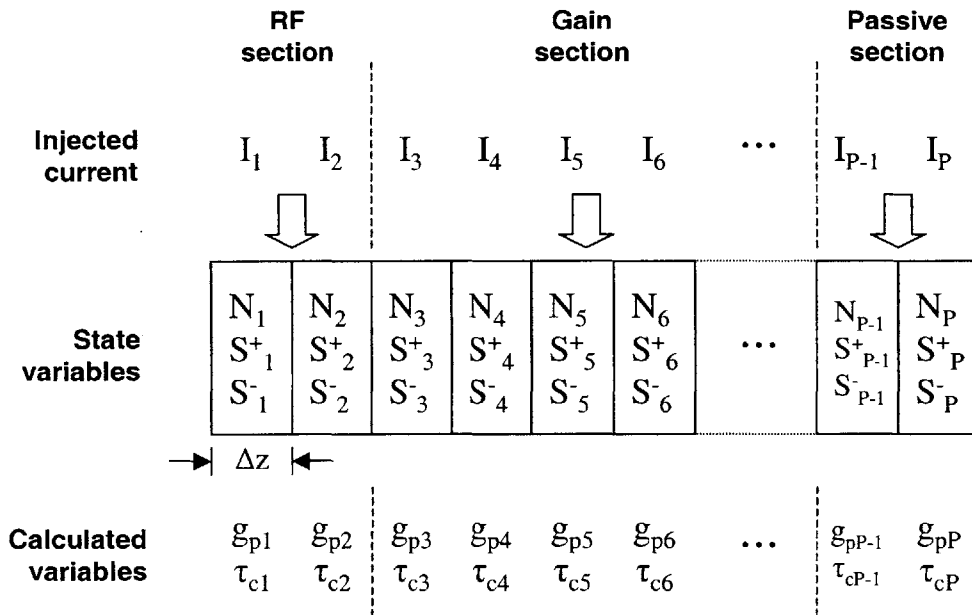


Figure 4-1: Illustration of the state variables in a three-section laser structure with P sections. The total laser length is $P\Delta z$.

The proper choice of the length of the time segment (and hence, the length segment) is important to arriving at a stable and accurate result. It is apparent that the shorter the length of the segment, the closer to a true derivative the results become. However, too short a length will result in a slow simulation program. Execution time goes as $O[(\frac{1}{\Delta z})^2]$. The time segment is chosen by running the simulation with different time steps and noting

trends. Regardless of the choice of time step, if the simulation reaches a steady-state then the solution is stable. If the simulation asymptotically converges to the same stable result as the time step is reduced then it is a correct solution. By examining the diminishing returns of increased accuracy versus decreased time step, one can choose a time step that produces a sufficiently correct solution in the minimal amount of computing time. A sufficiently correct solution can be defined as one that does not deviate from the asymptotically approached answer by more than a certain percentage.

Boundary conditions can be found at the laser segments that correspond to the end facets. In a laser with P sections, this would correspond to sections 1 and P . Based on the reflectivity of the laser facet, we can couple the forward and reverse propagating photon densities together. For example, given a reflectivity R for both mirror facets, the right-hand mirror facet implies

$$S_P^-(t + \Delta t) = R_{right} \times S_P^+(t) \quad (4.10)$$

and the left-hand mirror implies

$$S_1^+(t + \Delta t) = R_{left} \times S_1^-(t) \quad (4.11)$$

Internal boundary conditions can easily be added to simulate the effects of internal reflective surfaces that may result in coupled-cavity effects. These boundaries occur at the junction between the different functional sections in a multi-section modelocked laser (See Section 4.8 for results).

The laser output is asymmetrical and can be observed by the complementary boundary conditions:

$$S_{out}^+(t + \Delta t) = (1 - R) \times S_P^+(t) \quad (4.12)$$

and the left-hand mirror implies

$$S_{out}^-(t + \Delta t) = (1 - R) \times S_1^-(t) \quad (4.13)$$

The finite difference programs were written in **Matlab** (See Appendix A).

4.4.3 Calculating Error

It is necessary to estimate the error in the finite difference calculations in order to determine which method is more accurate than another. One form of error estimation is by Taylor expansion. We first note that expanding $S(t)$ around t at intervals of $\pm\Delta t$ gives exact solutions:

$$S(t + \Delta t) = S(t) + \frac{d}{dt}S(t)\Delta t + \frac{1}{2}\frac{d^2}{dt^2}S(t)\Delta t^2 + \frac{1}{6}\frac{d^3}{dt^3}S(t)\Delta t^3 + \dots \quad (4.14)$$

$$S(t) = S(t) \quad (4.15)$$

$$S(t - \Delta t) = S(t) - \frac{d}{dt}S(t)\Delta t + \frac{1}{2}\frac{d^2}{dt^2}S(t)\Delta t^2 - \frac{1}{6}\frac{d^3}{dt^3}S(t)\Delta t^3 + \dots \quad (4.16)$$

From these equations we can find the error for the Euler method above:

$$S(t + \Delta t) - S(t) = \frac{d}{dt}S(t)\Delta t + \frac{1}{2}\frac{d^2}{dt^2}S(t)\Delta t^2 + \frac{1}{6}\frac{d^3}{dt^3}S(t)\Delta t^3 + \dots \quad (4.17)$$

$$\frac{dS(t)}{dt} = \frac{S(t + \Delta t) - S(t)}{\Delta t} + \left\{ -\frac{1}{2}\frac{d^2}{dt^2}S(t)\Delta t - \dots \right\} \quad (4.18)$$

Hence, in this last grouping of terms, it is easy to see that the term in curly braces is the error and that it is dominated by the second-order derivative term.

We can develop a more accurate approximation for the first-order derivative terms by including past values of $S(t)$ (Equation 4.16):

$$S(t + \Delta t) - S(t - \Delta t) = 2\frac{d}{dt}S(t)\Delta t + 2\frac{1}{6}\frac{d^3}{dt^3}S(t)\Delta t^3 + \dots \quad (4.19)$$

$$\frac{d}{dt}S(t) = \frac{S(t + \Delta t) - S(t - \Delta t)}{2\Delta t} + \left\{ -\frac{1}{6}\frac{d^3}{dt^3}S(t)\Delta t^2 - \dots \right\} \quad (4.20)$$

This filter is symmetrical around $S(t)$. The error, in this case, is dominated by the third-order derivative term and in general will be smaller than the previous case. In general, we can continue adding symmetrical terms around $S(t)$ to improve the error and increase the order of the largest error term. However, the trade-off is the requirement of a shorter time step, since the estimation of a derivative at a specific point should be as local as possible. The addition of terms requires values further away from the derivative point, which will increase the error of the derivative calculation (See text on Numerical Analysis for a more rigorous discussion [52]).

4.5 Classic Finite Difference Simulation Results

4.5.1 First-Order Derivative Finite Difference Equations

First, let us examine the results of running a finite difference simulation using only laser rate equations without the second-order derivatives. The advantages of this method is the simplicity in implementation. It is also relatively fast since no history of past state variables (at $t - \Delta t$) is needed. The problems with this method are two-fold. First and most obvious is the fact that the Euler method of solution can contain errors that may compound after each time step. The second is that since no dispersive or gain bandwidth effects can be employed, a passive or hybrid modelocked laser will have dominant pulse narrowing effects with insufficient broadening terms to keep the pulse from narrowing to singularity. In fact, if a simulation using the Euler method is run, this indeed happens. Figure 4-2 shows multiple snapshots of the pulse profile within the laser cavity. The time difference between each snapshot is the round trip period calculated from twice the round-trip cavity length divided by the group velocity ($t_{r.t.} = 2L_{tot}/v_g$) (notice the pulse drifting similar to observed in the split-step method). The pulse propagates and begins shaping initially, but continues to narrow to impossible pulse widths. The position (x-) axis shows the passive section on the left-hand side ($80\mu m$) and the active section on the right ($100\mu m$), with the gain section occupying the remaining middle section ($3500\mu m$). The biasing is set to $500mA$ in the gain

section, $10mA - DC$ with $200mA - RF$ set at the round-trip frequency for the active section. It begins as the low power, central pulse snapshot (obscured by other pulse trails). The initial pulse begins at $2ps$, each successive pulse snapshot drifting toward the right facet of the laser. The right-most pulse shown has a width of $0.2ps$, which is impossible for a typical semiconductor laser due to gain bandwidth restrictions. Further propagation would result in increasingly-narrower pulses. Eventually, the pulse will occupy a single discretized point. Hence, gain bandwidth is an important effect that cannot be left out of a semiconductor modelocked laser model.

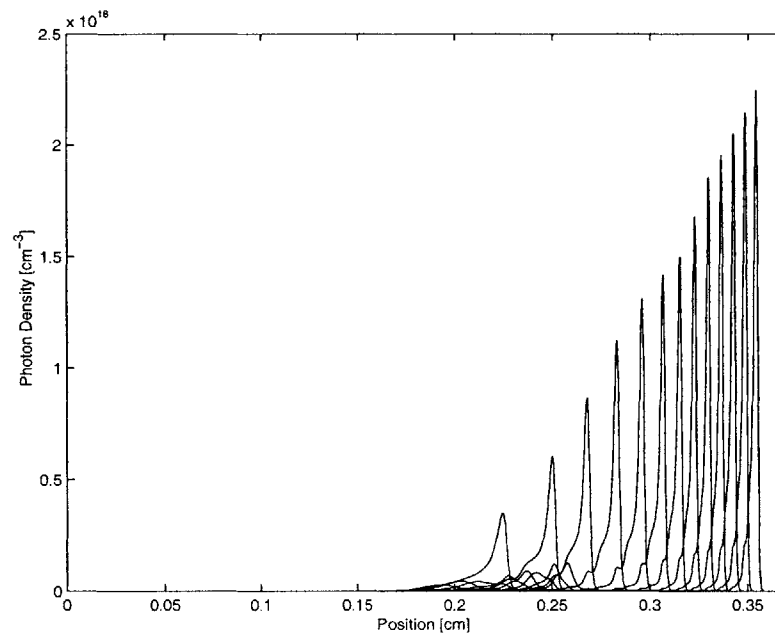


Figure 4-2: Pulse evolution with insufficient broadening forces (infinite gain bandwidth). Selected round trip snapshots are shown.

Previous first-order finite difference simulations that do not provide finite gain bandwidth [5] have not suffered from the singularity asymptote effect. Since their model uses a single-section, external cavity actively modelocked laser, there are no passive sections to supply the dominant pulse narrowing effect that forces the pulse to singularity. Rather, the narrowing effect is simply the weakly-confining gain shape provided by the active modula-

tion and the spatially inhomogeneous current biasing.

4.5.2 Second-Order Derivative Finite Difference Equations

The most obvious choice for including the second-order derivative terms is by approximating the derivative as a finite difference term, as shown in Appendix B. We can use an asymmetric, causal approximation, such as Equation B.4. Again, the positive points about this method is that it is relatively simple in concept. However, because of the many terms needed, this method requires more memory accessing and greater iteration time. This method also seems to have severe stability problems. Even before the pulse propagates half the length of the cavity, the error exponentially increases until it becomes greater than the pulse itself. This is shown in Figure 4-3. Figure 4-3(a) shows the initial pulse. Figure 4-3(b) shows the pulse at a later time. The inset shows a blown-up segment of the pulse. Note that the profile is no longer smooth, rather it has become rough. This alternating roughness increases without bound. Figure 4-3(c) shows the pulse at a point in which the error is on the order of magnitude of the pulse power. Figure 4-3(d) shows a point in which the error is many orders of magnitude larger than the pulse power. This represents the exponential increase in the error.

It is unclear how to calculate the error and verify that it exponentially increases. Asymmetric approximations of the partial derivative that include 5-15 previous terms (hence smaller error but larger past memory) were tried with no marked improvement to the stability. Up to 100 terms were tried with similar results (however, such drastic numbers may run into truncation errors and other problems). In finite difference simulations, especially multi-dimensional simulations, quantitative error analysis is difficult. There are methods of determining stability. It is also unclear if these methods can be applied to this problem formulation. Future work should be done to estimate the error [52]. This unbounded error relates closely to the symptoms found in η_F limitations for the filtering technique described in Section 4.7.1.

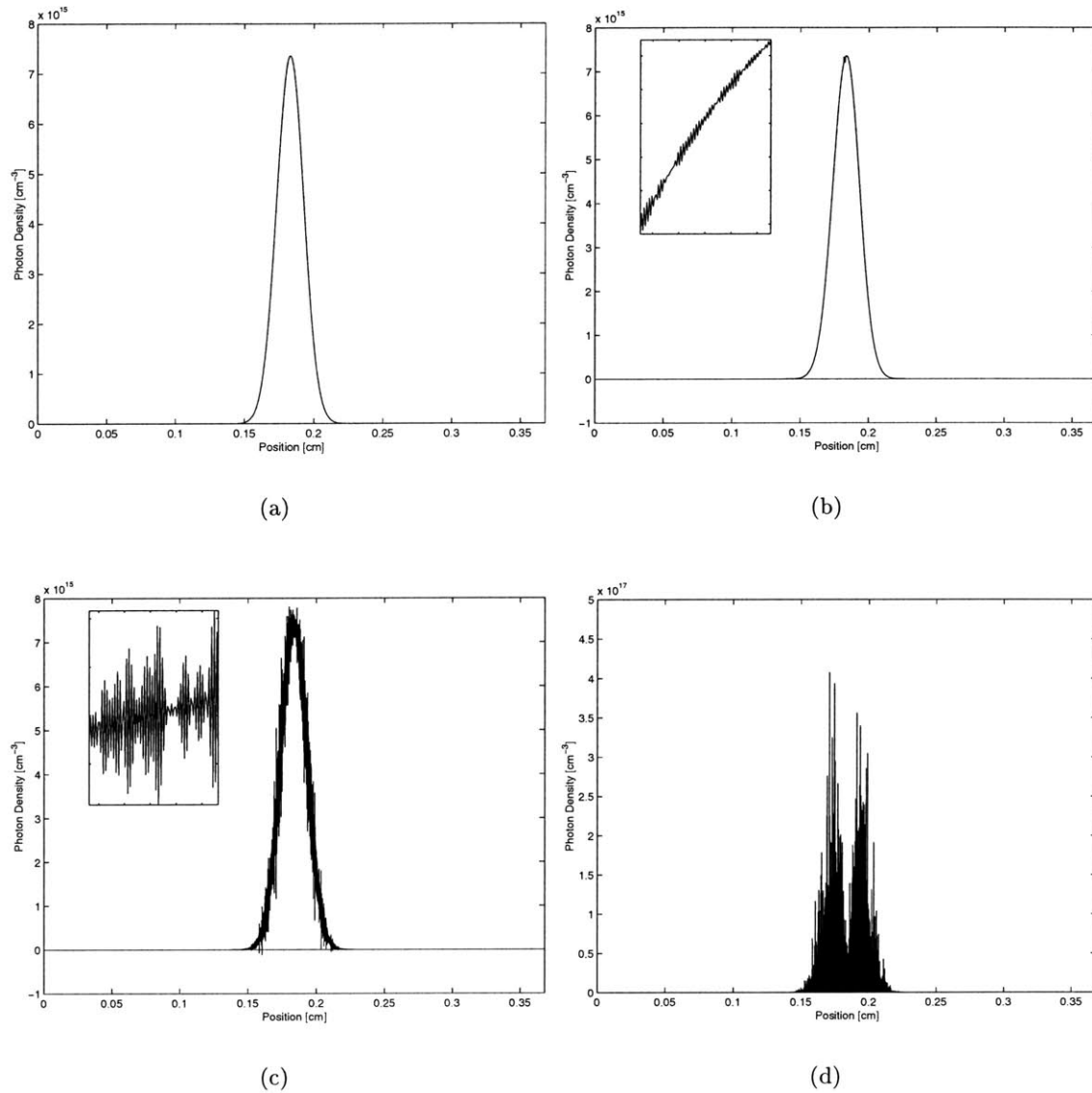


Figure 4-3: Pulse evolution using unstable finite gain bandwidth implementation. (a) the initial pulse ($t = 0$ fs). (b) the pulse at the threshold of instability ($t = 58$ fs). (c) the pulse exhibiting significant instability ($t = 63$ fs). (d) the pulse well beyond the threshold of instability ($t = 70$ fs).

4.6 Difference Equation Filtering

Another method for including the gain bandwidth parameter is through using a digital difference equation filter. This technique was pioneered by Carroll et al. when they simulated pulse propagation in colliding pulse modelocked semiconductor lasers [31]. It recognizes that the laser pulses have a minimum achievable pulse width, hence their bandwidth remains limited. In fact, the bandwidth of the photon field is limited to only a small range of the much wider material gain bandwidth (See Figure 3-7). This same fact allowed us to approximate the gain peak with a parabolic profile in Figure 3-7 for the split-step method. We can further take advantage of this by creating a digital filter that matches the gain profile only in the frequencies within the bandwidth of the photon field. The shape of the filter can be allowed to deviate from the actual gain profile outside of the bandwidth of interest.

Carroll et al. take the frequency response of their filter as:

$$|H(\omega)|^2 = \frac{(1 - \eta)^2}{1 + \eta^2 - 2\eta \cos[(\omega - \omega_0)\Delta t]} \quad (4.21)$$

where ω_0 is the center frequency of the gain peak (as in Section 3.3.2), Δt is the time step, and η is the bandwidth parameter. Since we have already assumed a gain peak recentered to zero, $\omega_0 = 0$. The bandwidth parameter takes values from $0 < \eta < 1$ and a prudent choice allows us to match the gain spectrum within the pertinent frequency range. Figure 4-4 shows the parabolic gain spectrum and various values of η from [31], given a time step $\Delta t = 150fs$.

Carroll et al. state that the difference equation implementation of this filter for a forward propagating wave is:

$$E^+(z + \Delta z, t + \Delta t) = AE^+(z + \Delta z, t) + (1 - A)E^+(z, t) \quad (4.22)$$

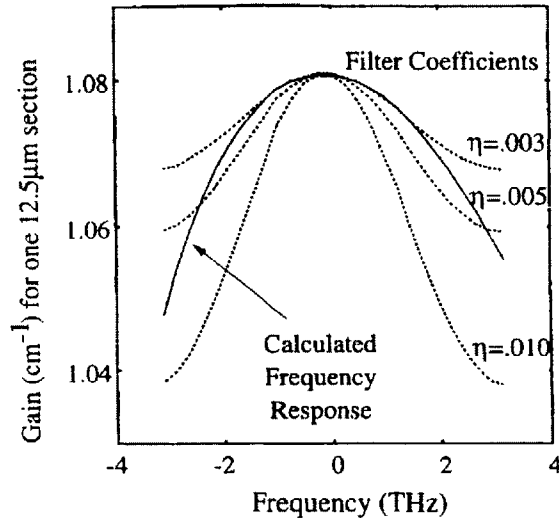


Figure 4-4: Parabolic gain spectrum model and the frequency response of filters with varying η (From [31])

where

$$A = \eta \exp(j\omega_0 \Delta t) \quad (4.23)$$

The term A in Equation 4.22 is typically small. If $A = 0$, then Equation 4.22 reduces to:

$$E^+(z + \Delta z, t + \Delta t) = E^+(z, t) \quad (4.24)$$

This means that there is no filtering performed and the field at z simply travels to $z + \Delta z$ in the time interval between t and $t + \Delta t$. The filtering simply means that we are taking the field at time t and performing a weighted average of two adjacent points together: the majority of the field at z and a small amount of the field at $z + \Delta z$. This averaged result is what travels to $z + \Delta z$ at $t + \Delta t$. Averaging can be explained as a form of low-pass filtering, so this accomplishes our goal of limiting the gain bandwidth. However, there are several issues with the technique:

1. The filter parameter, η , is determined incorrectly. This is explained in the next section.
2. The low-pass filtering (averaging) is performed in space, not time. In Equation 4.1, the filtering is a function of the double partial in time. Filtering in space could be performed if the gain bandwidth term was a partial in space. Since it is not, the only other way that a filter in space would make sense is if the partial in time and space were proportional to each other. As seen in Equation 3.16, the partial in time and space of the photon density are not proportional. In other words we would be able to claim, if this were true,

$$\frac{\partial}{\partial t} S^+(z, t) = \frac{1}{v_g} \frac{\partial}{\partial z} S^+(z, t) \quad (4.25)$$

Because the gain on the right-hand side of Equation 3.16 is not negligible compared to the terms on the left, these are not equivalent. To show that this approximation cannot even be made, we will analyze Equation 3.1. Given a Gaussian photon density profile:

$$S^+(z, t) = S_0 \exp \left[-\frac{(t - z/v_g)^2}{2\tau^2} \right] \quad (4.26)$$

we observe that:

$$\frac{\partial}{\partial t} S^+(z, t) = -\frac{(t - z/v_g)}{\tau^2} S^+(z, t) \quad (4.27)$$

$$\frac{\partial}{\partial z} S^+(z, t) = \frac{(t - z/v_g)}{v_g \tau^2} S^+(z, t) \quad (4.28)$$

When compared with

$$v_g(\Gamma g_p - \alpha_i) S^+(z, t) \quad (4.29)$$

we see that around the peak of the pulse, $t - z/v_g = 0$, that both partials are close to

zero. Therefore, the approximation made in Equation 4.25 is not appropriate at the pulse peak.

3. The major problem with the filter lies in the fact that the weighted averaging is not symmetric around the space point z . As seen in Equation 4.22, the weighting is the majority of $E^+(z, t)$ (as it should be) and a fraction of $E^+(z + \Delta z, t)$. Since the latter term is ahead in space to the former term, the averaging causes the pulse to be shifted slightly backward in space. In a limiting case, think of a single impulse in space and time. Without a filter, the impulse advances at the group velocity. When the filter is applied, it begins to spread, but only to points behind it in space, since the filter is asymmetrical. In filter theory terms, this can be explained by examining the frequency response of the filter. The filter is complex, which results in phase shifts in the output. These phase shifts are Fourier-transform-equivalent to shifts in time, or equivalently a time delay. This has been shown through simulation that the pulse is actually slowed down. Physically, this should not happen. This problem can be solved by creating a symmetric filter. This technique is discussed in Section 4.7.1.

For completeness, Carroll has since written a text on simulating distributed feedback lasers with gain filtering using a similar, but more refined technique [7]. However, application to modelocked lasers is still questionable. The text is mentioned for further research on this method.

4.7 Split-step/Finite Difference Simulation

Carroll's method provides inspiration to a suitable method of implementing the finite gain bandwidth term. The key to implementing a correct digital filter is to re-examine the split-step method in Chapter 3.

The split-step method separated the linear and non-linear effects of the laser rate equations into two steps, thus allowing for: 1) the integration of the non-linear terms over the space interval, thus allowing for the use of longer intervals and 2) the use of a Fourier-domain

frequency filter to implement the linear terms. The purpose of this method was improved computational time primarily due to the partially-integrated rate equations while still maintaining the effects of the linear terms through a two-step process. The negative effects were the approximations that one had to make in order to perform the partial integration of the non-linear effects.

The finite difference method shows improved accuracy and a more physical implementation of the rate equations. The primary goal of this section is to develop a simulation technique that combines the two methods, thus achieving maximum accuracy with the ability to include linear effects such as finite gain bandwidth and dispersion.

Since finite difference methods have been proven to be an effective technique for describing the non-linear dynamics of the laser rate equations, this portion of the problem is solved. What needs to be accomplished is a way to implement the linear effects. In the split-step method of Chapter 3, the filtering was performed by a Fourier-domain filter. This was possible because the pulse was stored as a function of time, not space. At each laser segment, the entire time window containing the pulse was "sifted through" the space increment twice: once for the non-linear effects and once for the linear effects. For the finite difference models, the pulse is stored in space rather than time, making a Fourier-domain filter impossible to implement.

4.7.1 Symmetric Difference Equation Filtering

The method for realizing a time-domain filter can be accomplished through a digital filter, in the spirit of Carroll's work [31] in Section 4.6. However, rather than a space-domain difference equation, a time-domain difference equation will be used. Following Carroll's formalism in Equation 4.22, we can write a similar one for the time domain, using photon densities rather than fields:

$$S_F^\pm(z, t + \Delta t) = \eta S^\pm(z, t - \Delta t) + (1 - \eta) S^\pm(z, t) \quad (4.30)$$

where $S_F^\pm(z, t)$ represents the newly-filtered photon density. Additionally, the photon density has not yet translated spatially. Only after the filtering has been performed, then the boundary conditions are implemented and the pulse is allowed to translate in space at the group velocity.

This filter, unfortunately suffers from the same drawbacks of the one in Equation 4.22. Since it is asymmetric around $S^\pm(z, t)$, it will cause the pulse to slow down in the same manner. The way around this is to use a symmetric filter:

$$S_F^\pm(z, t + \Delta t) = \eta S^\pm(z, t - \Delta t) + (1 - 2\eta)S^\pm(z, t) + \eta S^\pm(z, t + \Delta t) \quad (4.31)$$

The Fourier transform of the difference equation becomes:

$$\frac{\tilde{S}_F^\pm(z, \omega)}{\tilde{S}^\pm(z, \omega)} = 1 + 2\eta [\cos(2\omega\Delta t) - 1] \quad (4.32)$$

This filter, similar to a second partial in time, is real and does not affect the speed of the pulse propagation.

Since we are using the filtering in the same manner as the split-step method, the implementation is similar to that stated in Section 3.3.2. We are trying to implement a filter similar to the Fourier-domain filter in Equation 3.12:

$$\frac{\tilde{S}_{out}(\omega)}{\tilde{S}_{in}(\omega)} = \exp[-\omega^2 t_2^2 \Delta z \Gamma g_p(N)] \quad (4.33)$$

However, since our filter is not the same, we try to match the filter response over the frequency range of interest and allow our difference equation filter to have arbitrary response outside this range. The matching is accomplished by two parameters: Δt and η . η is a free parameter, however Δt affects the accuracy of the finite difference portion of the simulation, so keeping this fact in mind is important. Essentially, Δt cannot be made too large. Figure 4-5 shows the fitting of the digital filter's gain bandwidth to that of the Fourier-domain filter.

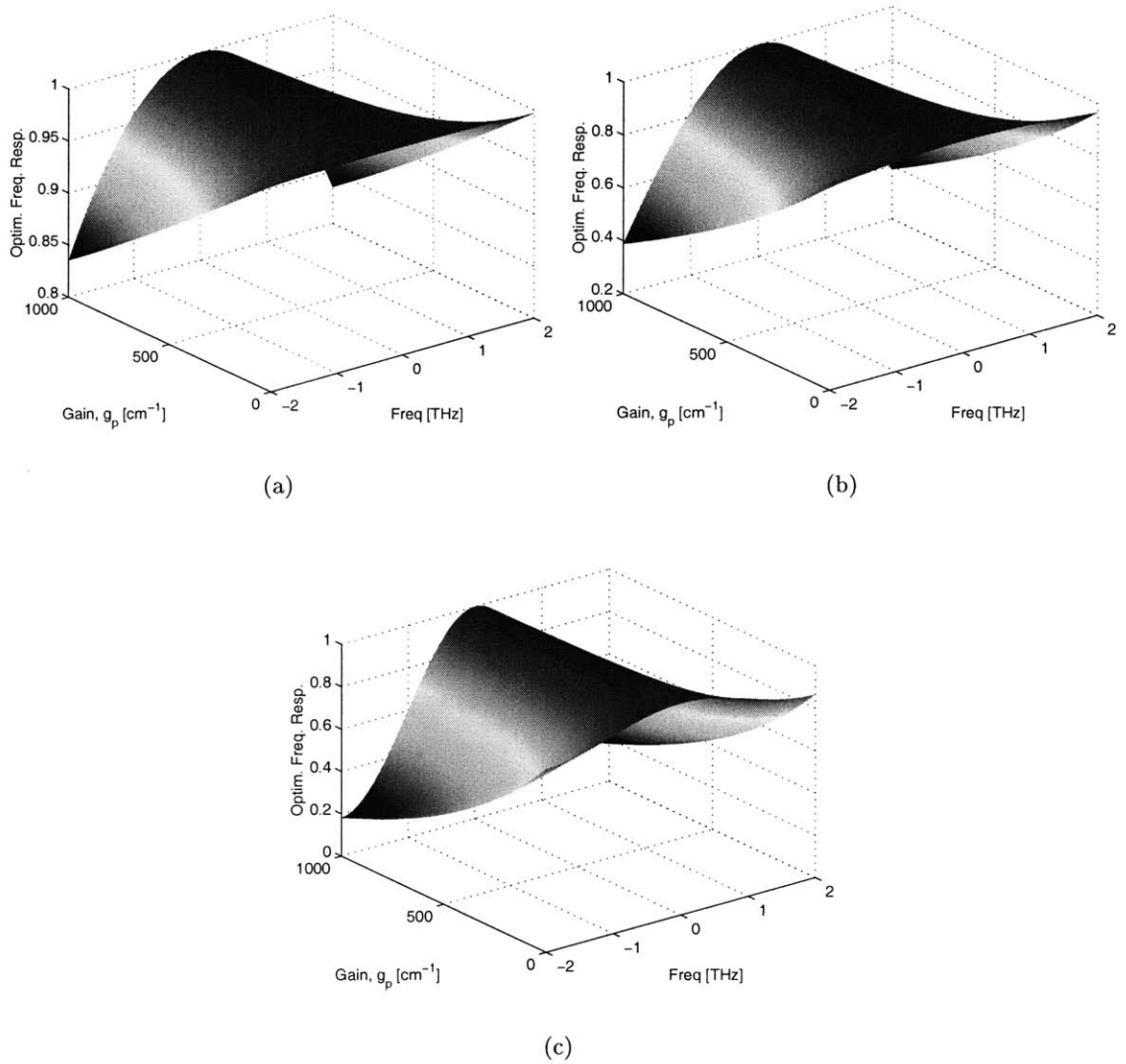


Figure 4-5: Fitting of the digital filter parameter, η , for various Δt . The fit is to Equation 4.33 for a given $t_2 = 5 \times 10^{-13} \text{s}$. Shown above are for $\Delta z =$ (a) $1 \mu\text{m}$ (b) $5 \mu\text{m}$ (c) $10 \mu\text{m}$

Figure 4-6 shows the error associated with these filters. It is more important to make the curve fit well for the central frequencies (around zero) than for the frequencies further away from zero. The tolerance for error is determined by the eventual steady-state pulse width. Typically, for a gain bandwidth factor of $t_2 = 5 \times 10^{-13}s$, the steady-state pulse width is no less than $4ps$ (as seen in the rough analysis of the split-step method in Chapter 3). The frequency range that is necessary to cover more than 99.9% of the energy of a pulse with a $4ps$ width corresponds to only $1THz$. If the minimum pulse width were $3ps$, then about 99% of the pulse energy would lie within a $1THz$ bandwidth. For a $1ps$ pulse, it takes $3THz$ bandwidth to cover 99% of the energy, and so on. Since no pulse energy lies at these frequencies, the approximation is valid.

The implementation of a symmetric filter requires the knowledge of the pulse profile at the future time, $t + \Delta t$. Realistically, this value is not known, but an extremely good guess can be made. In the same manner that a future pulse profile would be calculated without the presence of the gain bandwidth factor, we can calculate the pulse at this time interval. Once the future value is known, the present (t), past ($t - \Delta t$) and future ($t + \Delta t$) values can be used to perform the filtering. The assumption made is that the filter only changes the pulse profile a little, so a guess of the future value that does not include gain bandwidth filtering can be used to calculate the effects of gain bandwidth filtering. This can be verified since for typical laser parameters (See Table 3.1) and a very large gain $g_p = 4000cm^{-1}$, the filter response falls a mere 2% of the peak value at $1THz$. For more reasonable gain values, $g_p = 2000cm^{-1}$, the filter drops less than 1% within a $1THz$ span, and it only improves as the gain drops. The shorter the time step (and thus, the space step), the better these approximations become.

It is important to note that Equation 4.33 shows the shape of the filter to be dependent on the peak gain, g_p , and hence, the carrier density, N . Therefore, each point along the laser cavity can experience a different filtering effect; the areas with higher carrier density will experience more filtering than areas with lower carrier density. An added benefit of this filter technique is that a variable filter of this kind can be implemented. In the split-step

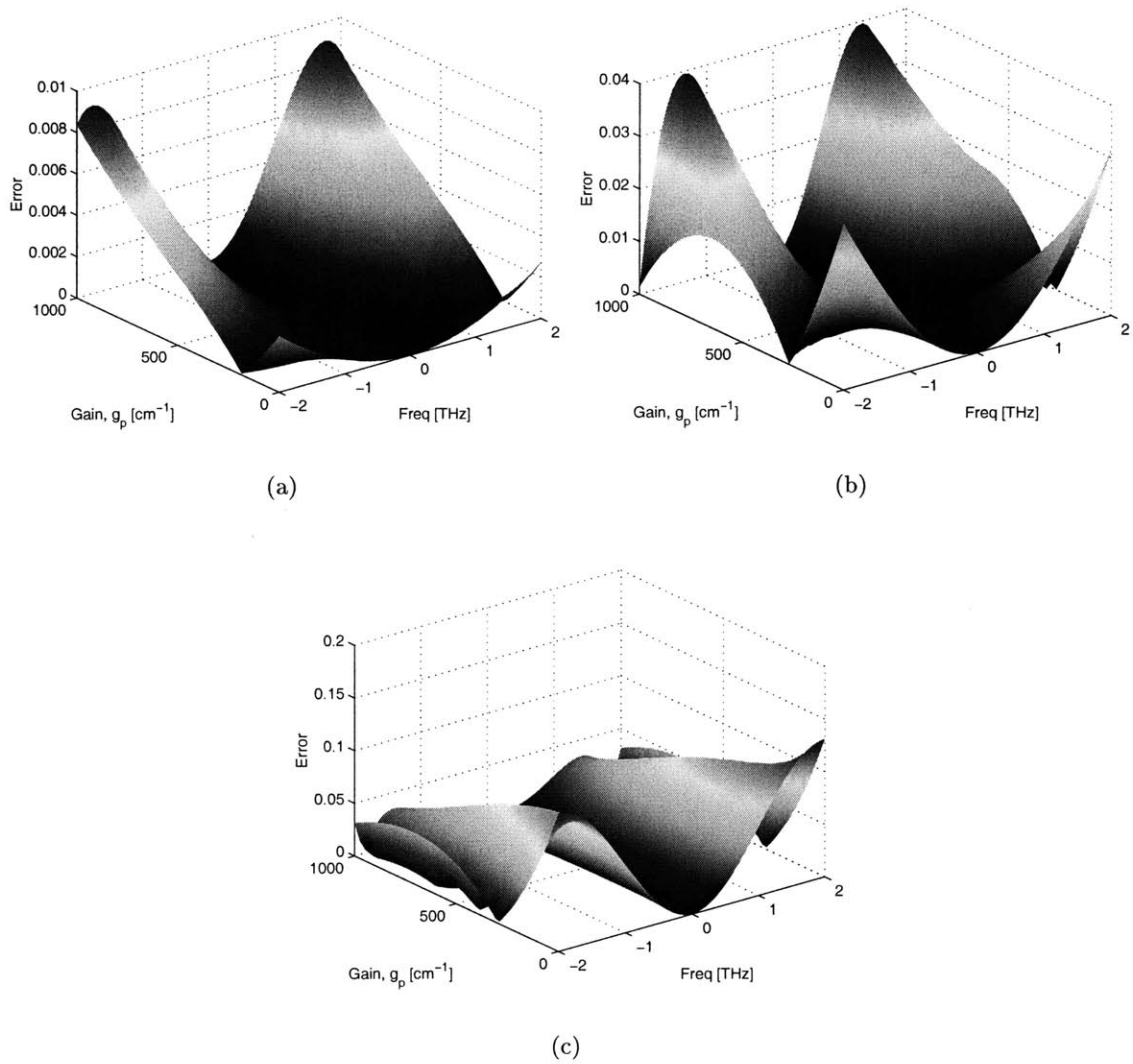


Figure 4-6: Error corresponding to the digital filter approximations defined by the parameters in Figure 4-5. Shown above are for $\Delta z =$ (a) $1\mu\text{m}$ (b) $5\mu\text{m}$ (c) $10\mu\text{m}$

method, this is not possible, since the filter is determined by the steady-state carrier density without photons.

It seems that this would require a filter fitting for each position in z at a given time t . This would then have to be repeated once the time increment was advanced, resulting in a very slow simulation, indeed! This can be bypassed by choosing all values *a priori* except for g_p and η . A separate program can be run that finds the best-fitting value of η for each given g_p . So, g_p can be scanned across a large range (i.e. from 0 to 5000cm^{-1}), and appropriate values of η can be found. Then, an n th-degree polynomial fit can be made to generalize a functional fit of the values of η to g_p . Hence, only the $n + 1$ coefficients are necessary to determine the appropriate η to use for a given g_p . This saves an immense amount of computational time. Figure 4-7 shows the fitted polynomial functions, $\eta(g_p)$, for various Δz . Appendix A shows the **Matlab** code for this concept.

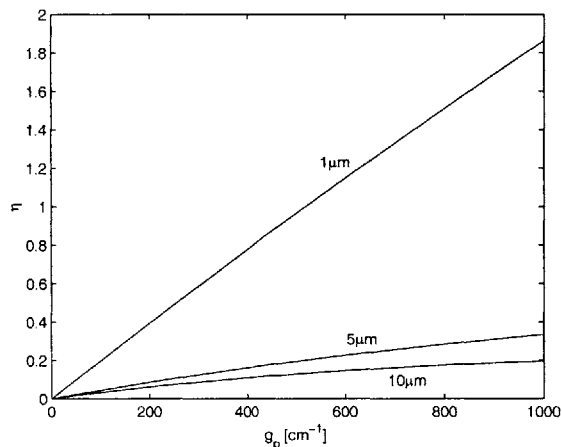


Figure 4-7: $\eta(g_p)$ for various $\Delta z = 1\mu m, 5\mu m, 10\mu m$.

After running simulations using this technique, it was found that when the value of η becomes equal to or greater than 0.5 then an unbounded error occurs, similar to that found for the second-order derivative approximation method in Section 4.5.2. A simple solution can be to limit η to values below 0.5. While this will result in a slightly understated filter

value, this is only necessary for regions where the carrier density reaches extremely large values. In a steady-state monolithic modelocked laser, the carrier density within the gain section should be close to transparency. In addition, it is possible to choose values of Δt that force η to be very small and, hence, never grow larger than 0.5.

4.7.2 Reverse-Bias Model

A strong benefit of using a finite difference simulation model over other models is the added ability to deal with saturable absorbers in an appropriate manner. The split-step method only allowed us to specify a power transmission coefficient and a saturation energy. The transmission coefficient signified the fraction of power that was transmitted through the absorber when it was saturated. The saturation energy (E_{sat}) is a measure of how much pulse energy is necessary to saturate the absorber. Although these quantities are possible to experimentally quantify, they are esoteric and have little relation to standard physical quantities, such as carrier lifetime and laser length. The finite difference model allows any model that can be described with a differential equation to be used for the reverse-biased laser section.

The model used in this thesis defines a saturable absorber simply as a laser section with a shorter carrier lifetime than a regular laser section. Typical lifetimes for a standard semiconductor laser section hover around $1ns$, depending on the carrier density, N . Equation 4.4 shows the carrier density dependency on the lifetime. As the carrier density approaches zero (equivalently, as the carrier density in the active region approaches thermal equilibrium with no bias), the lifetime becomes inversely proportional to A :

$$\tau_c = \frac{1}{A} \tag{4.34}$$

Hence, A can be used to define a traditional, low-level injection carrier density-independent lifetime value. For our simulations, we have chosen a value of $\tau_c = 10ns$ (hence, $A = 10^8 s^{-1}$). Since a regular laser section is biased above threshold, we will deal with high-level injection cases, where the value of A is unimportant.

We can use A to define the dramatically decreased carrier lifetime in a saturable absorber. Typical reverse bias carrier lifetimes range from 5 – 45ps, about three orders of magnitude less than that of a regular laser [31, 34, 35]. Karin et al. give a quantitative formula for determining the lifetime, based in experimentally-fit data.

$$\tau_c = 86ps \cdot \exp \left[-\frac{(V_{bias} + V_{bi})}{2.1V} \right] \quad (4.35)$$

where V_{bias} is the magnitude of reverse bias and V_{bi} is the built-in voltage of the device. The equation is a fit to a single 150Å *GaAs* quantum well with 720Å undoped $Al_{0.3}Ga_{0.7}As$ barriers. Karin et al. also describe in [60] a model that describes the physical effects that contribute to reduced lifetime performance in a reverse-biased laser segment. This thesis will use a value of $\tau_{sa} = 20ps$ for the saturable absorber carrier lifetime, unless otherwise noted.

Active Modulation Reverse Bias

The physics of reverse bias are also needed to describe actively modulated laser sections. The RF section is DC current biased with an RF power modulation superposed. For forward biased regimes, the RF power is translated into current modulation, hence a sinusoidal current is used for current values greater than zero. For reverse biased regimes, the laser diode is modeled in reverse bias, and the current is set to zero, while the carrier lifetime is reduced. We have chosen to use the same lifetime as that of the saturable absorber.

4.7.3 Computational Recipe

The **Matlab** code for the SSFD simulation can be found in Appendix A. A list of pertinent programs follow:

1. **findGBWFunc**. Determines the appropriate polynomial coefficients to describe a functional dependence of $g_p(N)$ versus η .
2. **LaserParam**. Loads all general laser parameters.

3. `fdiffMain`. Loads specific modelocked laser parameters, such as laser geometry, biasing, and RF frequency. Sets up initial conditions, such as seed pulse, and carrier density within the laser. Executes `fdiffLoop`.
4. `fdiffLoop`. This is the main loop of the program. It calculates the new state variables for each time/space increment and graphs the progression. It also collects the output laser power coming off the right-hand laser facet.
5. `plotRT`. Calculates pulse width and total pulse energy for each round trip. Plots snapshots of the pulse energy within the cavity, the power emitted from the cavity, and the pulse width and energy. Each snapshot is separated in time by the inverse of the frequency of the active modulation.
6. `plotEP`. For use with detuning experiments. Displays the pulse evolution and determines if the pulse is locked to the RF source.

The following section will describe the computational recipe to the reader in a step-by-step manner.

1. Define all laser parameters.
2. Choose an appropriate space increment (Δz).
3. Build the appropriate filtering function, based on the space increment choice.
4. Define all modelocked laser geometries and bias points, including RF modulation depth and frequency.
5. Define all laser initial conditions for N and S^\pm . Seed the photon density with an arbitrarily shaped pulse of any energy.
6. Repeat the following loop that calculates all pertinent data at each time increment.
 - (a) Calculate the RF current bias for this particular time step.

- (b) Calculate the next pulse, without filtering.
- (c) Calculate the next-next pulse, without filtering.
- (d) Based on the current gain, calculate the appropriate filter and apply to the next pulse.
- (e) Calculate the next carrier density.

4.7.4 Simulation Validity

As in the split-step discussion, we undergo the same testing to verify the accuracy of the SSFD method. Many of the following tests are similar to the ones found in Section 3.4.2. However, because the SSFD method is more physical, the tests will have a more tangible feel.

When the space increment shrinks, the finite difference algorithm becomes more accurate and the filter error shrinks (See Figure 4-6). However, the η parameter needed to describe the same bandwidth limiting factor (t_2) grows. As we decrease the space increment we should observe the accuracy of the simulation increase. Figure 4-8 compares the steady-state pulse width and energy for different space increments. In this simulation, $L_{sa} = 60\mu m$, $\tau_{sa} = 20ps$, $A = 10^8 s^{-1}$, $I_{gain} = 100mA$, $I_{act}^{DC} = 20mA$, $I_{act}^{RF} = 40mA$.

Note that for $\Delta z = 13\mu m$, the steady-state does not follow the asymptotic trend of the smaller increments. It is easy to see that smaller space increments show increasingly diminished accuracy improvements in the pulse width. The pulse energy follows a more damped oscillation behavior that approaches a singular value, rather than a monotonic trend. It is unsure why the energy follows this trend. Therefore, it is sensible to choose an increment that satisfies an acceptable level of accuracy while not prohibitively increasing the computation time to reach a steady-state. For all subsequent tests, we choose a space increment of

$$\Delta z = 5\mu m \tag{4.36}$$

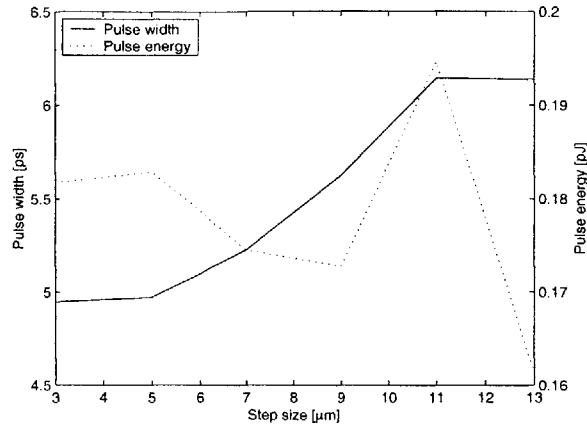


Figure 4-8: Steady-state pulse width and energy for different space increments.

The next few tests demonstrate the steady-state's invariance to initial conditions. Figure 4-9 varies the initial pulse width, using an initial peak power of 0.1mW . Initial pulse widths shown are 20ps , 5ps , 1ps , and 0.1ps . The graph does not show these values explicitly, since the initial pulse lies within the laser cavity (internal). The graph only shows data extracted from the laser output (external). Figure 4-10 varies the initial pulse energy, using an initial pulse width of 1ps . Initial pulse energies shown are $1.5 \times 10^{-22}\text{J}$, $1.5 \times 10^{-16}\text{J}$, and $1.5 \times 10^{-11}\text{J}$. Additional simulations show that the steady-state can be reached from a singularity initial condition of arbitrary energy. For all subsequent simulations, we start with a low, spatially-uniform photon density. This also reaches an identical steady-state as the other arbitrary initial conditions. Figure 4-11 varies the initial pulse location, relative to the active modulation peak. It shows how the pulse steady-state settles to the same time distance away from the modulation peak. Figure 4-11 represents the output of the mod-locked laser from the right-hand side (RF modulation side). Rather than show a single, long stream of photon power, each round-trip period is shown side-by-side. The photon density is shown by color; darkest is densest. Time evolves by following a vertical line from bottom to top, then shifting over to the right by one round trip and scan once more from the bottom. The time window length of the graph represents one round-trip period. A

round-trip period is defined, not by the round-trip time of the pulse bouncing in the cavity, but by the inverse of the frequency of the RF modulation, since this force more accurately determines the laser's output round-trip time.

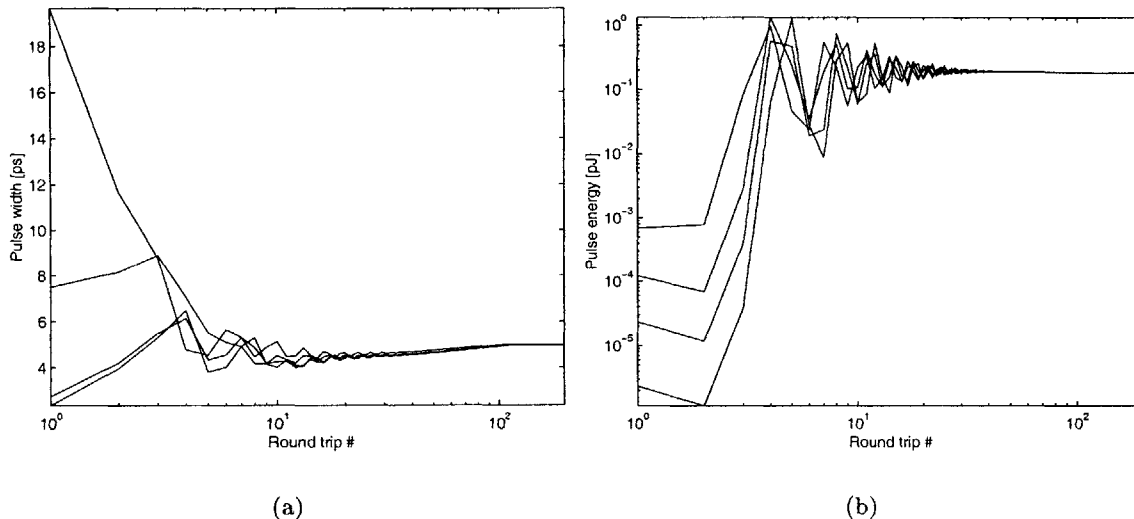


Figure 4-9: Steady-state (a) pulse width and (b) pulse energy for different initial pulse widths.

We can demonstrate the active section's ability to synchronize the pulse's frequency to its own. Figure 4-12 shows the laser's output without RF modulation. For comparison, Figure 4-11 are all examples with RF modulation.

4.8 Design Trends

The SSFD method can be used to determine design trends for better performance, more efficient semiconductor modelocked lasers. It can also shed light on biasing trends that optimizes performance of the lasers. This section provides a compilation of these trends.

The three-section monolithic laser introduced in Chapter 3 was not experimentally successfully modelocked. The major cause was the presence of large internal reflections occurring at the current-confining etch regions between the three sections. Dimensions of the

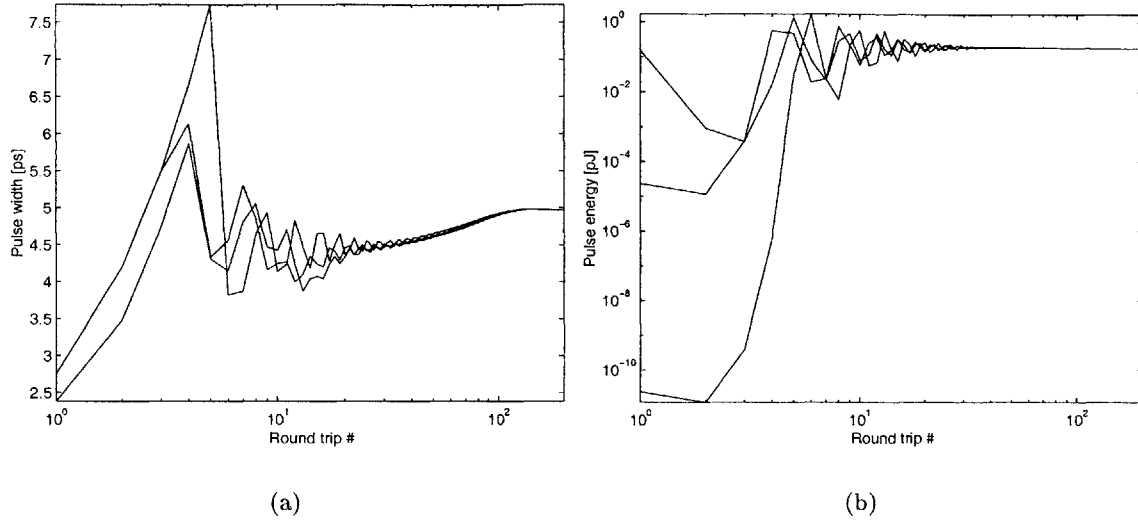
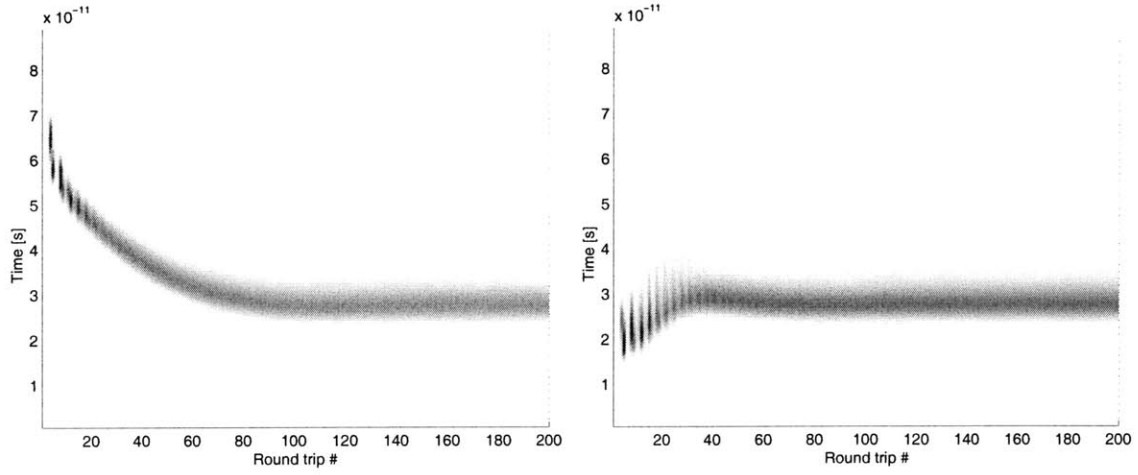


Figure 4-10: Steady-state (a) pulse width and (b) pulse energy for different initial pulse energies.

three sections are: $230\mu m$, $3400\mu m$, $240\mu m$. Figure 4-13 shows the DC L-I characteristics of the laser. The ordinate is the current bias on the large section while each curve represents different biases on the small sections. The small sections were biased equally with respect to each other.

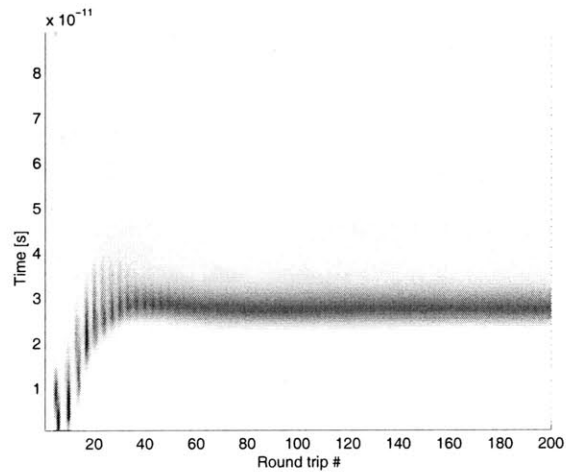
Figure 4-14 shows evidence of significant reflections occurring at the current isolation boundaries. The resonant peaks correspond to a round-trip cavity length of about $230\mu m$, which is roughly the length of each small section. This implies that a resonant cavity is formed by internal reflections at the section boundaries.

Within the time span of the writing/research for this thesis, a suitable test device was unavailable. Hence, we look to results presented in the literature to explore the design capabilities of the SSFD simulation. We use a high-performance two-section $1.55\mu m$ monolithic hybrid modelocked laser developed by Ogawa et al. [29]. In addition to [37, 38], we can determine the majority of the laser parameters, compiled in Table 4.2. The listed values are nominal values and will change when noted.



(a)

(b)



(c)

Figure 4-11: Pulse evolution to steady-state for two different initial relative pulse locations.

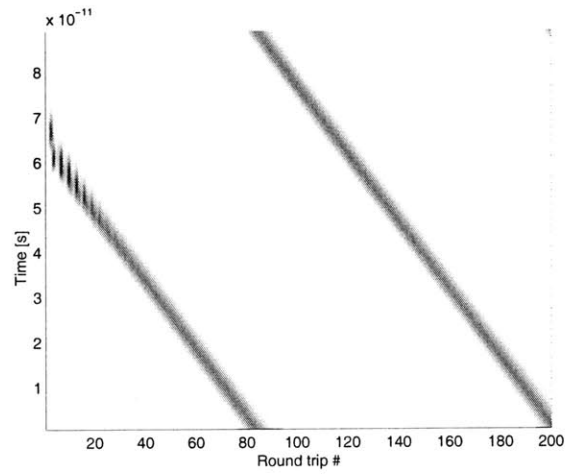


Figure 4-12: Laser output with $I_{act}^{RF} = 0$. The pulse continues to advance in time faster than the group velocity.

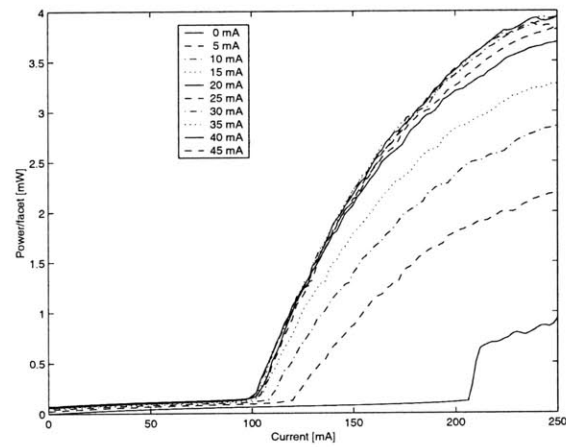


Figure 4-13: DC L-I curves for three-section laser.

Table 4.2: Laser Parameters

Parameter	Symbol	Value	Unit
Intrinsic			
Carrier wavelength	λ_0	1.55	μm
Effective group index	n_g	3.7	
Facet power reflectivity (sat. abs. side)	R_{sa}	0.274	
Internal power reflectivity	R_{int}	0	
Confinement factor	Γ	0.05	
Gain coefficient	g_0	3420.8	cm^{-1}
Transparency	N_{tr}	1.577×10^{18}	cm^{-3}
	N_s	2.254×10^{18}	cm^{-3}
Internal quantum efficiency	η_i	1	
Internal optical loss	α_i	5	cm^{-1}
Trap recombination coefficient	A	1×10^8	s^{-1}
Bimolecular recombination coefficient	B	1×10^{-10}	$cm^3 s^{-1}$
Auger recombination coefficient	C	1×10^{-28}	$cm^6 s^{-1}$
Gain bandwidth factor	t_2	5×10^{-13}	s
Geometry			
Quantum well thickness	T_{QW}	40	\AA
Number of quantum wells	N_{QW}	3	
Ridge width	W	2	μm
Length of saturable absorber	L_{sa}	75	μm
Length of active section	L_{act}	750	μm
Length of phase control sect.	L_{pc}	150	μm
Length of DBR	L_{DBR}	200	μm
Coupling coefficient	κ	20	cm^{-1}
Effective length of DBR	L_{eff}	95	μm
Effective power reflectivity (DBR side)	R_{DBR}	0.43	
Discrete space step	Δz	5	μm
Biasing			
Saturable absorber lifetime	τ_{sa}	5	ps
Current, RF, act. sect.	I_{RF}	60	mA
Current, DC, gain sect.	I_{gain}	60	mA
Frequency detuning	f_{det}	0	MHz

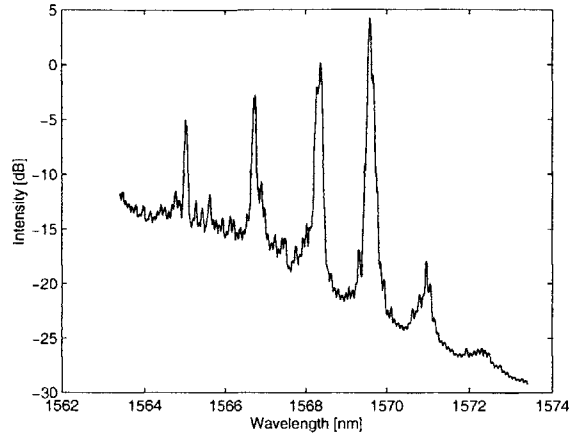


Figure 4-14: Optical spectrum of three-section laser.

The device, shown in Figure 4-15, consists of an actively-modulated saturable absorber section, a DC-biased gain section, and a passive waveguide section. The saturable absorber is a reverse-biased laser diode with the addition of an RF source for active modulation. The RF input power is modeled as a sinusoidal current modulation. Transmission line reflectance and internal laser diode impedance can be used to calculate the amount of power needed to achieve the desired RF strength. Hence, the passive waveguide section was grown at $1.3\mu\text{m}$, making the bandgap energy larger than the photon energy. The photon field is roughly transparent to the bandgap, however optical loss (α_i) due to heavy-hole/light-hole intervalence band absorption. This section is unbiased. Due to the mismatched material between the passive waveguide and gain section, there is a finite reflectivity associated with fields traveling across this interface; this is ignored in the simulation ($R_{int} = 0$). However, it is shown in the following sections that modelocking can occur even with non-zero internal reflectivity.

The saturable absorber side is terminated by air, and a straight-forward index-mismatch power reflectivity is calculated for R_{left} . The passive section consists of phase control section

and a DBR (Distributed Bragg Reflector) grating. The phase control section is not used in this simulation. We use the effective mirror approximation to derive an effective cavity length (L_{eff}) and reflectivity (R_{DBR}) for the DBR. Using κ , λ_0 and L_{DBR} , we determine this using a transmission matrix solver.

The confinement factor is approximated to 5%. Although the confinement factor is not found in the published works of this group, it can be calculated by knowing the band structure, found in [37], using an optical mode solving program. The gain versus carrier density parameters, g_0 , N_{tr} , and N_s are fitted parameters to the theoretical gain curves in Section 2.4.5. The internal quantum efficiency, η_i , is set to 1, since a different value will only scale the current inputs.

The saturable absorber is reversed biased, and is modeled with an increased carrier lifetime, τ_{sa} , which causes any generated carriers to be swept away by the reversed biasing. The value of τ_{sa} is a monotonically increasing function of increasing reverse bias voltage, but the relationship is non-trivial to determine but can be accomplished experimentally (See Section 4.7.2).

The gain bandwidth factor, t_2 , is assumed to be the same as the previous lasers in this thesis. The ridge width is not mentioned in the three papers, and a value is set to $2\mu m$. This will scale currents, total field energies, and also the confinement factor.

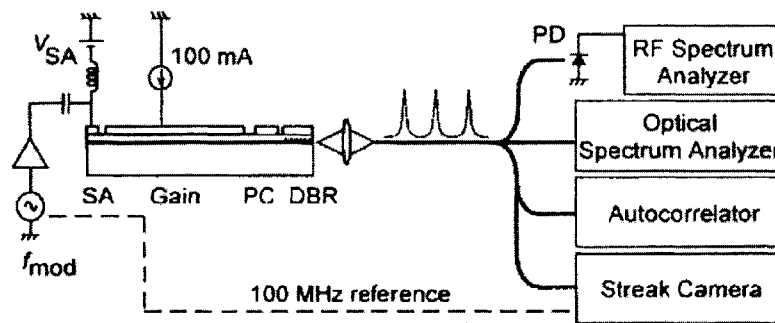


Figure 4-15: Schematic of laser used for design [29].

We now present, in the following sections, results from the simulation for various pa-

parameter spaces. For each experiment, we scan two parameters and measure the steady-state pulse width and energy for each point in the parameter space. In general, the goal is to minimize the pulse width and maximize the pulse energy. The three following sections are broken down into three parameter space themes: biasing parameters, geometrical parameters, and intrinsic laser parameters.

4.8.1 Biasing

Passive Modelocking

It is necessary to demonstrate simple passive modelocking, since the hybrid case should follow similar biasing schemes. The active modulation should only serve to modulate the time-dependent gain and should not affect the overall performance of the laser, other than providing a confining potential to make the pulse more robust against noise. Certain kinds of noise, such as spontaneous emission noise, will serve to produce fluctuations in the periodicity of the pulses; effectively shifting the pulse backward or forward in time. The active modulation should only provide a time-dependent gain potential that synchronizes the pulse to the electrical modulation source frequency.

In Figure 4-16, the gain section current bias is scanned for different saturable absorber lengths. Each curve represents a distinct saturable absorber length. Each curve is terminated by a lower and upper bound for DC bias. The lower bound is set by the minimum gain needed to exceed threshold. The upper bound denotes CW or modulated CW operation. The pulse energy trends are intuitive: with increasing bias, the pulse energy increases. In addition, for a given bias level, the energy falls as the saturable absorber length increases, accounting for increased pulse absorption.

The pulse width trend is a bit more interesting. For small currents (hence, small pulse energies), the pulse width falls with increasing bias. Around $150mA$, the pulse width hits a minimum and then increases slightly with increasing bias. This is accounted for by the fact that for small pulse energies, the pulse is not completely saturating the absorber (this was observed by examining the carrier density dynamics in the simulation). Hence, as the

pulse energy increases, the absorption saturation is more strongly observed, resulting in a narrower pulse. Again, the concept of a saturation energy, E_{sat} is introduced. This is the energy that is needed to saturate the absorber, and is proportional to the transverse cross-sectional area of the absorber and the strength of reverse bias. It is not proportional to the length of the absorber. It can be increased only by harder reverse biasing on the absorber.

When the pulse initially enters the absorber, it experiences the greatest amount of pulse shaping since its energy is large and is on the order of E_{sat} . As the pulse travels further into the absorber, its overall energy is reduced and pulse narrowing is reduced. The further the pulse travels into the absorber, the less narrowing effect the absorber will have on it. However, the pulse will still continue to experience pulse energy reduction. Thus, the use of very long absorbers is not necessarily beneficial. Of course, increasing the bias raises the initial energy of the pulse entering into the absorber, but not without increasing the filtering due to decreased gain bandwidth. In addition, the increased gain saturation effects begin to widen the pulse.

A transparency energy E_{tr} can be defined for the gain section, describing the energy necessary to bring the gain region to transparency. With increasing current bias, the carrier density increases and, hence, E_{tr} increases. Since the steady-state pulse energy increases simultaneously, the pulse sees a larger gain saturate effect and the pulse becomes slightly wider.

Heating effects are not included in this model. Therefore, a fundamental limit on the maximum current bias and pulse energy needs to be imposed on the results of the simulation. This fact should be kept in mind when interpreting the results of the simulation. In summary, these results claim that an optimum absorber length can be determined. All subsequent simulation results include active modulation.

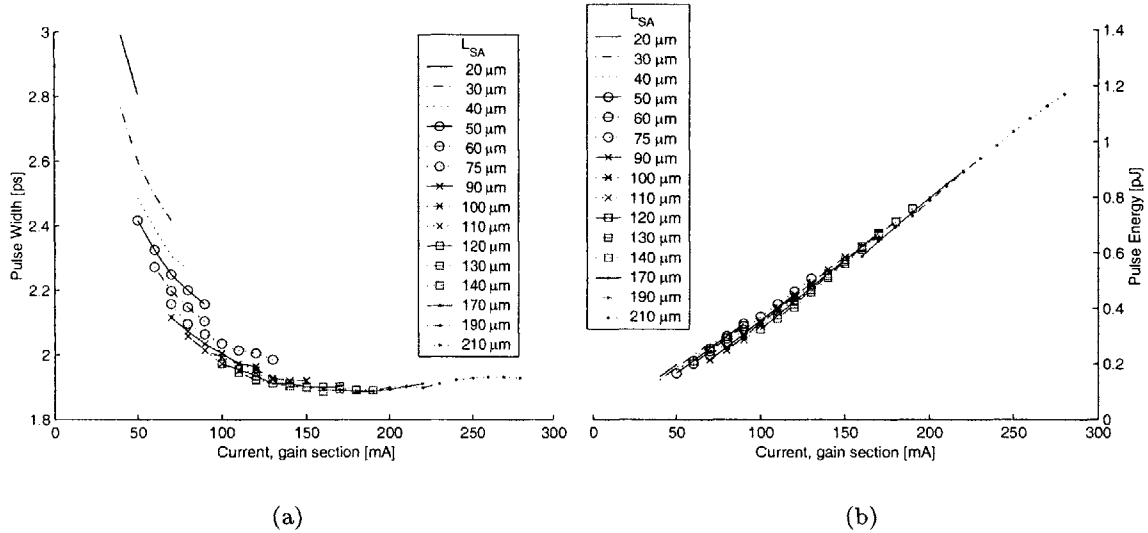


Figure 4-16: (a) Pulse width and (b) pulse energy versus gain region bias current, for different saturable absorber lengths (no active modulation).

RF Current Depth

The following simulation experiment involves scanning the magnitude RF current for different DC current biases. Figure 4-17 shows the simulation results. For each DC bias level curve, the smallest RF current point shown defines the minimum modulation depth required to produce synchronized, well-defined steady-state pulse trains (i.e. poor modelocking was observed for RF depths of 30mA or less). There is no upper bound, however; 80mA was chosen arbitrarily as a cut-off point for the simulation.

Note that no frequency detuning was used (this will be elaborated on in the next subsection). Note also that the modulation current densities are extremely high for a reverse-biased laser section. For example, $\pm 50\text{mA}$ for a $75\mu\text{m}$ long, $2\mu\text{m}$ wide saturable absorber gives a current density of $J_{RF} = 33\text{kA}/\text{cm}^2$. However, with no detuning, these levels are necessary to produce well-defined pulses that are synchronized to the RF source. Note also the saddle point seen by looking at the pulse widths for a fixed RF current, scanning the DC currents.

We see that $I_{gain} = 60mA$ gives the smallest pulse width, with current levels on either side producing wider pulses. This was also seen in the passive modelocking case above. Note that the widths increase with increasing RF currents. This is due to the fact that greater RF currents produce a higher average carrier density in the absorber, which results in less absorption saturation effects.

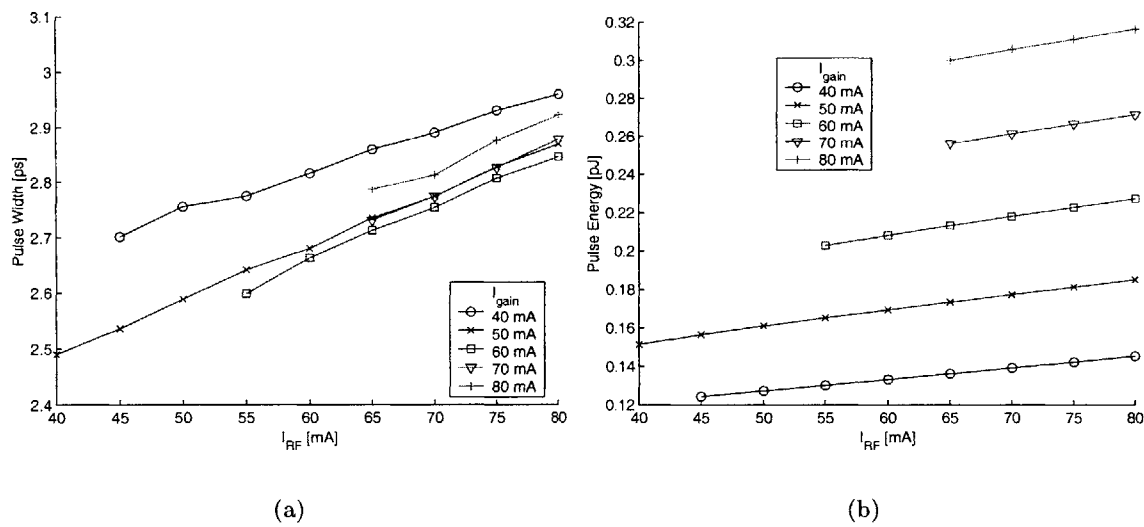


Figure 4-17: (a) Pulse width and (b) pulse energy versus gain region bias current, for different modulation depths.

Frequency Detuning

The modulation frequency can be detuned from the nominal value defined by twice the laser length divided by the pulse group velocity. The range of detuning frequencies that produce synchronized, well-defined pulses is defined as the locking bandwidth. Locking bandwidth curves for different modulation depths are shown, demonstrating the effect of modulation depth on the locking bandwidth range. It is expected that this bandwidth would decrease with decreasing modulation depth, since the confining potential is less.

Figure 4-18 shows a rough, broadband picture of the widths and energies within the locking bandwidth range. Neither the 80mA nor 40mA RF modulation depths shown were the actual max/min values. These were chosen arbitrarily (i.e. 90mA or 30mA would also produce curves). In addition, the locking bandwidths for 70 and 80mA extend beyond the arbitrarily-chosen frequency range of $\pm 500\text{MHz}$.

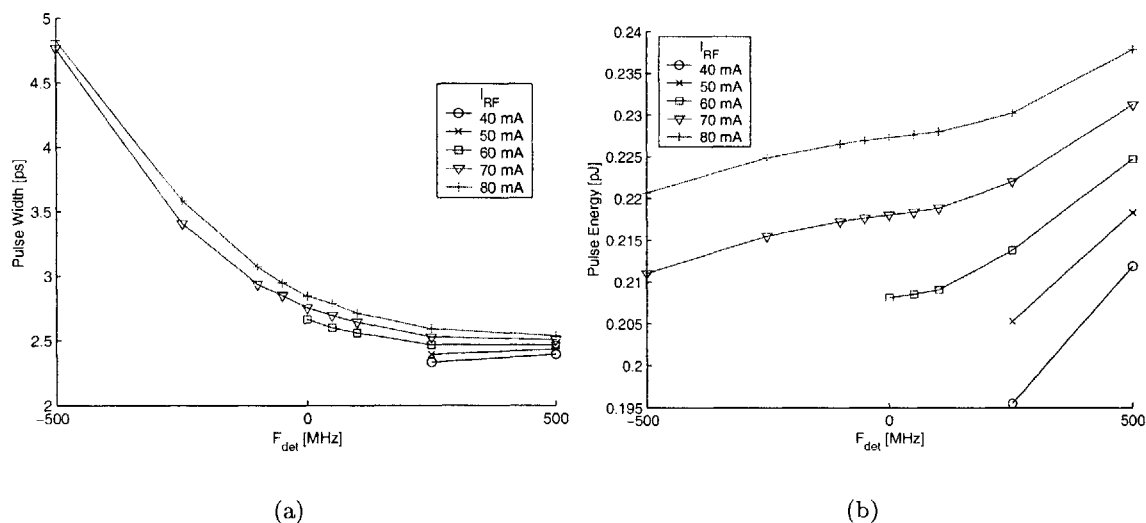


Figure 4-18: (a) Pulse width and (b) pulse energy versus detuning frequency, for different modulation depths.

Figure 4-19 shows a more detailed and extended picture of the locking range. We can feasibly make the RF current very close to zero and still achieve a non-zero locking range.

The most notable point is to notice that the range for pulse synchronization occurs well away from 0MHz . The locking range should lie where the modulation is as close to the true round trip frequency of the oscillating pulse. This phenomenon occurs due to the unbalanced pulse drifting caused by gain and loss saturation (discussed in Section 3.3.1). The amount of pulse drifting in steady-state determines how much detuning is necessary. In addition, the more drifting the less chance that 0MHz detuning will be able to produce synchronized, well-defined pulses, since the pulse will experience a greater urge to break the

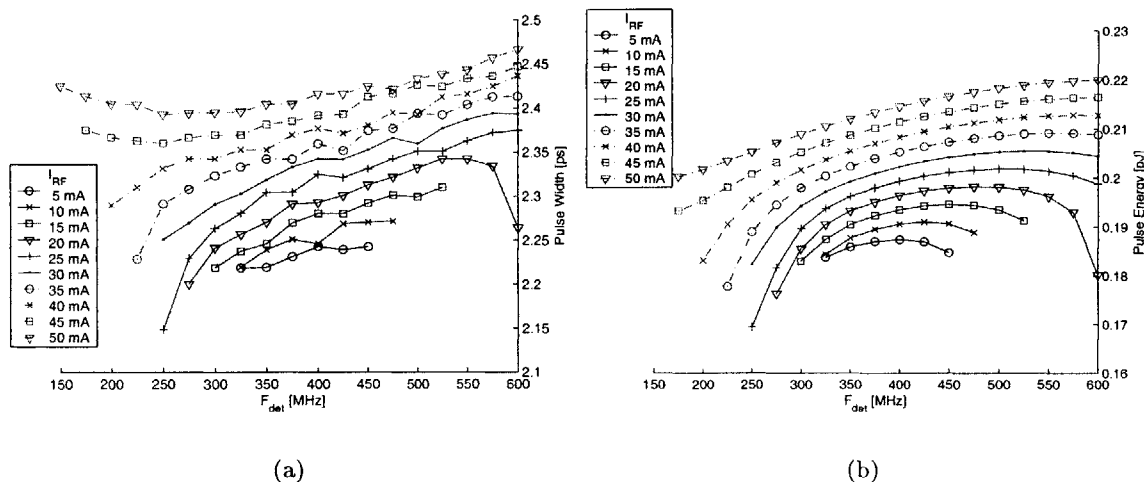


Figure 4-19: (a) Pulse width and (b) pulse energy versus detuning frequency, for different modulation depths. A more detailed view than Figure 4-18.

synchronizing RF potential. By detuning, smaller RF currents can be used. Practically, in a real modelocking experiment, the true group velocity is not accurately known. An error in group index of ± 0.1 results in a difference of $1GHz$ modulation frequency, much greater than the shifted detuning range determined here (only about $400MHz$). Hence, an experimenter would most likely find the "detuned" range without realizing that this was actually detuned. She would merely find the frequency that gives the optimum modelocking performance. This point should correspond to the pulse passing through the RF section near the peak of the modulated carrier density. Detuning the frequency from this true round trip frequency, either greater or less than this peak value, would cause the pulse to experience lower gain and therefore smaller pulse energies would be observed. In addition, shorter pulse widths would also be observed, since the pulse feels a steeper confining potential.

However, in a simulation, finding this range is not as trivial a task. For each point in a parameter space, the detuning must be scanned to find a locking range that could span less than $50MHz$, but lie $400MHz$ away from the nominal value of $0MHz$. Since most parameter changes will affect the amount of gain/loss saturation found in a steady-

state round-trip, the amount of net drift per round trip will change greatly. Therefore, the locking range should shift with each parameter change, potentially making computation extremely time-consuming. A simple algorithm may be feasible to construct that allows for a minimization of detuning scanning. This is left to future work. In addition, it is interesting to note that the less DC current bias on the gain section, the less pulse drifting occurs (pushing the pulse faster in time), and the greater the locking bandwidth will be.

For all subsequent simulation experiments, we do not attempt to find the locking range. Rather, we set the detuning frequency to $0MHz$ and find a robust RF modulation depth that gives us suitable modelocking. We have chosen $I_{RF} = 60mA$. This value is too high for experimental purposes but should allow us to observe the trends regardless. It is stressed that an accurate solution, with a lower modulated carrier density, is straightforward to simulate, however it is not performed in this thesis.

Reverse Bias Strength

As stated before, making the reverse-bias voltage more negative produces a decreased carrier lifetime, τ_{sa} . Figure 4-20 shows different carrier lifetime curves. A curve for $\tau_{sa} = 2ps$ is not shown, indicating no suitable, stable steady-state was reached. $I_{gain} = 40mA$ marks the minimum current bias for stable pulses, however $I_{gain} = 80mA$ does not represent the maximum. Most trends are intuitive. Decreasing the lifetime decreases the pulse energy and width. However, for increasing DC bias, the pulse width increases for $\tau_{sa} = 100ps$ but decreases for $\tau_{sa} = 5ps$. This can be explained using the concept of E_{sat} . For larger lifetimes, the steady-state carrier density is larger, therefore it is easier to saturate the absorber. For the bias values shown, the absorber has been easily saturated for the $\tau_{sa} = 100ps$ curve. However, this is not the case for the $\tau_{sa} = 5ps$ curve, where the pulse energy has not yet saturated the absorber during each round trip. In this curve, the increasing bias produces a higher-energy pulse that begins to saturate the absorber more effectively, producing shorter pulses.

In summary, if the saturable absorber is made too long, then the gain necessary to

achieve a steady-state pulse must be made higher, or the net round trip gain/loss will be too high and the pulse will never appear. Heating effects and other non-idealities prevent the gain from being too high. If the saturable absorber is too short, however, the pulse is not exposed to a very large pulse narrowing force. Hence, the steady-state pulse will be very broad. Reverse biasing the absorber harder or making it longer do not have the same effects. As stated in the above sections, increasing the length increases the pulse narrowing effects while increasing the reverse bias increases the E_{sat} . Both serve to increase the DC threshold current bias. If the pulse energy is much less than E_{sat} then not much pulse narrowing occurs. If the pulse energy rises well above E_{sat} then the pulse narrowing effects cease to increase.

It is reiterated that this minima is set by E_{sat} and the pulse energy. The former is not a function of absorber length, L_{sa} , as can be seen clearly in the 30GHz case.

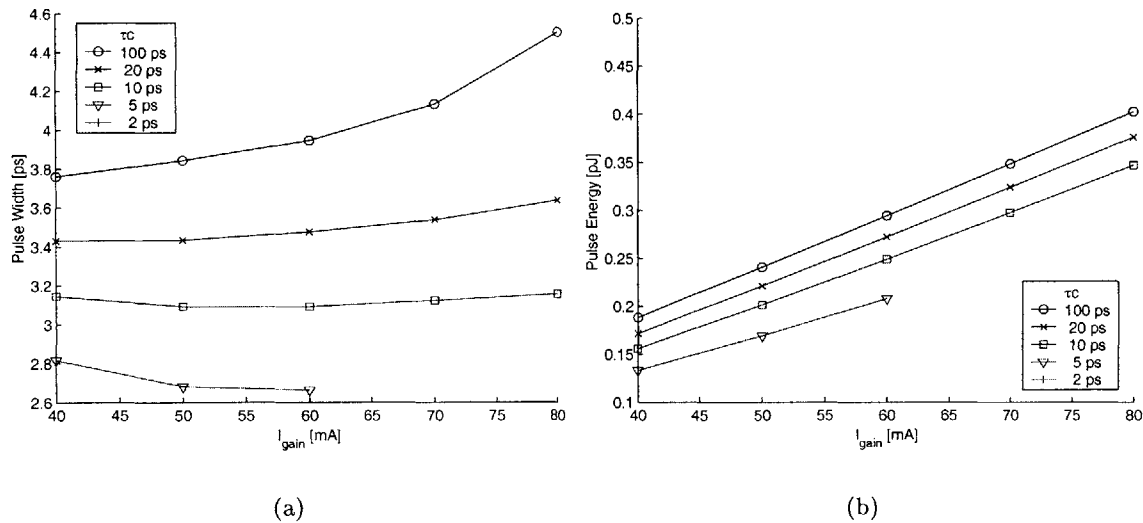


Figure 4-20: (a) Pulse width and (b) pulse energy versus gain region bias current, for different saturable absorber strengths (measured by carrier lifetime).

4.8.2 Geometry

Round-trip Frequency

This section explores the differences between cavities of different lengths. There are three lengths presented, corresponding to three different round trip frequencies: $38GHz$, $30GHz$, and $20GHz$. Figures 4-21 to 4-23 show the results of these simulations. Each simulation scans the DC bias for different saturable absorber lengths. In order to maintain the same total cavity length, the gain section length is changed. In other words, as the saturable absorber length increases, the gain section length decreases. Also, the RF current density is maintained at $40kA/cm^2$ to maintain consistency. Evident in the $30GHz$ case, there is a relatively small range of DC biases that result in stable pulses. The lower limit was set by the minimum bias required to be above threshold. As the saturable absorber length increases, this DC bias threshold level also increases. The upper limit was set by an increase of pulse drift which prevented the pulses from synchronizing. Again, pulse width minima can be seen, similar in effect to the passive modelocking case. In the $20GHz$ case, pulse broadening for large biases is evident when $L_{sa} = 400\mu m$.

4.8.3 Intrinsic

Optical Loss

Not all parameters can be so easily controlled as the biasing or laser geometry. However, we can explore the effect of improving them to see how they affect laser performance. If they prove to be of large impact, then these facts can be relayed to the laser designer and grower to ensure these parameters are optimized. The optical loss parameter, α_i , is one such parameter. Figure 4-24 shows the effects of controlling the optical loss. Each curve is lower-bound by the threshold condition and upper-bound by increased pulse drift. In steady-state, the net gain and loss per round trip must equal unity. The effect of reducing α_i means that the overall round trip loss is reduced, hence the gain need not be as large to maintain a net round trip gain/loss of unity. Since the gain is lower, the gain saturation effects and gain

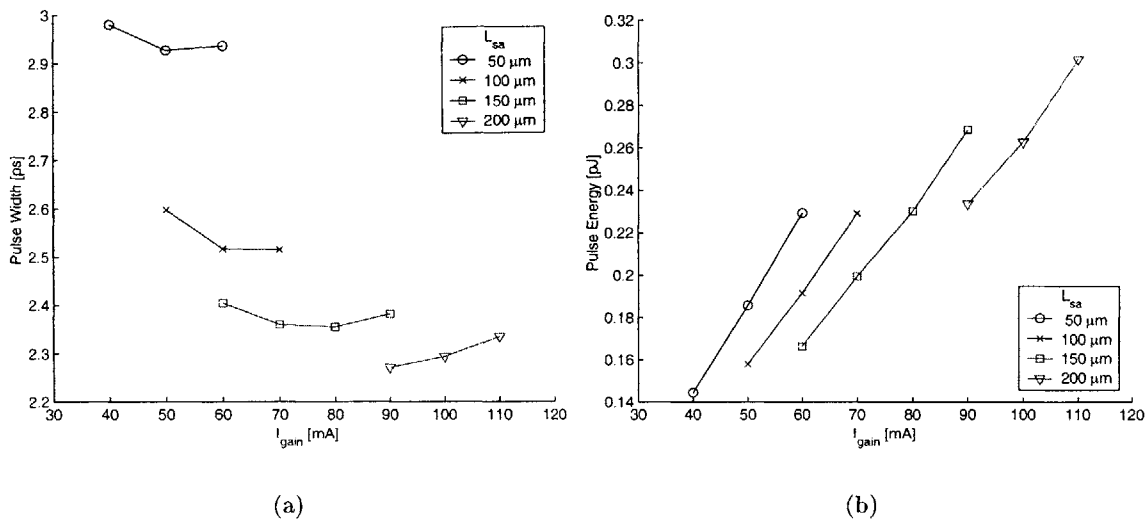


Figure 4-21: (a) Pulse width and (b) pulse energy versus gain region bias current, for different saturable absorber lengths in a 37.8 GHz cavity.

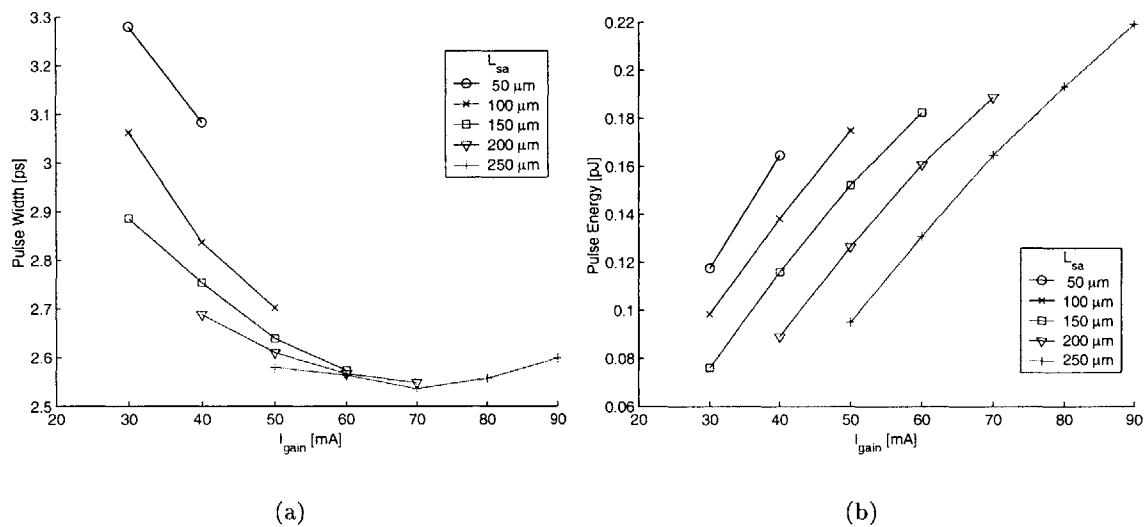


Figure 4-22: (a) Pulse width and (b) pulse energy versus gain region bias current, for different saturable absorber lengths in a 30 GHz cavity.

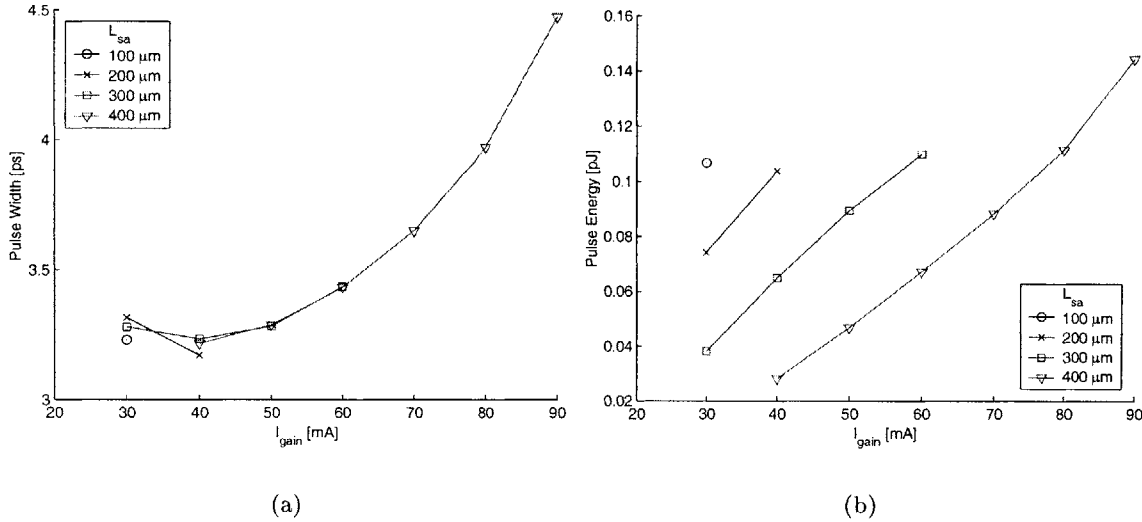


Figure 4-23: (a) Pulse width and (b) pulse energy versus gain region bias current, for different saturable absorber lengths in a 20 GHz cavity.

bandwidth filtering are not as strong, so pulse broadening is minimized. These factors result in lower pulse width and higher pulse energy: both wins in laser performance optimization.

Facet Reflectivity

A more controllable parameter (albeit not technically an intrinsic parameter) is the mirror facet reflectivity. Although it can nominally be controlled by changing the index of the material, it is most easily controlled by depositing an HR coating on the end facets. Figure 4-25 scans the DC gain for different mirror reflectivities for the left-hand mirror (in Figure 4-15). As with all the simulations, the optical power is collected from the right-hand facet. Intuitively, the laser output should increase as the mirror reflectivity increases. Additionally, the internal photon energy should be higher, due to a greater confining force. The net round trip gain/loss is reduced, therefore requiring less gain to obtain an above-threshold pulse. As similarly seen in the reduction of optical loss, the increase of mirror reflectivity results in reduced pulse width and increased pulse energy. This is also a win/win situation,

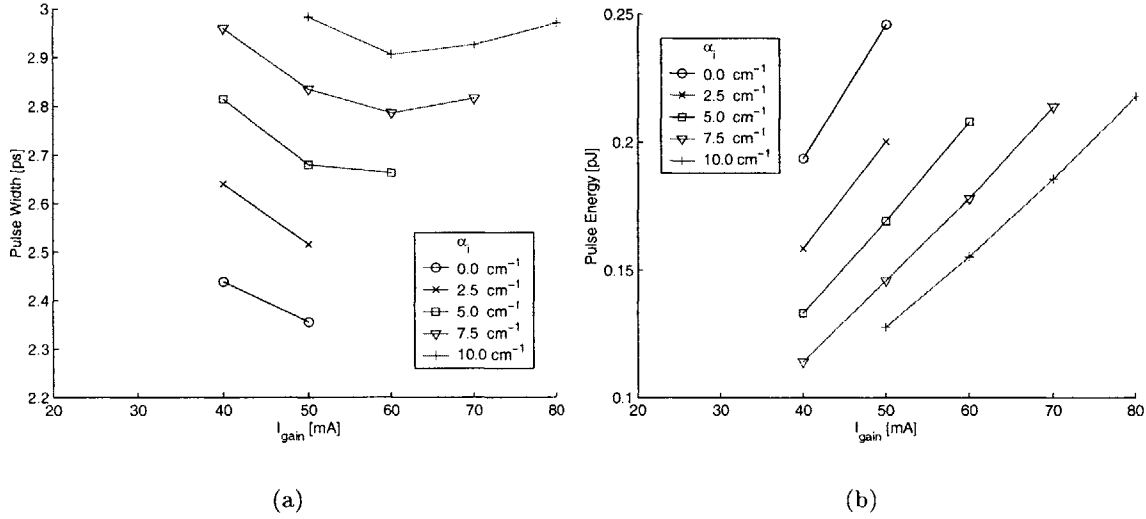


Figure 4-24: (a) Pulse width and (b) pulse energy versus gain region bias current, for different optical loss values.

and much more easily controllable than the former parameter.

Internal Reflections

The presence of non-zero internal reflections (so-called "coupled-cavity" cases) can also be simulated. In Figure 4-26, we create reflective boundary conditions at the current-confining boundaries. There are two: one between the absorber and gain section, one between the gain and DBR section. Each curve represents changing their reflectivities simultaneously. As can be seen, the transition between $R_{\text{int}} = 0.01$ and $R_{\text{int}} = 0.1$ results in a dramatic increase in the pulse width. The pulse widths shown that lie above 10ps do not actually represent pulses. The round trip cavity length is only 26ps long; to have a FWHM pulse width of anything greater than 10ps would mean an overlapping of the tails of neighboring pulses. In fact, their nulls do not fall to zero. Rather, they represent either CW light or modulated CW light, essentially showing no modelocking. In summary, it is necessary to

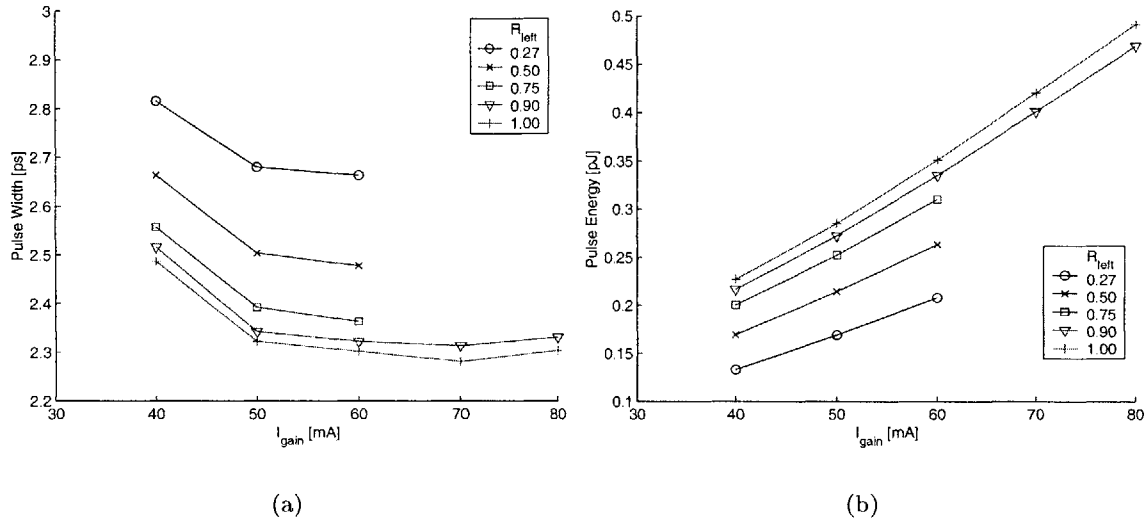


Figure 4-25: (a) Pulse width and (b) pulse energy versus gain region bias current, for different left-hand-side mirror reflectivities.

keep the internal reflections quite low.

4.9 Summary

The SSFD method has been developed through the inspiration provided by the published literature. Like other methods, it harbors its own limitations. However, primarily due to the development of faster computers, the SSFD method is, at heart, a brute-force finite difference method enhanced by a filter technique capable of describing second-order effects that a traditional finite difference method cannot. The method is computationally intensive, but with the progressive advancement of the computational power of inexpensive desktop computers, this has ceased to be a large concern. The filtering has limitations that are mathematical in origin, and a study on numerical methods would possibly allow a relaxation of these limitations. However, for a large range of experimentally-observed gain bandwidth parameters, this method is a robust and useful tool for describing modelocked

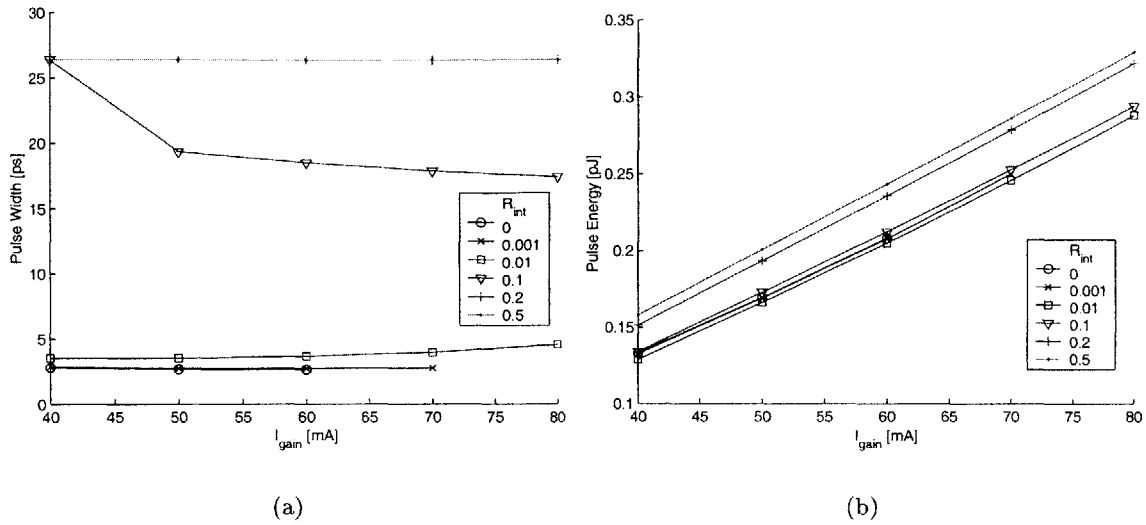


Figure 4-26: (a) Pulse width and (b) pulse energy versus gain region bias current, for different internal reflections.

laser dynamics. It is capable of exhibiting many effects due to its general description of the laser dynamics. Its greatest strength lies in its usefulness as a design tool for optimizing the performance of modelocked lasers. This ability has been demonstrated in the various simulation results that lie in this chapter.

Chapter 5

Conclusion

5.1 Summary

This thesis begins with theoretical and experimental parameter extraction for general laser diodes. All parameters necessary for describing the lasers used in the simulation programs can be determined and verified against results from multiple tests. The extractable parameters include: optical loss parameter, α_i ; optical gain, $g(N, \lambda)$; carrier injection efficiency, η_i ; confinement factor, Γ ; mirror reflectivity R ; recombination coefficients, A, B, C ; and group velocity $n_g(N, \lambda)$.

The split-step Fourier method was presented as a first-pass exploration into numerical methods for solving modelocked laser problems. While it fails to prove practically applicable, it does provide much insight into modelocked laser dynamics. It also provides inspiration to the SSFD method explained in Chapter 4.

The SSFD method was developed to answer the needs of a simulation method that could provide accurate and practical information about biasing and designing modelocked lasers. Using this method, we can design semiconductor modelocked lasers around the parameters of our choice. This should be of primary importance when designing superior performance lasers for optical A/D converters.

As closing, a list of future works is enumerated below to provide the reader with further

projects to continue the research presented in this thesis.

5.2 Future Work

5.2.1 Active Modulation

The most accurate modeling of the RF modulation could be as a sinusoidal voltage source. In either case, the active modulation depth should be very minimal (much lower than the design graphs presented in this thesis) and almost the same as a passively modelocked laser that is biased similarly, just without the RF modulation. The true round trip frequency of the modelocked laser is different than that calculated by a pure group velocity calculation, and the modulation frequency should be tuned to this true round-trip frequency. This frequency can be found by passively modelocking the laser without the RF source and measuring the round trip frequency. The addition of the RF source should not change this value too drastically. Its true usefulness is not portrayed in the simulations in this thesis; the real effect is to make the laser more robust to noise, which is not introduced in this simulation (this is left to future work). It is only interesting in detuning experiments. It can show how frequency detuning affects the dynamics of the laser. It would be more accurate to rerun the simulations in this thesis without the active modulation. This would give more accurate simulation results than an overestimate of the RF modulation depth. Due to the time constraints on this thesis, this work is left to future research.

5.2.2 Phase Effects

The most significant improvement to the model is the addition of phase to the photon field. Phase can be accounted for in the same manner as the split-step method: track the evolution of a field magnitude term and a phase term. The field finite difference equation is simply:

$$E^\pm(z \pm \Delta z, t + \Delta t) = E^\pm(z, t) + \Delta t \left[\frac{1}{2} v_g (\Gamma g_p(z, t) - \alpha_i) E^\pm(z, t) \right] \quad (5.1)$$

We can account for self-phase modulation simply through a finite difference equation that parallels Equation 4.8:

$$\Phi^\pm(z \pm \Delta z, t + \Delta t) = \Phi^\pm(z, t) - \Delta t \left[\frac{1}{2} v_g \Gamma \alpha g_p(z, t) \right] \Phi^\pm(z, t) \quad (5.2)$$

The gain bandwidth filter must be fit to a field bandwidth Fourier filter:

$$\frac{\tilde{E}_{out}(\omega)}{\tilde{E}_{in}(\omega)} = \exp \left[-\frac{1}{2} \omega^2 t_2^2 \Gamma g_p(N) \Delta z \right] \quad (5.3)$$

The dispersion should be fit to a slightly different filter:

$$\frac{\tilde{E}_{out}(\omega)}{\tilde{E}_{in}(\omega)} = \exp \left(-j \frac{1}{2} \beta_2 \omega^2 \Delta z \right) \quad (5.4)$$

where

$$\beta_2 = t_2^2 \Gamma g_p(N) \quad (5.5)$$

However, since phase itself is slightly different than magnitude:

$$\exp(j\Phi_{out}(\omega)) = \exp(j\Phi_{in}(\omega)) \exp \left(-j \frac{1}{2} \beta_2 \omega^2 \Delta z \right) \quad (5.6)$$

the actual filter should look like:

$$\frac{\Phi_{out}(\omega)}{\Phi_{in}(\omega)} = -\frac{1}{2} \beta_2 \omega^2 \Delta z \quad (5.7)$$

A suitable difference equation filter is:

$$\gamma [-\Phi_{in}(t - \Delta t) + 2\Phi_{in}(t) - \Phi_{in}(t + \Delta t)] = \Phi_{out}(t) \quad (5.8)$$

whose frequency response is:

$$\frac{\tilde{\Phi}_{in}(\omega)}{\tilde{\Phi}_{out}(\omega)} = \gamma [\cos(\omega\Delta t) - 1] \quad (5.9)$$

This function can be fit to the actual frequency response of the dispersion effect. It is left to future work for the implementation of this technique.

5.2.3 Direct Derivative Filter

Another method for implementation of the finite gain bandwidth is the Direct Derivative Filter (DDF) method. It recognizes that Equation B.9 contains an inherent filter in the full gain term. We can examine the gain terms (including gain bandwidth):

$$v_g \Gamma g_p(z, t) \left[1 + t_2^2 \frac{\partial^2}{\partial t^2} \right] S^+(z, t) \quad (5.10)$$

Writing the definition for the filtered photon density, S_F ,

$$S_F(z, t) \equiv 1 + t_2^2 \frac{\partial^2}{\partial t^2} S(z, t) \quad (5.11)$$

it is immediately obvious that the unity plus second-partial define a filter that can be described in the Fourier-domain:

$$\frac{\tilde{S}_F(\omega)}{\tilde{S}(\omega)} = 1 - t_2^2 \omega^2 \quad (5.12)$$

Hence, we can again use the same technique of filter approximation to account for this transformation as in Section 4.7.1:

$$\frac{\tilde{S}_F(z, \omega)}{\tilde{S}(z, \omega)} = 1 + 2\eta [\cos(2\omega\Delta t) - 1] \quad (5.13)$$

Figure 5-1 shows what the actual filter looks like, including a fitted difference equation filter approximation. Note that the fitting for $t_2 = 5 \times 10^{-13} s$ and $t_2 = 1 \times 10^{-13} s$ are

both quite accurate, relative to the SSFD method filtering. However, when used, this method suffers from the same unbounded error that the SSFD method exhibits when the bandwidth parameter goes above 0.5. However, this method provides a bit more room: it becomes unbounded at values above $\eta > 1$. For the latter case, the fit for η is below one. However, for the value of t_2 that is used in this thesis, η is well above one for the $t_2 = 5 \times 10^{-13} s$ case, rendering it useless for bandwidth parameter values this high. If an acceptably lower value of t_2 can be used, this method would qualify as the more superior.

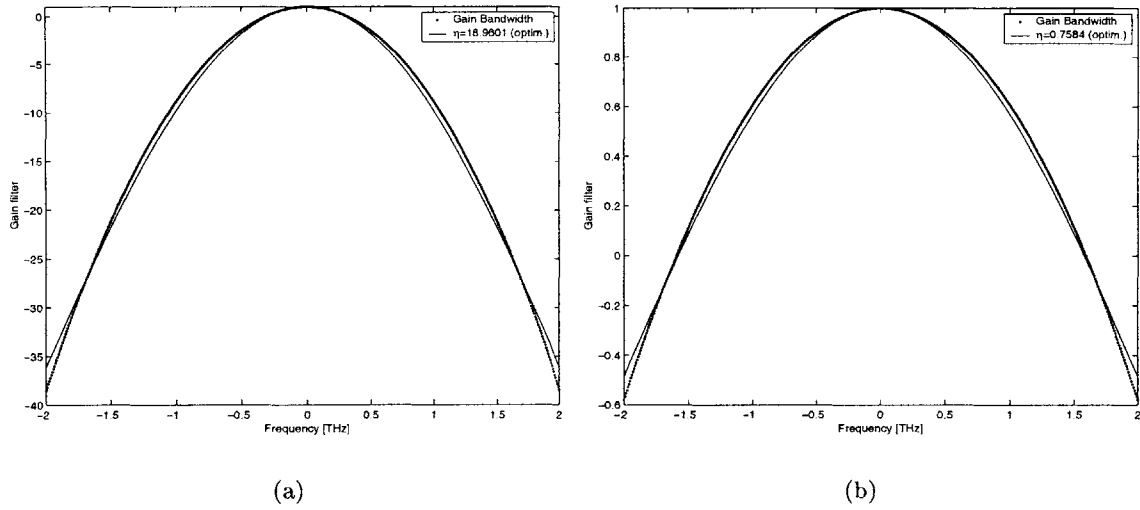


Figure 5-1: Actual filter with fitted filter for $\Delta z = 5 \mu m$. (a) $t_2 = 5 \times 10^{-13} s$ (b) $t_2 = 1 \times 10^{-13} s$

Once the photon density is filtered and S_F is obtained, we can use it in a difference equation, combining Equations B.9 and 5.11:

$$\frac{S^\pm(z \pm \Delta z, t + \Delta t) - S(z, t)}{\Delta t} = -v_g \alpha_i S(z, t) + v_g \Gamma g_p(z, t) S_F(z, t) \quad (5.14)$$

This method promises the most accurate filtering technique since it is not a split-step method. However, the current filter can be a poor fit if the bandwidth factor, t_2 is too large. The method's filtering accuracy depends greatly on the space step chosen, Δz , and

the gain bandwidth factor, t_2 . The larger the space step, the more narrow a filter it can fit.

5.2.4 Filtering Limit

The filter coefficient in the SSFD method cannot be set above 0.5. Otherwise, an unstable error similar to the second-order derivative approximation in Section 4.5.2 can occur. This upper-bound limits the size of the bandwidth parameter, t_2 . Hence, the stronger the filter needs to be, the less accurate it will be. Possible solutions are to develop another filter, possibly a higher order one (containing more terms).

5.2.5 Energy Conservation

The SSFD method performs a filtering after the new carrier density and photon density are determined. Without filtering, there is a one-to-one correlation to the number of photons gained/lost to the number of carriers lost/gained. The filtering always has a magnitude equal to or less than one. This results in a decrease in only the photon density, hence destroying the detailed balance that we had prior to the filter. In order to regain this balance, the number of photons that were lost from prior to after the filter can be easily calculated. This number of carriers can then be added back to the new carrier density. In addition, this calculation has the added benefit of maintaining spatial dependence. Carroll et al. mention the importance of maintaining particle balance in [50].

5.2.6 Lax Averaging

Carroll discusses a technique called Lax averaging and states that it is a more accurate method for approximating the pulse evolution difference equation [7]. For a basic first-order differential equation,

$$\frac{d}{dt}S(t) = g(t)S(t) \approx \frac{S(t + \Delta t) - S(t)}{\Delta t} \quad (5.15)$$

The traditional method of Euler approximation is to define the derivative at time t :

$$S(t + \Delta t) = (1 + \Delta t g(t))S(t) \quad (5.16)$$

If Δt is very small, another approximation method is to define the derivative at time $t + \Delta t$:

$$\frac{d}{dt}S(t) = g(t + \Delta t)S(t + \Delta t) \approx \frac{S(t + \Delta t) - S(t)}{\Delta t} \quad (5.17)$$

which leads to:

$$S(t + \Delta t) = \frac{1}{1 - \Delta t g(t + \Delta t)}S(t) \quad (5.18)$$

These two can be combined:

$$S(t + \Delta t) = \frac{1 + \frac{1}{2}\Delta t g(t)}{1 - \frac{1}{2}\Delta t g(t)}S(t) \quad (5.19)$$

where $g(t)$ is taken to be the value at t for both the numerator and denominator. Equation 5.19 is called a Lax average approximation for the differential equation. It is not difficult to implement Lax averaging in the SSFD method. It is unsure whether the improvement is worth the added computation time and complexity. Preliminary simulations comparing a Lax-averaged and non-Lax-averaged pulse steady state show a marginal difference.

5.2.7 Spontaneous Emission Modeling

The SSFD method can take any arbitrary initial pulse (even a singularity of very low photon density) and produce the same steady state, provided the biasing is the same. However, the ultimate goal would be to model spontaneous emission and allow it to build into a pulse. Proper statistics are necessary to model it in a correct and physical manner. Several authors discuss this modeling [30, 64].

Appendix A

Matlab Code

A.1 Hakki-Paoli Code

A.1.1 hakki.m

```
% HAKKI    Finds overall laser loss/gain spectrum
% a = hakki(L,R,sp,avenum)
%
%  L:      length of laser (cm)
%  R:      Power reflection coefficient
%  sp:     matrix of two column vectors
%          col.1: lambda[nm]: wavelength of each photon gain, a, found
%          col.2: Optical Power[dB]: intensity spectrum
%  avenum: # of 'a' points to average over
%
%  output: matrix of two column vectors
%          col.1: wavelength of each photon gain, a, found [nm]
%          col.2: photon gain [cm^-1] = Gamma*g-alpha_i
%
function a = hakki(L,R,sp,avenum)

%#####
% split up sp matrix into lambda and P_dBm vectors
lambda=sp(:,1);
PdBm=sp(:,2);
PmW=10.^(PdBm/10);

%#####
% calls FINDPEAK script
findpeak;

%#####
% plot the spectrum
```

```

figure;
set(gcf,'Position',[50 50 500 400]);
plot(lambda,PdBm,lambda(Ipeak), ...
      PdBm(Ipeak),'og',lambda(Inull),PdBm(Inull),'vm');
axis tight;
xlabel('Wavelength [nm]');
ylabel('Transmission I/I_o [dB]');
title('Hakki-Paoli Minima/Maxima with Wavelength vs. Transmission');

%*****
% convert maxima and minima values from dBm to Watts
Pmax = PmW(Ipeak); % [mW]
Pmin = PmW(Inull); % [mW]

%*****
% calculate a (positive is gain, neg. is loss)
for N=1:length(Pmin)-1
    r(2*N-1) = 2*Pmax(N+1)./(Pmin(N)+Pmin(N+1));
    r(2*N)   = (Pmax(N)+Pmax(N+1))./(2*Pmin(N));
    alambda([2*N-1 2*N])=[lambda(Ipeak(N)) lambda(Inull(N))];
end;
a=-(1/L)*log(R*(sqrt(r)+1)./(sqrt(r)-1));

%*****
% averaging
for I=1:length(a)-avenum
    atemp(I) = mean(a(I:I+avenum));
    alambdatemp(I) = mean(alambda(I:I+avenum));
end;
a = [alambdatemp' atemp'];

%*****
% plot gain vs. wavelength
figure;
set(gcf,'Position',[600 50 500 400]);
plot(alambdatemp,atemp);
xlabel('Wavelength [nm]');
ylabel('\Gamma_g - \alpha_i [cm^{-1}]');
title('Photon Gain vs. Wavelength');

```

A.1.2 findpeak.m

```

%FINDPEAK Finds indices for peaks and nulls of the Fabry-Perot spectrum
% input:  sp(:,[1 2])
%         lambda = lambda vector (nm)
%         PmW    = Power vector (mW)
%         WinLen = Number of Index points between maxima
%
% output: Inull(:) = index vector of nulls within PmW
%         Ipeak(:) = index vector of peaks within PmW

```



```

##### 10
% grab approx. wavelength difference between peaks (free spectral range?)
figure;
plot(lambda,PmW);
xlabel('Wavelength [nm]'); ylabel('Power [mW]');
zoom;
disp('Zoom until left-most Fabry-Perot nulls are visible. ');
disp('Press ANY KEY to continue. ');
pause;
zoom off;
disp('Select two consecutive minima nulls, left to right, for beginning. '); 20
peak_input=ginput(2);
lambdal=find(lambda>peak_input(1,1));
lambd2=find(lambda>peak_input(2,1));
WinLen=abs(lambd2(1)-lambdal(1)); % number of points between peaks: approx

#####
% initializes the peak-finding window
IWindow = [WinLen:3*WinLen];
[temp Imax] = max(PmW(IWindow));
Ipeak(1) = Imax + IWindow(1) - 1; 30
ILambdaStart = Ipeak(1) - floor(WinLen/2);
ILambdaEnd = ILambdaStart + WinLen;
IWindow = [ILambdaStart:ILambdaEnd];
WinLen = length(IWindow);
N=1;

#####
% finds peak indices
while (Ipeak(N) + ceil(WinLen/2) + WinLen <= length(lambda)) 40
    IWindow = [ILambdaEnd : ILambdaEnd + WinLen];
    N=N+1;
    [temp Imax] = max(PmW(IWindow));
    Ipeak(N) = Imax + IWindow(1) - 1;
    ILambdaEnd = Ipeak(N) + ceil(WinLen/2);
    WinLen = Ipeak(N) - Ipeak(N-1);
end;

#####
% finds null indices
for N = 1:length(Ipeak)-1 50
    IWindow = [Ipeak(N):Ipeak(N+1)];
    [temp Imin] = min(PmW(IWindow));
    Inull(N) = Imin + IWindow(1) - 1;
end;

```

A.2 Split-step Fourier Code

A.2.1 modelock.m

```

%MODELOCK Modelock Laser Simulation Script
% Simulates modelock pulse evolution using the split-step Fourier method
% developed by D.J.Derickson et al.
% specify the first pulse in variable "pulseone" as = 'new'
% or = 'prev' prior to running
% specify Laser Parameter File at *1
%
% See also LASERPARAM, SPLITSTEP, MAKERTMATRIX, FINDWIDTH, PLOTMODELOCK.

global q h c hv a 10

%#####
% *1 Loads laser parameters from file
LaserParam;

%#####
% Constants
q = 1.609e-19; % [C] Coulomb/charge
h = 6.626176e-34; % [J*s] Planck's constant
c = 3e10; % [cm/s] Speed of light 20
hv = h*c/lambda; % [J] Energy/photon

%#####
% Initial pulse parameters
Tw = 50e-12; % [s] width of window
tp = 8e-12; % [s] initial width of pulse
Apeak = .8e0; % [=sqrt(W)] initial peak field amplitude of pulse
noP = 2^11; % number of points in the window

%##### 30
% Initial pulse construction
ptau = Tw*2/noP*[fliplr([1:noP/2] [0:noP/2-1])]; % [s]
tau = Tw*2/noP*[-noP/2+1:noP/2]; % [s]
dtau = tau(2)-tau(1); % [s] period, T
t0 = sqrt(tp^2/4/log(2)); % [s] time std. dev.
Ai = Apeak*exp(-ptau.^2/2/t0^2); % [W^(1/2)] the pulse

%#####
% decide whether first pulse is new (specified above) or last pulse from prev. run
switch pulseone 40
case 'prev', % yes, continue previous pulse propagation
% Recenters the pulse so it doesn't migrate out of the time window
[PeakVal PeakI] = max(abs(Art(end,:)).^2);
TrueMidI = noP/2;
PeakDiffI = PeakI - TrueMidI;
if PeakDiffI <= 0, %if the peak is offset to the left
tmp = [zeros(1,-PeakDiffI), Art(end,1:end+PeakDiffI)];
else, % if the peak is offset to the right

```

```

    tmp = [Art(end,1+PeakDiff:end), zeros(1,PeakDiff)];
    end;
    Art = zeros(noPass+1,noP);
    Art(1,:) = tmp;
case 'new',
    Art = zeros(noPass+1,noP);
    Art(1,:) = Ai;
    Penergy = [];
    Pwidth = [];
    Pwidthtemp = [];
    Pheight = [];
otherwise,
    error('Specify variable: pulseone');
end;

#####
% create roundtrip propagation matrix of different parameters
[Tmtx, Lmtx, Lsectmtx, Imtx] = makeRTmatrix(Tmat, Lmat, Nmat, Imat);

#####
% The actual propagation
Ap = zeros(length(Lmtx)+1,noP,noPass);
Pratio = ones(length(Lmtx),noP,noPass);
PHI = zeros(size(Pratio));
for P = 1:noPass,
    % assigns the previous roundtrip's last field as the initial pulse in this roundtrip
    Ap(1,:,P) = Art(P,:);
    for n = 1:length(Lmtx)
        switch Tmtx(n)
            case 'P',
                a = aSA; % changing differential gain => E_sat changes
                [Ap(n+1,:,P),Pratio(n,:,P),dPHI(n,:,P)] = splitstep(Ap(n,:,P), ...
                    tau,Tmtx(n),Lmtx(n),Imtx(n),Lsectmtx(n));
            case 'G',
                a = aG; % changing differential gain => E_sat changes
                [Ap(n+1,:,P),Pratio(n,:,P),dPHI(n,:,P)] = splitstep(Ap(n,:,P), ...
                    tau,Tmtx(n),Lmtx(n),Imtx(n),Lsectmtx(n));
            case 'M',
                Ap(n+1,:,P) = sqrt(R)*Ap(n,:,P);
                Pratio(n,:,P) = R*ones(1,noP); % it's just the mirror reflectivity
                dPHI(n,:,P) = zeros(1,noP);
            otherwise,
                error('propagation');
        end;
    end;
    Art(P+1,:) = Ap(end,:,P); % save the last one to the roundtrip field matrix
end;

#####
% Determine pulsewidth vector, pulse energy, shaping function, matrices
for P = 1:noPass+1,
    Pwidthtemp(P) = findwidth(Art(P,:),tau);

```

```

end;
Pwidth=[Pwidth(1:end-1) Pwidthtemp];           % Pulse width [s]
Prt = abs(Art).^2;                               % Power matrix
Penergy = [Penergy(1:end-1) sum(Prt,2)*dtau];   % energy per roundtrip [J]
Pratio = [ones(noP,1) squeeze(prod(Pratio,1))]; % shaping function
dPHIsum = [zeros(noP,1) squeeze(sum(dPHI,1))]; % delta-phase function
Pheight = [Pheight(1:end-1) max(Prt,[],2)'];    % Pulse height per roundtrip [W]

```

```

%#####
% Specify file that plots the results

```

110

```

PlotModelock;

```

A.2.2 LaserParam.m

```

%LASERPARAM Physical parameters and Laser Geometry
% Sample: UCSB modelocked lasers
%
% Called by MODELOCK.

```

```

global W tQW nQW Gamma Bsp lambda alpha Esatratio nG etai alhai ...
A B C g0 Ntr hv d tctr R aG aSA t2 B2

```

```

%#####
% Physical parameters

```

10

```

W = 1.5e-4;           % [cm]           Width of laser stripe
tQW = 70e-8;         % [cm]           Thickness of Quantum Well
nQW = 6;              %                # of Q.W.

```

```

%#####
% Theoretical quantities

```

```

Gamma = .008037*nQW; % -           Confinment factor
lambda = 1550e-7;    % [cm]           Lasing wavelength
alpha = 2;           % -           linewidth enhancement factor *
Esastratio = 5;      % -           ratio of Gain region's Esat to S.A.'s Esat *

```

20

```

%#####
% Measured quantities

```

```

nG = 3.2;            % -           Group index
etai = 0.77;         % -           Internal efficiency
A = 0;              % [1/s]           trap recomb. coeff.
B = 1e-10;          % [cm^3/s]       S.E. coefficient (Rsp = B*N^2)
C = 1e-28;          % [cm^6/s]       Auger recomb. coeff. (typ [7-9]e-29)

```

```

%#####
% Gain curve fits

```

30

```

g0 = 1864;           % [cm^-1]       Max Gain coefficient
Ntr = 1.82e18;       % [cm^-3]       Transparency carrier Density(at300K)

```

```

%#####

```

```

% Derived parameters
d = tQW*nQW; % [cm] Total Q.W. length
tctr = 1/(A + B*Ntr + C*Ntr^2); % [s] Carrier lifetime at transparency
R = ((nG-1)/(nG+1))^2; % Mirror power reflectivity
aG = g0/(Ntr); % [cm^-2] Differential gain (lin. model) Gain sect. 40
aSA = aG*Esatratio; % [cm^-2] Differential gain (lin. model) Sat. Abs.

%#####
% gain bandwidth filtering parameters
t2 = 5e-13; % [s] gain bandwidth param. (taylor expand g vs. w)

%#####
% Modelocked laser geometry
% each vector entry signifies a different section in the laser
% Nmat and Lmat should be constructed such that each splitstep part 50
% is about 50e-4 long
%
% Types: 'P' = passive, 'G' = gain, 'A' = active, 'M' = mirror
% note: mirrors are automatically put in
Tmat = ['P' 'G' ]; % section Type
Lmat = [80e-4 3500e-4 ]; % section Length
Nmat = [4 35 ]; % number of splitstep parts in each section
Imat = [0.05 63e-3 ]; % section current bias
noPass = 10;

```

60

A.2.3 makeRTmatrix.m

```

function [Tmtx, Lmtx, Lsectmtx, Imtx] = makeRTmatrix(Tmat, Lmat, Nmat, Imat);
%MAKERTMATRIX Creates the space-varying matrix of state variables
%
% Called by MODELOCK.

%#####
% construct roundtrip laser geometry matrices
Trt = [Tmat 'M' fliplr(Tmat) 'M' ];
Lrt = [Lmat 0 fliplr(Lmat) 0 ];
Nrt = [Nmat 0 fliplr(Nmat) 0 ];
Irt = [Imat 0 fliplr(Imat) 0 ];

```

10

```

%#####
% construct the split-step information matrices
Lsectmtx = [];Lmtx = [];Imtx = [];Tmtx = [];
for n = 1:length(Lrt)
    switch Trt(n)
        case 'P', % absorber section
            Tmtx = [Tmtx repmat('P',1,Nrt(n))];
            Lmtx = [Lmtx Lrt(n)/Nrt(n)*ones(1,Nrt(n))];
            Lsectmtx = [Lsectmtx Lrt(n)*ones(1,Nrt(n))];
            Imtx = [Imtx Irt(n)*ones(1,Nrt(n))];
        case 'G', % gain section

```

20

```

    Tmtx = [Tmtx repmat('G',1,Nrt(n));
    Lmtx = [Lmtx Lrt(n)/Nrt(n)*ones(1,Nrt(n));
    Lsectmtx = [Lsectmtx Lrt(n)*ones(1,Nrt(n));
    Imtx = [Imtx Irt(n)*ones(1,Nrt(n));
case 'M', % mirror section
    Tmtx = [Tmtx 'M'];
    Lsectmtx = [Lsectmtx 0];
    Lmtx = [Lmtx 0];
    Imtx = [Imtx 0];
case 'S', % free space
otherwise,
    'error makeRTmatrix'
end;
end;

```

A.2.4 splitstep.m

```

function [Aout,Pratio,dPHI] = splitstep(Ain,tau,T,L,I,Lsect)
% SPLITSTEP Takes pulse profile Ain(tau) and performs splitstep filtering on it.
% [Aout,Pratio,dPHI] = SPLITSTEP(Ain, tau, L, I, Lsect)
%
% Ain [sqrt(W)] pulse envelope
% tau [s] time vector of Ain
% T (string) type of this section (S.A.,gain, mirror, etc.)
% L [cm] length of splitstep segment
% I [A] current in segment
% Lsect [cm] length of current-isolated section (total)
%
% Aout [sqrt(W)] output pulse envelope
% Pratio ratio of output/input power (vector)
% dPHI difference of output-input phase
%
% Called by MODELOCK.

```

global q h c W tQW nQW Gamma Bsp lambda nG etai ...
A B C g0 Ntr hv d a tctr alpha t2 B2

```

%#####
% Derived parameters
V = Lsect*W*d; % [cm^3] Volume of active region (Q.W.)
Itr = q*V*Ntr/tctr/etai; % [A] Transparency current

noP = length(tau);
dtau = tau(2)-tau(1); % [s]

%#####
% phase and intensity of input A
% Uin is the integrated energy of the pulse
PHiin = angle(Ain);
Pin = abs(Ain).^2;
Uin = cumtrapz(Pin)*dtau;

```

```

#####
% finds gain from linear gain model
if T == 'P'
    gp = log(I)/Lsect;
    heff = gp*L;
    G0 = exp(heff);
elseif T == 'G'
    dN = Ntr*(etai*I/Itr - 1); % carrier density difference from Ntr
    gp = Gamma*a*dN; % linear gain model
    heff = gp*L;
    G0 = exp(heff); % commented out and explicitly stated in modelock.m
else
    error('error finding G0');
end

Esat = hv*W*d/a/Gamma;
Pratio = 1./(1-(1-1/G0)*exp(-Uin/Esat));
Pout1 = Pin.*Pratio;
dPHI = alpha/2*log(1-(1-1/G0)*exp(-Uin/Esat));
PHIout1 = PHIin + dPHI;
Aout1 = sqrt(Pout1).*exp(j*PHIout1); % field from first part of splitstep

#####
% Dispersion parameter
B2 = gp*t2^2; % [cm/s^2] dispersion parameter

#####
% gain bandwidth filtering (only in gain sections)
switch T
case 'G'
    if gp<0
        error('Gain in gain region cannot be negative');
    end
    FAout1 = fft(Aout1);
    w = 2*pi*[0:noP/2] fliplr([1:noP/2-1])/(noP*dtau);
    filt = exp(-w.^2*t2^2*gp*L/2).*exp(-j*B2*L*w.^2/2);
    Aout = ifft(FAout1.*filt);
case 'P'
    Aout = Aout1;
otherwise
    error('splitstep');
end

#####
% tests to see if the window you picked was big enough
if or(abs(Aout(1)) >= 1e-10,abs(Aout(end)) >=1e-4),
    'Warning: Window time span may be too small.'
end

#####
% add some stuff to get rid of anomalies happening due to Fourier transform on sides

```

```

sides = abs(blackman(noP*2^(-3))');
lside = sides(1:end/2);
rside = sides(end/2+1:end);
middle = ones(1,noP-length(sides));
win = [lside middle rside];
Aout = Aout.*win;

```

90

A.2.5 findwidth.m

```

function width = findwidth(A,time);
%FINDWIDTH Finds width of the pulse
% width    = width of pulse FWHM power [s]
% A        = field amplitude of pulse [field amplitude]
% time     = time vector that defines A(t) [s]
%
% Called by MODELOCK.

P      = abs(A).^2;
[Ppeak ind] = max(P);
FWHM   = find(P > Ppeak/2);
width  = time(FWHM(end)) - time(FWHM(1));

```

10

A.2.6 PlotModelock.m

```

%PLOTMODELOCK Plots pulse profile/width/energy evolution
%
% Called by MODELOCK.

%#####
ps    = 1e-12; % define picosecond scaling factor
pJ    = 1e-12; % defines picoJoule scaling factor

figure;

%#####
% Plot pulse profiles per roundtrip
subplot(4,1,1);
plot(tau/ps,Prt);
ylabel('Pulse Profile [W]');
axis([tau(1)/ps tau(end)/ps 0 1.1*max(max(Prt))]);

%#####
% Plot shaping function profile per roundtrip
subplot(4,1,2);
plot(tau/ps, Pratiosum);
ylabel('P_{out}/P_{in}');
axis([tau(1)/ps tau(end)/ps 0.8*min(min(Pratiosum)) 1.1*max(max(Pratiosum))]);
xlabel('Time [ps]');

```

10

20


```

#####
% Plot pulse width per roundtrip
subplot(4,1,3);
plot([0:length(Pwidth)-1], Pwidth/ps);
ylabel('Pulsewidth [ps]');
axis([0 length(Pwidth)-1 0 1.1*max(Pwidth)/ps]);
text(length(Pwidth)*.8,Pwidth(end)/ps+.3,[num2str(Pwidth(end)/ps),' ps']);

#####
% Plot pulse energy per roundtrip
subplot(4,1,4);
plot([0:length(Penergy)-1], Penergy/pJ);
ylabel('Energy [J]');
axis([0 length(Penergy)-1 0 1.1*max(Penergy)/pJ]);
text(length(Penergy)*.8,Penergy(end)/pJ+.3,[num2str(Penergy(end)/pJ),' pJ']);
xlabel('Roundtrip #');

#####
% Sticks some laser geometry/bias info on bottom
set(gcf,'Position',[10 10 800 800]);
label = 'Type   Len[um]   #Div   Bias[A]   ';
Geom=num2str([Lmat;Nmat;Imat]');
SType=[repmat(' ',length(Tmat),3) Tmat' repmat(' ',length(Tmat),7)];
Geom = [SType Geom repmat(' ',length(Tmat),8)];
label = label(1:length(Geom(1,:)));
Geom = [label;Geom];
Ht=uicontrol(gcf,'Style','text', ...
'Position',[10 10 350 60],'String',Geom,'BackgroundColor',[0.8 0.8 0.8]);

#####
% Labels the graph
subplot(4,1,1);
title(['\alpha=', num2str(alpha),' ', E_{sat} Ratio=', num2str(Esatrio), ...
', # Points=', num2str(noP)]);

```

30

40

50

60

A.3 Split-step Finite Difference Code

A.3.1 findGBWFunc.m

```

%FINDGBWFUNC Finds the polynomial fitting functions for gain bandwidth
% Run this before running FDIFFMAIN.

```

```

#####
% Load laser parameters (just to grab t2)
LaserParam;

```

```

#####
% User preferences
dzM = [1:13]*1e-4; % [cm] space step

```

10

```

fRange = 2e12;           % [1/s]           max range of freq. to fit
gpM = linspace(1,1000,100); %           Good for N={Ntr,8e18)
f = linspace(-1,1,500)*fRange; % [Hz]     freq. vector
f0 = 0;
w = 2*pi*f;             % [s^-1]         ang. freq. vector
w0 = 2*pi*f0;
THz = 1e12;             % [Hz]           units constant

#####
% Defines function to optimize (and optim. param.s)
opts = optimset('lsqcurvefit');
opts = optimset(opts,'TolFun',1e-15,'MaxFunEvals',1e4,'MaxIter',1e4, ...
'Display','off','TolX',1e-6);
gbw=inline('1+2*eta*(cos(2*w*dt)-1)','eta','w','dt');

for D=1:length(dzM),

    dz = dzM(D);
    dt = dz*nG/c;
    #####
    % Optimizes over the range of g-p
    clear GainM HM etaFM;
    tic;
    for X = 1:length(gpM),
        GainM(X,:) = exp(-Gamma*gpM(X)*dz*t^2*(w-w0).^2);
        gI = find(GainM(X,:) >= 0.2);
        [etaFM(X) resnorm] = lsqcurvefit(gbw,0,w(gI),GainM(X,gI),[],[],opts,dt);
        HM(X,:) = gbw(etaFM(X),w,dt);
        HM(find(HM<0)) = 0;
        disp(['Optimized # ' num2str(X)]);
    end
    disp(['Elapsed optimization time: ' num2str(toc) ' secs.']);
    figure;
    set(gcf,'position',[50 50 400 800]);
    #####
    % plot the fitting functions
    subplot(311);
    surf(f/THz,gpM,HM);shading interp;
    xlabel('Freq [THz]');ylabel('Gain, g_p [cm^{-1}]');zlabel('Optim. Func. ');
    #####
    % Polynomial fitting function
    rutM = polyfit(gpM,etaFM,5);
    subplot(312);
    plot(gpM,etaFM,gpM,polyval(rutM,gpM));
    xlabel('Gain (g_p)');ylabel('Gain Bandwidth Parameter (\eta_F) ');
    #####
    % Find and plot the error
    errM = abs(HM-GainM);
    subplot(313);
    surf(f/THz,gpM,errM); shading interp;
    xlabel('Freq [THz]');ylabel('Gain, g_p [cm^{-1}]');zlabel('Error');
    #####

```

```

    % save the polynomial coefficients to the saving cell
    rutC{D} = rutM;

end

eval(['save GBWParam' num2str(t2,'%0.0g') 'rutC dzM;']);

```

A.3.2 fdiffMain.m

```

%FDIFFMAIN Simulates modelocked laser.
% This is the MAIN parameter initialization SCRIPT
% Run this script to simulate the modelocked laser.
%
% See also LASERPARAM, FDIFFLOOP.

more off;
%#####
% Initializes laser parameters (Be sure this is executed before running this script)
% If batchrun has been run already, then do not run 'LaserParam'
if ~exist('batchrunScriptFlag'),
    disp(' ');disp('LOADING: LASERPARAM.m');
    LaserParam;
end;
%#####
% Laser Params, Calculated
Area = W*Lsect; % [cm^3] Area of active region
V = W*d*Lsect; % [cm^3] Volume of active region
vG = c./nG; % [cm/s] group velocity
dz = dt*vG; % [cm] Discretized length step
noP = round(Lsect./dz); % # of discretized points
Lsect = noP.*dz; % [cm] (revised) section lengths
%#####
% Gain BW Param loading
eval(['load GBWParam' t2str]);
rutM = rutC{find(round(dzM*1e4)==round(dz(2)*1e4))};
maxeta = 0.49;
%#####
% Modulation Params, Calculated
ActI = find('Type=='A'); % active section index
Trt = 2*sum(Lsect./vG); % [s] roundtrip time
noPRT = round(1/((Fdtun+1/Trt)*dt)); % # pts. incl. detuning
wM = 2*pi*(1/Trt+Fdtun); % [rad/s] mod. freq.
P = 5*noPRT; % # points between graph commands
S = noPRT; % # points between 'store state' command
pdispN = 50; % # prev. pulses to display
%#####
% Initialize space-varying variables
%#####
% Finds steady-state carrier density (Nss), given current & no photons
for X = 1:length(Lsect)
    if Ibias(X)<0, Nss(X) = 0;

```

```

else
    Nroots(:,X) = roots([C B A(X) -etai*Ibias(X)/q/V(X)]);
    if isreal(Nroots(:,X)), Nss = max(Nroots(:,X));
    else,
        for Y = 1:length(Nroots(:,X)),
            if isreal(Nroots(Y,X)), Nss(X) = Nroots(Y,X);
            end; end; end; end; end;
end

zM = []; LsectM = []; NM0 = [];
AM = []; BM = []; CM = [];
sectI = []; IM = []; VM = [];
alphiM = []; vGM = [];
for X = 1:length(Lsect)
    if isempty(zM)
        sectI{X} = [1:noP(X)];
        zM = linspace(dz(X)/2,Lsect(X)-dz(X)/2,noP(X));
    else
        sectI{X} = [1:noP(X)]+sectI{X-1}(end);
        zM = [zM linspace(dz(X)/2,Lsect(X)-dz(X)/2,noP(X))+sum(Lsect(1:X-1))];
    end
    LsectM = [LsectM Lsect(X)*ones(1,noP(X))];
    NM0 = [NM0 Nss(X)*ones(1,noP(X))];
    AM = [AM A(X)*ones(1,noP(X))];
    BM = [BM B(X)*ones(1,noP(X))];
    CM = [CM C(X)*ones(1,noP(X))];
    IM = [IM Ibias(X)*ones(1,noP(X))];
    VM = [VM V(X)*ones(1,noP(X))];
    alphiM = [alphiM alphi(X)*ones(1,noP(X))];
    vGM = [vGM vG(X)*ones(1,noP(X))];
end
tM = zM./vGM;
tRTM = linspace(dt,S*dt,S)-dt/2;
if isempty(find(diff(vGM)))
    vGM = vGM(1);
end;

%#####
% Initial pulse parameters
[Lmax X] = max(Lsect); % choose which section for pulse origin
PeakPower = 1e0; % [cm^-3] peak pulse power
tMG = zM(sectI{X})/vG(X); % [s] time markers in the gain section
tp = 1e-12; % [s] pulse width
t0 = sqrt(tp^2/4/log(2)); % [s] time std. dev.
SfM0 = zeros(size(zM)); % [cm^-3] Forward-traveling photon density
SrM0 = zeros(size(zM)); % [cm^-3] Forward-traveling photon density
SrM0 = 1; SfM0 = 1; % [cm^-3] Spatially-uniform photon density

%#####
% Initializes roundtrip saving matrices
SfRT = zeros(noRT,length(tM));
SrRT = zeros(noRT,length(tM));
NRT = zeros(noRT,length(tM));

```

```

SoutM = zeros(noRT,S);
NActM = zeros(noRT,S);
SfActM = zeros(noRT,S);

#####
% Set up initial conditions
NM = NM0;
SfM = SfM0;
SrM = SrM0;
NActM(1,1) = NM(end);
SfActM(1,1) = SfM(end);
ContN = 0; % # of round trip to continue from
Xstart = ContN*S; % starting X value

#####
% Run the main loop of the program
#####

fdiffLoop;

```

A.3.3 LaserParam.m

```

%LASERPARAM Loads modelocked laser parameters.
% Load: physical parameters, laser geometry, and biasing.
% Current Sample: Two-section laser by Hoshida et al.
%
% See also FDIFFMAIN.

#####
% Constants
q = 1.609e-19; % [C] Coulomb/charge
h = 6.626176e-34; % [J*s] Planck's constant
c = 3e10; % [cm/s] Speed of light
ps = 1e-12; % [s] # of seconds in a picosecond (abbrev.)
pJ = 1e-12; % [s] # of Joules in a picoJoule (abbrev.)
mA = 1e-3; % [A] # of Amps in a milliAmp (abbrev.)
um = 1e-4; % [cm] # of centimeters in a micron (abbrev.)
mV = 1e-3; % [V] # of Volts in a milliVolt (abbrev.)
#####
% Physical parameters
W = 2*um; % [cm]* Width of laser stripe
tQW = 40e-8; % [cm]* Thickness of Quantum Well
nQW = 3; % # of Q.W.
#####
% Theoretical quantities
Gamma = .05; % - Confinment factor
lambda = 1550e-7; % [cm] Lasing wavelength
#####
% Measured quantities
nG = 3.7; % - Group index
nEff = 3.2; % - Effective index

```

```

etai = 1; % - Internal efficiency 30
#####
% Gain curve fits
g0 = 3420.8; % [cm^-1] Max Gain coefficient
Ntr = 1.577e18; % [cm^-3] Transparency carrier Density(at300K)
Ns = 2.254e17;
#####
% Derived parameters
hv = h*c/lambda; % [J] Energy/photon
d = tQW*nQW; % [cm] Total Q.W. length
Rair = ((nEff-1)/(nEff+1))^2; % Mirror power reflectivity 40
#####
% Gain bandwidth filtering parameter
t2 = 0.5*ps; % [s] gain bandwidth param. (taylor expand g vs. w)
t2str = num2str(t2,'%0.0g'); % gain bandwidth param. (taylor expand g vs. w)
#####
% DBR specs
Ldbr = 200*um; % [cm] DBR length
kappa = 20; % [cm^-1] mode coupling coeff.
kLg = kappa*Ldbr; %
LeffDBR = round(1/2/kappa*tanh(kLg)*1e4)/1e4; % [cm] DBR effective length 50
rg = tanh(kLg); % DBR effective field reflectivity
#####
% Laser Geometry
Type = ['A' 'G' 'P']; % - Section type
% G=Gain/Absorber,A=Active,P=Passive(no gain),S=Freespace
Lpcont = 150*um; % [cm] Phase Control section length
Lsect = [75e-4 750e-4 Lpcont+LeffDBR]; % [cm] Section lengths
Ibias = [0 60e-3 0]; % [A] DC Current bias
nG = [3.7 3.7 3.7]; % Group index
alphaI = [5 5 5]; % [cm^-1] Optical loss 60
A = [2e11 1e8 0]; % [1/s] Trap recomb. coeff. (A=2e10-2e11)
B = [1e-10 1e-10 0]; % [cm^-3/s] Bimolecular recomb. coeff.
C = [1e-28 1e-28 0]; % [cm^-6/s] Auger recomb. coeff.
dt = (5*um)*nG(2)/c; % [s] Time increment
noRT = 200; % # round trips to execute
Rl = Rair; % Power reflectivity, left-hand side
Rr = 0.43; % Power reflectivity, right-hand side
% (DBR calc'ed from trans. matrix program)
Rint = 0.0; % Internal power reflectivity
##### 70
% Saturable Absorber and Modulation Params
HarmNum = 1; % Harmonic # of the modulation
Fdtun = 0; % [Hz] detuned frequency
IRF = 60*mA; % [A] RF current
phi = 0; % [rad] RF phase shift
#####
% Display/Plotting Flags (0=False, 1=True)
DISP = 1; % [Boolean] Display N(z),S(z),eta(z) graphs

```

A.3.4 fdiffLoop.m

```

%FDIFFLOOP The main loop of the SSFD method
% This is the main loop of the program.
%
% Called by FDIFFMAIN.

%#####
% Plot the initial conditions
if DISP,
if exist('fdiff_fig1'), figure(fdiff_fig1);
else, fdiff_fig1 = figure; end
    set(gcf,'position',[920 40 350 250]);
    set(gca,'position',[.13 .10 .775 .8]);
    gM = g0*log((NM0+Ns)/(Ntr+Ns));
    plot(zM,polyval(rutM,gM));
    set(gca,'xlim',[0 sum(Lsect)]);
if exist('fdiff_fig2'), figure(fdiff_fig2);
else, fdiff_fig2 = figure; end
    set(gcf,'position',[920 700 350 250]);
    set(gca,'position',[.13 .10 .775 .8]);
    plot(zM,SfM0,zM,SrM0);
    set(gca,'xlim',[0 sum(Lsect)]);
if exist('fdiff_fig3'), figure(fdiff_fig3);
else, fdiff_fig3 = figure; end
    set(gcf,'position',[920 370 350 250]);
    set(gca,'position',[.13 .10 .775 .8]);
    plot(zM,NM0);
    set(gca,'xlim',[0 sum(Lsect)]);
end
if exist('StatusF'), figure(StatusF);
else, StatusF = figure; end
    set(gcf,'Position',[560 650 350 20],'MenuBar','none');
    axis off;
    if ~exist('StatusH')
        StatusH = text(0,0.5,'Initialized');
    end;
fdiff_fig4 = figure;
    set(gcf,'position',[560 700 350 250]);
    set(gca,'position',[.13 .10 .775 .8]);
    p3H = plot(tRTM/ps,zeros(size(tRTM)));
    set(gca,'xlim',[0 tRTM(end)/ps]);
    hold on;
    drawnow;
tic;
%#####
% This is the main loop
%#####
for X = 1+Xstart:noRT*noPRT+Xstart,
%#####
% Finds Active section current bias
% IRFcurr current bias for this time step

```

```

% AM      the vector containing A coefficients versus space
% IM      the vector containing bias current versus space
if ~isempty(ActI)
    IRFcurr = IRF*cos((wM*dt*X+phi)/HarmNum);
    IM(sectI{ActI}) = IRFcurr;
end;
#####
% Calculate the next time increment's pulse. loop starts with: NM, SfM, SrM
% loop ends with Sfn, SrMn. these are not filtered yet
% RM      recombination rate vector
% gM      gain vector
% n suffix = next
RM      = (AM + (BM + CM.*NM).*NM).*NM;
gM      = g0*(log(NM+Ns)-log(Ntr+Ns));
G       = 1 + (Gamma*gM-alphaIM).*vGM*dt;
SfMtemp = G.*SfM;
SrMtemp = G.*SrM;
SfMn    = [Rl*SrMtemp(1) SfMtemp(1:end-1)];
SrMn    = [SrMtemp(2:end) Rr*SfMtemp(end)];
#####
% Calculates the next iteration for forward prediction
% nn suffix = next-next
NMn     = NM + (etaI*IM/q./VM - RM - vGM.*gM.*(SfM+SrM))*dt;
NMn(find(NMn<0)) = 0; % ensures that N doesn't fall below 0
gMn     = g0*(log(NMn+Ns)-log(Ntr+Ns));
Gn      = 1 + (Gamma*gMn-alphaIM).*vGM*dt;
SfMtemp2 = Gn.*SfMn;
SrMtemp2 = Gn.*SrMn;
SfMnn    = [Rl*SrMtemp2(1) SfMtemp2(1:end-1)];
SrMnn    = [SrMtemp2(2:end) Rr*SfMtemp2(end)];
#####
% Filters the photon densities to simulate Gain BW
etaFM    = polyval(rutM,gM);
etaFM(find(etaFM<0)) = 0;
etaFM(find(etaFM>maxeta)) = maxeta;
SfM      = etaFM.*(SfMnn + SfM - 2*SfMn) + SfMn;
SrM      = etaFM.*(SrMnn + SrM - 2*SrMn) + SrMn;
SoutM(ceil(X/S),rem(X-1,S)+1) = (1-Rr)*SfM(end);
NM       = NMn;
NActM(ceil(X/S),rem(X-1,S)+1) = NM(sectI{ActI}(1));
SfActM(ceil(X/S),rem(X-1,S)+1) = SfM(sectI{ActI}(1));
#####
% Graph commands (frequency determined by 'P')
if and(X/P == floor(X/P), DISP)
    %Carrier density plot
    figure(fdiff_fig1);
    set(gca,'YLimMode','auto');
    plot(zM,etaFM);
    set(gca,'xlim',[0 sum(Lsect)],'ylim',[0 maxeta+0.1]);
    %xlabel('Position [cm]');ylabel('Carrier Density [cm^-3]');
    %Photon density plot
    figure(fdiff_fig2);

```



```

set(gca,'YLimMode','auto');
plot(zM,SfM,zM,SrM);
T = -300; M = max([SfM SrM]);
while (10^-T < M), T = T + 1; end;
set(gca,'xlim',[0 sum(Lsect)],'ylim',[0 10^-T]);
xlabel('Position [cm]');ylabel('Photon Density [cm^{-3}]');
figure(fdiff_fig3);
set(gca,'YLimMode','auto');
plot(zM,NM);
set(gca,'ylim',[0 2.5e18]);
set(gca,'xlim',[0 sum(Lsect)]);
drawnow;
end;

%#####
% Store state commands (frequency determined by 'S')
if X/S == floor(X/S)
    ET(X/S) = toc;
    tic;
    if exist('StatusH'),
        set(StatusH,'String',['Roundtrip #' num2str(X/S,'%4.4g') ...
            ' Elapsed time: ' num2str(ET(X/S),'%03.3f') ' sec.']);
    end;
    SfRT(X/S,:) = SfM;
    SrRT(X/S,:) = SrM;
    NRT(X/S,:) = NM;
    figure(fdiff_fig4);
    pHM(X/S) = plot(tRTM/ps,SoutM(X/S,:));
    if (X/S-pdispN-ContN)>0, delete(pHM(X/S-pdispN)); end;
    delete(p3H);
    p3H = plot(tRTM/ps,SoutM(X/S:),'r');
    xlabel('Time [ps]');ylabel('Photon Density [cm^{-3}]');
    drawnow;
end
end;

```

A.3.5 plotRT.m

%PLOTRT Plots the pulse profile/width/energy evolution.

%

% See also FDIFFMAIN.

%#####

% Makes some strings to for file saving and graph titling

makeParamString;

%#####

% Removes any non-calculated roundtrips at the end of the state matrices

noRT=floor(X/S);

10

```

RT=1:noRT;
SfRT=SfRT(1:noRT,:);
SrRT=SrRT(1:noRT,:);
SoutM=SoutM(1:noRT,:);
NActM=NActM(1:noRT,:);
SfActM=SfActM(1:noRT,:);
NRT=NRT(1:noRT,:);

```

20

```

#####
% Calculate interpolated pulse width & energy (better accuracy)
smp = 6; % new sampling rate
clear Pwidth Penergy Pstream;
for Y=1:noRT-1
    [SmaxVal SmaxI] = max(SoutM(Y,:));
    if and(Y > 1, Y < noRT),
        SpulseM = [SoutM(Y-1,:) SoutM(Y,:) SoutM(Y+1,:)];
        SpulseM = SpulseM(SmaxI+round(noPRT/2)+1:SmaxI+round(noPRT/2)+noPRT);
    else
        SpulseM = SoutM(Y,:);
    end;
    if isempty(find(SpulseM)),
        SspM = SpulseM;
        tspM = tRTM;
    else
        tspM = interp(tRTM,smp);
        SspM = interp(SpulseM,smp);
    end;
    Pwidth(Y) = findwidth(SspM,tspM);
    Penergy(Y) = sum(SspM)*dz(1)/smp*W*d/Gamma*hv;
    Pstream(noPRT*(Y-1)+1:noPRT*Y) = SoutM(Y,:)*dz(1)/smp*W*d/Gamma*hv;
    Nstream(noPRT*(Y-1)+1:noPRT*Y) = NActM(Y,:);
    Sfstream(noPRT*(Y-1)+1:noPRT*Y) = SfActM(Y,:);
    tstream(noPRT*(Y-1)+1:noPRT*Y) = tRTM+(Y-1)*(tRTM(end)+tRTM(1));
end

```

30

```

#####
% Plot the pulse output, width, and energy
figure;
set(gcf,'position',[100 535 560 420]);
surf(RT,tRTM/ps,SoutM'*dz(1)*W*d/Gamma*hv);
shading interp; view(2); axis tight;
xlabel('Roundtrip #');
ylabel('Time [ps]');
zlabel('Power [W]');
title([titleS]);

```

50

```

figure;
set(gcf,'position',[700 535 560 420]);
plot(RT(1:end-1),Pwidth/ps);
xlabel('Roundtrip #');
ylabel('Pulsewidth [ps]');
title([titleS]);

```

60

```

figure;
set(gcf,'position',[700 35 560 420]);
plot(RT(1:end-1),Penergy/pJ);
xlabel('Roundtrip #');
ylabel('Pulse Energy [pJ]');
title([titleS]);

```

70

A.3.6 plotEP.m

```

%PLOTTEP Plots the pulse evolution and determines if synchronized
% Since dz is fixed but wM can be any value, there will be a mismatch
% between the pulse roundtrip, Trt, and the modulation frequency. This
% program graphically shows where the pulse should be, if it was synchronized
% to the RF source (i.e. no pulse drifting).
%
% The vertical green line is where the pulse center starts at. The vertical blue line
% shows where the pulse center should be. The pulse should already be in steady-state.
%
% Execute after FDIFFMAIN.

```

10

```

#####
% Determines how many roundtrips in the past to plot
noRTP = 100;
#####
% Removes any non-calculated roundtrips at the end of the state matrices
noRT = floor(X/S);
RT = 1:noRT;
SfRT = SfRT(1:noRT,:);
SrRT = SrRT(1:noRT,:);
SoutM = SoutM(1:noRT,:);
NActM = NActM(1:noRT,:);
SfActM = SfActM(1:noRT,:);
NRT = NRT(1:noRT,:);
#####
% Evaluates the index for the pulse peak
for x = 1:noRT,
    [tempMax peakIM(x)] = max(SoutM(x,:));
end;
#####
% Plot the pulse output, width, and energy
figure; hold on;
set(gcf,'position',[100 535 560 420]);
cM = linspace(0,1,noRTP);
for x = 1:noRTP,
    plot(tRTM/ps,SoutM(end-noRTP+x,:), 'color',[cM(x) 0 0]);
end;
#####
% Plot the start and end pulse center locations
startT = tRTM(peakIM(end-noRTP+1));
endT = startT - (noPRT*dt-2*pi/wM)*(noRTP-1);

```

20

30

40

```
plot(repmat(startT/ps,1,2),get(gca,'ylim'),'color',[0 1 0],'LineWidth',2);
plot(repmat(endT/ps,1,2),get(gca,'ylim'),'color',[0 0 1],'LineWidth',2);
hold off;
if startT > endT,
    set(gca,'xlim',[endT/ps-1/2 startT/ps+1/2],'ylim',[-1e15 1e15]+tempMax);
else
    set(gca,'xlim',[endT/ps-1/2 startT/ps+1/2],'ylim',[-1e15 1e15]+tempMax);
end;
xlabel('Time [ps]');
ylabel('Pulse Profile [cm-3]');
title([titleS]);
```

Appendix B

Second-Order Derivative Approximations

A different combination of the three Equations 4.14-4.16 gives us an approximation for the second-order derivative:

$$S(t + \Delta t) - 2S(t) + S(t - \Delta t) = 2\frac{1}{2}\frac{d^2}{dt^2}S(t)\Delta t^2 + 2\frac{1}{24}\frac{d^4}{dt^4}S(t)\Delta t^4 + \dots \quad (\text{B.1})$$

$$\frac{d^2}{dt^2}S(t) = \frac{S(t + \Delta t) - 2S(t) + S(t - \Delta t)}{\Delta t^2} + \left\{ -\frac{1}{12}\frac{d^4}{dt^4}S(t)\Delta t^2 + \dots \right\} \quad (\text{B.2})$$

This approximation has error dominated by the fourth-order term, as shown in the above equation. By using expansions around t that are $\pm 2\Delta t$ away, we can improve the dominating error term. Again, we can improve the error term by using more and more expansion terms. This was simply shown for the first-order derivative term above, improving the error from

second- to third-order. For a second-order derivative approximation, it can be shown that:

$$\begin{aligned} \frac{d^2}{dt^2}S(t) = & \frac{16S(t + 2\Delta t) - S(t + \Delta t) - 30S(t) - S(t - \Delta t) + 16S(t - 2\Delta t)}{12\Delta t^2} \\ & + \left\{ \frac{1}{90} \frac{d^6}{dt^6}S(t)\Delta t^4 + \dots \right\} \quad (\text{B.3}) \end{aligned}$$

This shows the error dominated by the sixth-order term. The use of more and more terms means that we are trying to approximate the derivatives with values of the function further and further away from the actual point in question. While the error will grow smaller as more and more terms are used, the use of many expansion terms will introduce its own set of errors. In addition, it seems necessary to know the values of function S for times greater than or equal to $t + \Delta t$. These "symmetric" approximations need equal weighted terms for each set: $t \pm \Delta t$, $t \pm 2\Delta t$, etc. Practically, we need to build a causal approximation. To solve this problem, we can use non-symmetric approximations. It can be shown that:

$$\begin{aligned} \frac{d^2}{dt^2}S(t) = & \frac{35S(t) - 104S(t - \Delta t) + 114S(t - 2\Delta t) - 56S(t - 3\Delta t) + 11S(t - 4\Delta t)}{12\Delta t^2} \\ & + \left\{ \frac{1}{12} \frac{d^5}{dt^5}S(t)\Delta t^3 + \dots \right\} \quad (\text{B.4}) \end{aligned}$$

The disadvantage of the non-symmetric approximation is that the error is larger than the symmetric case.

Note that we have not noted the z values in the above equations. When more than one variable needs to be considered, we must be careful in determining the terms of the difference equation approximation. There is a distinct difference between the approximation for partial derivatives and total derivatives. This shows up as a difference in the z value in the limits of the difference equations. For example, in the simple Euler approximation, we

note the difference between the two derivatives:

$$\frac{d}{dt}S(t) \approx \frac{S(z + \Delta z, t + \Delta t) - S(z, t)}{\Delta t} \quad (\text{B.5})$$

$$\frac{\partial}{\partial t}S(t) \approx \frac{S(z, t + \Delta t) - S(z, t)}{\Delta t} \quad (\text{B.6})$$

where

$$\frac{\Delta z}{\Delta t} = \frac{dz}{dt} = v_g \quad (\text{B.7})$$

This comes from the definition of the total derivative:

$$dS = dt \frac{\partial S}{\partial t} + dz \frac{\partial S}{\partial z} \quad (\text{B.8})$$

Of course, the partial terms only relate to a change in the function S with respect to only one variable at a time, but the total difference, dS , refers to a change in both space and time. Hence, any difference approximations of the total derivative require $z \rightarrow z + \Delta z$ whenever $t \rightarrow t + \Delta t$. For partials in time, z shall remain z .

The forward-propagating photon density rate equation, including gain bandwidth terms, that we would like to convert to a difference equation is stated here:

$$\frac{d}{dt}S^+(z, t) = v_g(\Gamma g_p(z, t) - \alpha_i)S^+(z, t) + v_g \Gamma g_p(z, t) t_2^2 \frac{\partial^2}{\partial t^2} S^+(z, t) \quad (\text{B.9})$$

It is necessary to approximate the first-order total derivative term on the left-hand side and the second-order partial time derivative term on the far right-hand side. Using Equations 4.18 and B.4, we can express the rate equation in a difference form:

$$\begin{aligned} \frac{S^+(z + \Delta z, t + \Delta t) - S^+(z, t)}{\Delta t} &\approx v_g(\Gamma g_p(z, t) - \alpha_i)S^+(z, t) + \\ &v_g \Gamma g_p(z, t) t_2^2 \times \\ &\frac{35S^+(t) - 104S^+(z, t - \Delta t) + 114S^+(z, t - 2\Delta t) - 56S^+(z, t - 3\Delta t) + 11S^+(z, t - 4\Delta t)}{12\Delta t^2} \end{aligned} \quad (\text{B.10})$$

We can then solve for $S^+(z + \Delta z, t + \Delta t)$, which corresponds to the next time step interval, $t + \Delta t$.

In a similar manner, the reverse-propagating photon rate equation can be transformed into a difference equation. The result is identical, except the total time derivative corresponds to moving backward in z -space:

$$S^+(z + \Delta z, t + \Delta t) \Rightarrow S^-(z - \Delta z, t + \Delta t) \quad (\text{B.11})$$

The carrier rate equation (Equation 3.2) is simpler to approximate. The total time derivative does not correspond to any propagation in space:

$$\frac{N(z, t + \Delta t) - N(z, t)}{\Delta t} \approx \frac{\eta_i I}{qV} - \frac{N}{\tau_c} - v_g g_p (S^+(z, t) + S^-(z, t)) \quad (\text{B.12})$$

which leads to Equation 4.9. The method of implementing this is similar to the first-order implementation, except a history of previous time steps needs be kept so that the higher-order derivatives can be calculated. Also note that we could have also used Equation 4.20 for the first-order derivative approximation. We will explore the results of using both methods in Section 4.5.2.

Bibliography

- [1] G. P. Agrawal. *Nonlinear Fiber Optics*. Academic Press, San Diego, 1989.
- [2] G. P. Agrawal and N. A. Olsson. Self-phase modulation and spectral broadening of optical pulses in semiconductor laser amplifiers. *IEEE Journal of Quantum Electronics*, 25(1):2297–2306, November 1989.
- [3] S. Arahira, Y. Matsui, and Y. Ogawa. Mode locking at very high repetition rates more than terahertz in passively mode-locked distributed-Bragg-reflector laser diodes. *IEEE Journal of Quantum Electronics*, 32:1211–1224, July 1996.
- [4] A. Bindra. Speedier ADCs pick up more bits and samples. *Electronic Design*, 47(2):66, 68, 70, 72, 74, January 1999.
- [5] J. E. Bowers, P. A. Morton, A. Mar, and S. W. Corzine. Actively mode-locked semiconductor lasers. *IEEE Journal of Quantum Electronics*, 25(6):1426–39, June 1989.
- [6] D. Burns, A. Finch, W. Sleat, and W. Sibbett. Noise characterization of a mode-locked InGaAsP semiconductor diode laser. *IEEE Journal of Quantum Electronics*, 26(11):1860–1863, November 1990.
- [7] J. Carroll, J. Whiteaway, and D. Plumb. *Distributed Feedback Semiconductor Lasers*, chapter 7, pages 209–251. SPIE Optical Engineering Press, London, 1998.
- [8] D. T. Cassidy. Technique for measurement of the gain spectra of semiconductor diode lasers. *Journal of Applied Physics*, 56(11):3096–9, December 1984.
- [9] Y.K. Chen and M.C. Wu. Monolithic colliding-pulse modelocked quantum-well lasers. *IEEE Journal of Quantum Electronics*, 28:2176–2185, October 1992.
- [10] C. Y. J. Chu and Ghafouri-Shiraz. A simple method to determine carrier recombinations in a semiconductor laser optical amplifier. *IEEE Photonics Technology Letters*, 5(10):1182–5, October 1993.
- [11] L. A. Coldren and S. W. Corzine. *Diode Lasers and Photonic Integrated Circuits*. Wiley Series in Microwave and Optical Engineering. Wiley, New York, 1995.

- [12] L. Davis, Y. Lam, D. Nichols, J. Singh, and P. K. Bhattacharya. Auger recombination rates in compressively strained $In_xGa_{1-x}As/InGaAsP/InP$ ($0.53 \leq x \leq 0.73$) multi-quantum well lasers. *IEEE Photonics Technology Letters*, 5(2):120–2, February 1993.
- [13] D. Derickson, R. Helkey, A. Mar, J. Wasserbauer, and J. Bowers. Mode-locked semiconductor lasers. *Microwave Journal*, 36(2):76, 78, 81, 83, 85–6, 88–90, February 1993.
- [14] D. J. Derickson. Explanation of timing jitter mechanisms in multisegment mode-locked semiconductor lasers. In *LEOS '93 Conference Proceedings*, IEEE Lasers and Electro-Optics Society 1993 Annual Meeting, pages 282–3, New York, 1993. LEOS.
- [15] D. J. Derickson, A. Mar, and J. E. Bowers. Relative and absolute timing jitter in actively mode-locked semiconductor lasers. In *SLC '90 Conference Digest*, volume 2 of *1990 IEEE Semiconductor Laser Conference*, pages 1063–6. IEEE, 1990.
- [16] Dennis J. Derickson. *Multi-section Mode-locked Semiconductor Lasers*. Phd dissertation, University of California, Santa Barbara, Electrical and Computer Engineering Department, July 1992.
- [17] D.J. Derickson, R.J. Helkey, A. Mar, J.R. Karin, J.G. Wasserbauer, and J.E. Bowers. Short pulse generation using multisegment mode-locked semiconductor lasers. *IEEE Journal of Quantum Electronics*, 28(10):2186–202, October 1992.
- [18] M. Y. Frankel, J. U. Kang, and R. D. Esman. High-performance photonic analogue-digital converter. *Electronics Letters*, 33(25):2096–7, December 1997.
- [19] C. Furst, A. Leitenstorfer, and A. Laubereau. Mechanism for self-synchronization of femtosecond pulses in a two-color ti:sapphire laser. *IEEE Journal of Selected Topics in Quantum Electronics*, 2(3):473–9, September 1996.
- [20] Jr. H. C. Casey and P. L. Carter. Variation of intervalence band absorption with hole concentration in p-type InP. *Applied Physics Letters*, 44(1):82–3, January 1984.
- [21] B. W. Hakki and T. L. Paoli. I. CW degradation at 300°K of GaAs double-heterostructure junction lasers. II. Electronic gain. *Journal of Applied Physics*, 44(9):4113–9, September 1973.
- [22] E. Hashimoto, A. Takada, and Y. Katagiri. Clock source-limited low jitter, subterahertz signal generation from mode-locked semiconductor laser controlled by phase locked loop (PLL) with photonic downconversion. In *Technical Digest*, International Topical Meeting on Microwave Photonics, pages 169–72, New Jersey, 1998. IEEE.
- [23] H. A. Haus. A theory of forced mode locking. *IEEE Journal of Quantum Electronics*, 11(7):323–330, July 1975.

- [24] H. A. Haus. Theory of mode-locking of a laser diode in an external resonator. *Journal of Applied Physics*, 51:4042–9, 1980.
- [25] H. A. Haus. Noise of mode-locked lasers. *IEEE Journal of Quantum Electronics*, 29(3):983–996, March 1993.
- [26] H. A. Haus and E. P. Ippen. Modelocked fiber ring lasers. In *OSA Trends in Optics and Photonics*, Ultrafast Electronics and Optoelectronics, pages 6–13, Washington, D.C., 1997. Optical Society of America.
- [27] R. J. Helkey, P. A. Morton, and J. E. Bowers. Partial-integration method for analysis of mode-locked semiconductor lasers. *Optics Letters*, 15(2):112–4, January 1990.
- [28] Roger J. Helkey. *Subpicosecond pulse generation using modelocked semiconductor laser diodes*. Phd dissertation, University of California, Santa Barbara, Electrical and Computer Engineering Department, July 1993.
- [29] T. Hoshida, H.-F. Liu, M. Tsuchiya, Y. Ogawa, and T. Kamiya. Subharmonic hybrid mode-locking of a monolithic semiconductor laser. *IEEE Journal of Selected Topics in Quantum Electronics*, 2(3):514–22, sep 1996.
- [30] K. Hsu and C. M. Verber. Stochastic mode-locking theory for external-cavity semiconductor lasers. *Journal of the Optical Society of America B*, 8(2):262–275, February 1991.
- [31] D. J. Jones, L. M. Zhang, J. E. Carroll, and D. D. Marcenac. Dynamics of monolithic passively mode-locked semiconductor lasers. *IEEE Journal of Quantum Electronics*, 31(6):1051–8, June 1995.
- [32] V. Jordan. Gain measurement of semiconductor laser diodes: requirements for the wavelength resolution and sensitivity to noise. *IEE Proceedings in Optoelectronics*, 141(1):13–5, February 1994.
- [33] P.W. Juodawlkis, J.C. Twichell, J.L. Wasserman, and R.C. Williamson. Measurement of mode-locked laser timing jitter using phase-encoded optical sampling. In *Summaries of Papers Presented at Conference on Lasers and Electro-Optics, 2000*, CLEO '00. Optical Society of America, 2000.
- [34] J. R. Karin, R. J. Helkey, D. J. Derickson, R. Nagarajan, D. S. Allin, J. E. Bowers, and R. L. Thornton. Ultrafast dynamics in field-enhanced saturable absorbers. *Applied Physics Letters*, 64(6):676–8, February 1994.
- [35] D. K. Kim. Reverse bias voltage dependent pulse shape and transmission change through a semiconductor saturable absorber. *Applied Physics Letters*, 69(18):2635–7, October 1996.

- [36] H. Kressel and J. K. Butler. *Semiconductor Lasers and Heterojunction LEDs*. Academic Press, New York, 1977.
- [37] T. Kunii, Y. Matsui, Y. Katoh, and T. Kamijoh. Low threshold current and high output power operation for $1.5\mu\text{m}$ GRINSCH strained MQW laser diode. *IEE Electronics Letters*, 31(4):282–4, feb 1995.
- [38] T. Kunii, Y. Matsui, Y. Ogawa, and T. Kamijoh. Laser characteristics for four-section MQW-DBR laser. *IEEE Photonics Technology Letters*, 4(10):1096–8, oct 1992.
- [39] K. Y. Lau. Narrow-band modulation of semiconductor lasers at millimeter wave frequencies (> 100 GHz) by mode locking. *IEEE Journal of Quantum Electronics*, 26(2):250–261, February 1990.
- [40] D. A. Leep and D. A. Holm. Spectral measurement of timing jitter in gain-switched semiconductor lasers. *Applied Physics Letters*, 60(20):2451–3, May 1992.
- [41] A. J. Lowery. New dynamic semiconductor laser model based on the transmission-line modelling method. *IEE Proceedings*, 134:281–9, 1987.
- [42] A. J. Lowery. *Transmission line modelling of semiconductor lasers*. Phd dissertation, Nottingham University, 1988.
- [43] A. J. Lowery. Modelling spectral effects of dynamic saturation in semiconductor laser amplifiers using the transmission-line laser model. *IEE Proceedings*, 136(6):320–4, December 1989.
- [44] A. J. Lowery. New time-domain model for active mode locking, based on the transmission line laser model. *IEE Proceedings*, 136(5):264–72, October 1989.
- [45] M. B. El Mashade and J. Arnaud. Effect of facet coatings on far fields of semiconductor lasers. *Electronic Letters*, 23(11):568–70, May 1987.
- [46] J. L. Moll and S. A. Hamilton. Physical modeling of the step recovery diode for pulse and harmonic generation circuits. *Proceedings of the IEEE*, 57(7):1250–1259, 1968.
- [47] P. A. Morton, R. J. Helkey, and J. E. Bowers. Dynamic detuning in actively mode-locked semiconductor lasers. *IEEE Journal of Quantum Electronics*, 25(12):2621–2633, December 1989.
- [48] A. P. Ongstad, G. C. Dente, M. L. Tilton, J. Stohs, and D. J. Gallant. Determination of carrier lifetimes using Hakki-Paoli gain data. *Applied Physics Letters*, 72(7):836–8, February 1998.
- [49] J. Piprek, P. Abraham, and J. E. Bowers. Cavity length effects on internal loss and quantum efficiency of multiquantum-well lasers. *IEEE Journal of Selected Topics in Quantum Electronics*, 5(3):643–7, May/June 1999.

- [50] E. M. Pratt and J. E. Carroll. Gain modelling and particle balance in semiconductor lasers. *IEE Proceedings in Optoelectronics*, 147(2):77–82, April 2000.
- [51] M. J. W. Rodwell, D. M. Bloom, and B. A. Auld. Nonlinear transmission line for picosecond pulse compression and broadband phase modulation. *Electronic Letters*, 23(3):109–110, 1987.
- [52] F. Scheid. *Numerical Analysis*. Schaum's Outlines. McGraw Hill, New York, 2nd edition, 1988.
- [53] M. Schell and E. Schöll. Time-dependent simulation of a semiconductor laser amplifier: pulse compression in a ring configuration and dynamic optical bistability. *IEEE Journal of Quantum Electronics*, 26(6):1005–13, June 1990.
- [54] M. Schell, A. G. Weber, E. H. Böttcher, E. Schöll, and D. Bimberg. Theory of subpicosecond pulse generation by active modelocking of a semiconductor laser amplifier in an external cavity: limits for the pulsewidth. *IEEE Journal of Quantum Electronics*, 27(3):402–8, March 1991.
- [55] M. Schell, A. G. Weber, E. Schöll, and D. Bimberg. Fundamental limits of sub-ps pulse generation by active mode locking of semiconductor lasers: the spectral gain width and the facet reflectivities. *IEEE Journal of Quantum Electronics*, 27(6):1661–7, June 1991.
- [56] T. Shibata and M. Yoneyama. A novel sample and hold system using an optical modulator. *IEEE Photonics Technology Letters*, 4(6):588–591, June 1992.
- [57] G. E. Shtengel, D. A. Ackerman, and P. A. Morton. True carrier lifetime measurements of semiconductor lasers. *Electronic Letters*, 31(20):1747–8, September 1995.
- [58] A. E. Siegman. *Lasers*, chapter 24-28. University Science Books, California, 1986.
- [59] J.C. Twichell, P.W. Juodawlkis, J.L. Wasserman, R.C. Williamson, and G.E. Betts. Extending the performance of optically sampled time-demultiplexed analog-to-digital converters. In *Summaries of Papers Presented at Conference on Lasers and Electro-Optics, 2000*, CLEO '00. Optical Society of America, 2000.
- [60] A. V. Uskov, J. R. Karin, R. Nagarajan, and J. E. Bowers. Dynamics of carrier heating and sweepout in waveguide saturable absorbers. *IEEE Journal of Selected Topics in Quantum Electronics*, 1(2):552–561, June 1995.
- [61] P. Vasil'ev. *Ultrafast Diode Lasers: Fundamentals and Applications*, chapter 4, pages 95–149. Artech House, Inc., 1995.
- [62] D. von der Linde. Characterization of the noise in continuously operating mode-locked lasers. *Applied Physics B*, B39(4):201–217, April 1986.

- [63] R. H. Walden. Analog-to-digital converter survey and analysis. *IEEE Journal on Selected Areas in Communications*, 17(4):539–50, April 1999.
- [64] J. Werner and T. P. Lee. Monte carlo simulation of mode-locked semiconductor diode lasers. *Applied Physics Letters*, 57(12):1236–8, September 1990.
- [65] E. Wintner and E. P. Ippen. Nonlinear carrier dynamics in $Ga_xIn_{1-x}As_yP_{1-y}$ compounds. *Applied Physics Letters*, 44(10):999–1001, May 1984.
- [66] J. A. Yeung. Theory of active mode-locking of a semiconductor laser in an external cavity. *IEEE Journal of Quantum Electronics*, 17:399–404, 1981.
- [67] L. M. Zhang, S. F. Yu, M. C. Nowell, D. D. Marcenac, J. E. Carroll, and R. G. S. Plumb. Dynamic analysis of radiation and side-mode suppression in a second-order DFB laser using time-domain large signal traveling wave model. *IEEE Journal of Quantum Electronics*, 30(6):1389–95, June 1994.

Deposit Report

Date: 2/5/01

<i>Customer Name</i>	<i>Check Number</i>	<i>Payment Amount</i>
1st. Advertising	5899	\$250.00
Activac	350	\$330.00
Actuality Systems Inc.	1563	\$880.00
Akademos.com	1420	\$980.00
AllCampus Media	0025088	\$80.00
Allied Advertising Agency	5916	\$130.90
American Passage	63173	\$5,464.44
American Passage	63255	\$2,338.50
American Passage	65642	\$3,588.00
Atheros Communications, Inc.	3535	\$250.00
August, Lang & Husak	4655	\$440.00
Barnes & Noble College Bookst	762551	\$1,525.00
Bernard Hodes Advertising, Inc.	332780	\$673.20
Booz-Allen & Hamilton	3222023831	\$50.00
Boston Field & Focus Performan	6692	\$396.00
California Cryobank, Inc.	1761	\$352.00
Cambridge School Volunteers, I	3694	\$56.00
Cornerstone Research	1400	\$165.00
Council Travel	420749	\$126.00
Dean & Company	19538	\$500.00
Exponent	665253	\$400.00
Future Pages, LLC	6510	\$112.20
Gordian	8217	\$660.00
Harvard Coop	608307	\$792.00
Harvard University	388711	\$168.00
Janet Seluga	5996	\$90.00
LaVerde's Market	7383	\$400.00
Marsha Kirgan, MD	2837	\$105.60
Mary H. Cheung	1267	\$45.00
McKinsey & Company, Inc.	101341	\$1,200.00

<i>Customer Name</i>	<i>Check Number</i>	<i>Payment Amount</i>
Media Space Bank	8395	\$800.00
Media Space Bank	8451	\$800.00
Mercator Partners	1944	\$250.00
Merrill Lynch ITG	100106909	\$1,800.00
MIT Chi Alpha Christian Fellows	1075	\$96.00
MIT Employees' Federal Credit	503191	\$740.00
Morgan Stanley	00649897	\$4,800.00
Opnet Technologies, Inc	23425	\$176.00
Paul T. Shane	1945	\$110.00
Pennie & Edmonds	213624	\$1,200.00
PRE-PAID CUSTOMER	06-118326616	\$44.00
RNK Telecom	1744	\$880.00
Sephir Hamilton	353	\$100.00
Sports Printers	132	\$50.00
Stainless Steel Studios, Inc.	1896	\$252.00
Strickling/Hans	2982	\$45.00
Student Travel Service	64625	\$110.00
Student Travel Service	65455	\$618.00
Sun Splash Tours, Inc.	18557	\$110.00
Thailand Café	143	\$88.00
Tony & Carol Wilkerson	2685	\$45.00
United Technologies Research	308454	\$800.00
University of California, Los Ang	0006518221	\$250.00
William Katz	2592	\$85.00
Xicor	230979	\$1,000.00
Young Rubicam/Army Group	4000352339	\$462.00
Young Rubicam/Army Group	4000345540	\$250.00

Number Of Checks

57

Total Deposit

\$38,508.84

Deposit Report

Date: 2/5/01

<i>Customer Name</i>	<i>Check Number</i>	<i>Payment Amount</i>
1st. Advertising	5899	\$250.00
Activac	350	\$330.00
Actuality Systems Inc.	1563	\$880.00
Akademos.com	1420	\$980.00
AllCampus Media	0025088	\$80.00
Allied Advertising Agency	5916	\$130.90
American Passage	65642	\$3,588.00
American Passage	63255	\$2,338.50
American Passage	63173	\$5,464.44
Atheros Communications, Inc.	3535	\$250.00
August, Lang & Husak	4655	\$440.00
Barnes & Noble College Bookst	762551	\$1,525.00
Bernard Hodes Advertising, Inc.	332780	\$673.20
Booz-Allen & Hamilton	3222023831	\$50.00
Boston Field & Focus Performan	6692	\$396.00
California Cryobank, Inc.	1761	\$352.00
Cambridge School Volunteers, I	3694	\$56.00
Cornerstone Research	1400	\$165.00
Council Travel	420749	\$126.00
Dean & Company	19538	\$500.00
E Ink Corporation	011942	\$800.00
Exponent	665253	\$400.00
Future Pages, LLC	6510	\$112.20
Gordian	8217	\$660.00
Harvard Coop	608307	\$792.00
Harvard University	388711	\$168.00
Janet Seluga	5996	\$90.00
LaVerde's Market	7383	\$400.00
Marsha Kirgan, MD	2837	\$105.60
Mary H. Cheung	1267	\$45.00

<i>Customer Name</i>	<i>Check Number</i>	<i>Payment Amount</i>
McKinsey & Company, Inc.	101341	\$1,200.00
Media Space Bank	8451	\$800.00
Media Space Bank	8395	\$800.00
Mercator Partners	1944	\$250.00
Merrill Lynch ITG	100106909	\$1,800.00
MIT Chi Alpha Christian Fellows	1075	\$96.00
MIT Employees' Federal Credit	503191	\$740.00
Morgan Stanley	00649897	\$4,800.00
Opnet Technologies, Inc	23425	\$176.00
Paul T. Shane	1945	\$110.00
Pennie & Edmods	213624	\$1,200.00
PRE-PAID CUSTOMER	06-118326616	\$44.00
RNK Telecom	1744	\$880.00
Sephir Hamilton	353	\$100.00
Sports Printers	132	\$50.00
Stainless Steel Studios, Inc.	1896	\$252.00
Strickling/Hans	2982	\$45.00
Student Travel Service	64625	\$110.00
Student Travel Service	65455	\$618.00
Sun Splash Tours, Inc.	18557	\$110.00
Thailand Café	143	\$88.00
Tony & Carol Wilkerson	2685	\$45.00
United Technologies Research	308454	\$800.00
University of California, Los Ang	0006518221	\$250.00
William Katz	2592	\$85.00
Xicor	230979	\$1,000.00
Young Rubicam/Army Group	4000352339	\$462.00
Young Rubicam/Army Group	4000345540	\$250.00

Number Of Checks

58

Total Deposit

\$39,308.84